# Flexible Proton Optics for Concurrent Operation of the e-p and p-p Experiments in the HL-LHC and the FCC-eh Collider

Von der Fakultät für Mathematik und Naturwissenschaften der RWTH Aachen University zur Erlangung des akademischen Grades eines Doktors der Naturwissenschaften genehmigte Dissertation

vorgelegt von

Tiziana Marie Pauline von Witzleben, M.Sc.

aus Trier, Deutschland

Berichter: Prof. Dr. Jörg Pretz
Prof. Dr. Achim Stahl
Dr. Bernhard Holzer

Tag der mündlichen Prüfung: 24.06.2026

Diese Dissertation ist auf den Internetseiten der Universitätsbibliothek online verfügbar.

I hereby declare that I have created this work completely on my own and used no other sources or tools than the ones listed, and that I have marked any citations accordingly.

Hiermit versichere ich, dass ich die vorliegende Arbeit selbständig verfasst und keine anderen als die angegebenen Quellen und Hilfsmittel benutzt sowie Zitate kenntlich gemacht habe.

*Aachen, July 2026*
*Tiziana von Witzleben*

# Contents

**Abstract** **5**

**Zusammenfassung** **6**

**1 Motivation** **7**
1.1 Physics Case of LHeC and FCC-eh . . . . . 10

**2 Theory of Accelerator Physics** **13**
2.1 Linear Beam Optics . . . . . 13
2.1.1 Hill's Equation . . . . . 16
2.1.2 Courant-Snyder Parameters and the Phase Space Ellipse . . 17
2.1.3 Gaussian Beam Profile and Aperture . . . . . 19
2.1.4 Beam Envelope and Beta Function Evolution with Matrix Propagation . . . . . 21
2.1.5 Mini $\beta$ Insertions . . . . . 22
2.2 Luminosity . . . . . 24
2.2.1 Beam-Beam Effects . . . . . 25
2.3 Linear Beam Imperfections . . . . . 27
2.4 Momentum Spread, Dispersion and Chromaticity . . . . . 29
2.5 Frameworks for the Data Generation . . . . . 32
2.5.1 MAD-X . . . . . 32
2.5.2 Xsuite . . . . . 33

**3 Concurrent Operation of LHeC and HL-LHC** **35**
3.1 The Large Hadron electron Collider Study . . . . . 35
3.2 Scheduled Upgrades for the Large Hadron Collider . . . . . 39
3.2.1 The High Luminosity Large Hadron Collider (HL-LHC) Upgrade . . . . . 40
3.3 The Mutlipurpose Interaction Region . . . . . 42

**4 Installation of the Electron Insertion** **47**
4.1 Calculation of the Misalignment of the Quadrupole Doublet in Reference to the Proton Orbit . . . . . 49
4.2 Impact of the Electron Insertion on the Proton Beams . . . . . 53
4.2.1 Impact of the Electron Insertion on the Orbit of the Proton Beams . . . . . 54
4.2.2 Impact of the Electron Insertion on the Optics of the Proton Beams . . . . . 56

**5 Flexible Proton Optics for LHeC** **61**
5.1 Achromatic Telescopic Squeeze Optics in the LHC and the HL-LHC 61
5.2 High Luminosity Optics for the Niobium Titanium Triplet . . . . . 63
5.2.1 Necessary Hardware Changes for this Machine Layout . . . 68
5.3 High Luminosity Optics for the Niobium Tin Triplet . . . . . 69
5.3.1 Installation of the Niobium Tin Triplet . . . . . 70
5.3.2 High Luminosity Optics for the $Nb_3Sn$ Triplet . . . . . 73

**6 Optimization of the Proton Beam Separation** **77**
6.1 Principle of the Proton Beam Separation . . . . . 77
6.2 Optimization of the Proton Inter Beam Distance . . . . . 79
6.3 Luminosity Constraints of the Optimization . . . . . 84
6.3.1 Beam-Beam Effects . . . . . 85
6.3.2 Aperture Limitations . . . . . 85
6.4 Inter Beam Distance Optimization for the LHeC IR Using a NbTi Triplet . . . . . 86
6.4.1 Defined Parameter Space . . . . . 86
6.4.2 Optimal Inter Beam Distance . . . . . 87
6.4.3 Optimal Beam Stay Clear . . . . . 90
6.5 Inter Beam Distance Optimization for the LHeC IR Using a $Nb_3Sn$ Triplet . . . . . 93
6.5.1 Defined Parameter Space . . . . . 93
6.5.2 Optimal Inter Beam Distance . . . . . 95
6.5.3 Beam Stay Clear . . . . . 97
6.6 Summary . . . . . 99

**7 Dynamic Aperture Calculations for the LHeC Interaction Region** **101**
7.1 Preparation for the Tracking Simulations . . . . . 101
7.2 Dynamic Aperture Studies of the Colliding Proton Beam . . . . . 103
7.2.1 Beam-beam Impact of the Electron Beam on the Colliding Proton Beam . . . . . 105
7.3 Dynamic Aperture Studies of the Colliding Proton Beam without the Spectating Proton Beam . . . . . 107

**8 Luminosity Expectation for LHeC** **111**
8.1 LHeC in Alternating Operation with p-p/ion-ion Operation . . . . 113
8.2 LHeC as a Stand Alone Experiment . . . . . 115
8.3 Summary . . . . . 115

**9 Design of the Interaction Region for the FCC-eh Collider 117**
9.1 Implementation of the Electron Hadron Interaction Region . . . . . 119
9.2 Impact of the Electron Insertion on the Proton Beams . . . . . 120
9.2.1 Impact of the Electron Insertion on the Orbit of the Proton Beams . . . . . 120
9.2.2 Impact of the Electron Insertion on the Optics of the Proton Beams . . . . . 122

**10 Summary 125**

**11 Outlook 127**

**Acknowledgements 129**

**A Appendix I: Electron Magnet Insertion and Proton Beam Optics 133**
A.1 Installation of the Electron Insertion . . . . . 133
A.1.1 Correction of the Proton Optics after Insertion of the Electron Interaction Region . . . . . 134
A.2 Creation of the Proton Optics for LHeC . . . . . 134
A.2.1 Proton Optics for the NbTi Triplet . . . . . 134
A.2.2 Proton Optics for the $Nb_3Sn$ Triplet . . . . . 135
A.3 Optimization of the Proton Beam Separation . . . . . 135
A.3.1 Settings of the Orbit Separation . . . . . 135
A.3.2 Optimization of the Proton Beam Separation for the NbTi Triplet . . . . . 138
A.3.3 Optimization of the Proton Beam Separation for the $Nb_3Sn$ Triplet . . . . . 139
A.3.4 Plot Generation . . . . . 142

**B Appendix II: Dynamic Aperture Calculations for the LHeC Interaction Region 143**
B.1 Preparation of the Lattices before Tracking . . . . . 143
B.2 Chromatic Correction for low $\beta$ values for LHeC using a NbTi Triplet 143
B.3 Luminosity Expectation for LHeC without the Spectating Proton Beam . . . . . 147
B.4 Tune Footprint of the Colliding Proton Beam of LHeC . . . . . 148

**C Appendix III: Design of the Interaction Region for the FCC-eh Collider 149**

**Bibliography 151**

## Abstract

Electron-proton deep inelastic scattering is a cornerstone in understanding the internal structure of the proton and the nature of the strong interaction. In these experiments, the point-like electron is used to probe the proton, effectively acting as a high-resolution microscope. This was explored between 1992 and 2007 at the Hadron-Elektron-RingAnlage (HERA), which operated at an ultimate center of mass energy of $320\,\mathrm{GeV}$. The Large Hadron electron Collider (LHeC) and the Future Circular Collider for electron-hadron collisions (FCC-eh) are design studies exploring the possibility of electron-proton (e-p) collisions at the $\mathrm{TeV}$ energy scale at CERN, thereby increasing the resolution of this microscopic probe.
In these proposed colliders, the electrons would be accelerated in an energy-recovery linac (ERL) placed tangentially to the corresponding hadron accelerator. For the LHeC, the electrons would be accelerated to an energy of $50\,\mathrm{GeV}$ and collide with one of the $7000\,\mathrm{GeV}$ protons from the High Luminosity-Large Hadron Collider (HL-LHC), resulting in a center of mass energy of $1.2\,\mathrm{TeV}$. For the FCC-eh the corresponding energies are $60\,\mathrm{GeV}$ for the electrons and $50\,000\,\mathrm{GeV}$ for the protons, yielding a center of mass energy of $3.5\,\mathrm{TeV}$.
The e-p collisions would take place at one of the four interaction points of the hadron colliders, while the remaining interaction points would continue to operate for p-p collisions. This configuration requires two proton beams to circulate in the HL-LHC/FCC-hh as usual, and an additional electron beam from the ERL. One of the proton beams is brought into collision with the electron beam, whereas the second proton beam will be guided around the e-p interaction point in the same beam pipe without colliding.
An interaction region has been designed for the LHeC that can operate in either e-p or p-p mode, using a novel multipurpose detector. The proton beam optics were modeled and optimized using the software package MAD-X to achieve the highest possible e–p luminosity, while also maximizing the separation between the two proton beams at the e–p interaction point. This was achieved by using asymmetric optics and orbit configurations for the two proton beams. Different magnet technologies for the final focusing system of the protons, consisting of either Niobium Titanium or $\mathrm{Niobium_3Tin}$, were considered. Subsequently, tracking simulations were performed with the Xsuite framework to study the beam–beam effect of the electron beam on the colliding proton beam and to evaluate the dynamic aperture of this proton beam.
For the FCC-eh interaction region, magnets which guide and focus the electron beam have been integrated into the new $90\,\mathrm{km}$ ring FCC-hh design. For both collider concepts, the influence of the electron magnets, used to guide and focus the electron beam, on the proton beams was investigated and corrected.

## Zusammenfassung

Tiefinelastische Elektron-Proton Streuexperimente sind ein zentrales Werkzeug zum Verständnis der inneren Struktur des Protons und der starken Wechselwirkung. Hierbei dient das punktförmige Elektron als Sonde zur Untersuchung von Mikrostrukturen, die mit dem bloßen Auge nicht auflösbar sind. Zwischen 1997 und 2007 wurden an der Hadron-Elektron RingAnlage (HERA) Elektron-Proton (e-p) Kollisionen mit finalen Schwerpunktsenergien von $320\,\mathrm{GeV}$ realisiert. Der Large Hadron electron Collider (LHeC) und der Future Circular Collider for electron-hadron collisions (FCC-eh) sind Designstudien, die die Möglichkeit hochenergetischer e-p Kollisionen am CERN untersuchen, um die Auflösung dieser Experimente weiter zu erhöhen.
In diesen e-p Kollisionsbeschleunigern würden Elektronen in einem tangential zu den Hadronenbeschleunigern angeordneten Energy-Recovery-Linac (ERL) beschleunigt und anschließend mit einem der Protonenstrahlen des High Luminosity-Large Hadron Colliders (HL-LHC) bzw. des FCC-hh zur Kollision gebracht werden. Im Fall des LHeCs würden die Elektronen auf eine Energie von $50\,\mathrm{GeV}$ beschleunigt werden, bevor sie mit einem der $7000\,\mathrm{GeV}$ Protonenstrahlen des HL-LHC's zusammen treffen würden. Für den FCC-eh werden Elektronenenergie von $60\,\mathrm{GeV}$ vorgesehen, die mit $50\,000\,\mathrm{GeV}$ Protonen des FCC-hhs kollidieren würden. Hierbei würden e-p Schwerpunktsenergien von $1.2\,\mathrm{TeV}$ bzw. $3.5\,\mathrm{TeV}$ erreicht werden.
Die e–p Kollisionen würden an einem der insgesamt vier Interaktionspunkten des Protonenbeschleunigers stattfinden, während die übrigen Interaktionspunkte weiterhin gleichzeitig für p–p Kollisionen genutzt werden würden. Diese Konfiguration erfordert, dass zwei Protonenstrahlen im HL-LHC/FCC-hh beschleunigt werden, während der Elektronenstrahl im ERL beschleunigt wird. Einer der Protonenstrahlen würde mit dem Elektronenstrahl kollidieren, während der zweite Protonenstrahl um diesen e–p-Interaktionspunkt herum geführt werden würde, ohne an dieser Kollision teilzunehmen. Für den LHeC wurde mithilfe des Softwarepakets MAD-X eine Interaktionsregion entworfen, welche sowohl e–p als auch p–p Kollisionen mit einem Merhzweckdetektor ermöglichen würde. Hierfür wurden die Protonenstrahloptiken modelliert und optimiert, um eine möglichst hohe e–p Luminosität zu erreichen und gleichzeitig den Abstand zwischen den beiden Protonenstrahlen am e–p Interaktionspunkt durch asymmetrische Optiken und unterschiedliche Orbite der Protonen zu maximieren. Hierbei wurden verschiedene Materialien für die Magnettechnologien zur Fokussierung der Protonen vor der Kollision (Niob-Titan und Niob-Zinn) untersucht. Anschließend wurden Tracking-Simulationen mit dem Framework Xsuite durchgeführt, um die Strah-Strahl-Wechselwirkung des Elektronenstrahls auf den kollidierenden Protonenstrahl zu untersuchen und um die dynamische Apertur dieses Protonenstrahls zu bestimmen.
Für den FCC-eh wurden die Magnete, welche die Elektronen führen und fokussieren, in das neue $90\,\mathrm{km}$ Protonen Ringdesigns integriert. Für beide Beschleunigerkonzepte wurde der Einfluss dieser Elektronenmagnete auf die Optik und die Orbite der Protonen untersucht und anschließend korrigiert.

# 1 Motivation

Humans are the most influential life form on planet earth. Yet, from an evolutionary point of view, we did not prevail because we were particularly strong or fast. We thrived thanks to our curiosity and our ability to connect to another through a common language and, as a result, to build tools and to form communities. We are also the only species we know of which tries to understand itself, more precisely, what we are made of and how we came to be.

The field of particle physics aims to answer these questions by studying the smallest, indivisible building blocks of matter. It turns out that matter, and as a result everything we see including ourselves, consists of the same small particles. The theory of these particles, together with their interacting forces, is described in the *Standard Model*. These particles cannot be observed by the human eye. Visible light has wavelengths far larger than an atom, so atoms and their substructures can't be "seen" directly. To verify theoretical predictions or discover new physics, we must build tools that extend our senses.

One way to investigate these "invisible" micro structures is with scattering experiments. This field was pioneered in 1911 with Ernest Rutherford's series of experiments [1]. By shooting $\alpha$ particles (helium ions) from a radium source at a gold foil, he discovered that most particles passed straight through the foil, while some were deflected at large angles. He concluded that atoms must consist of very small and heavy cores with vast spaces between them.

Today, more than a century later, the primary tool to test particle theories experimentally is through high-energy particle colliders. By accelerating particles to relativistic energies, colliding them and studying the resulting debris, physicists around the world can draw conclusions about the underlying forces, as well as the properties of the particles themselves. In these machines, particle beams travel in opposing directions and collide within a particle detector. The most powerful particle collider in the world is the Large Hadron Collider (LHC). This $27\,\mathrm{km}$ large accelerator of the the European Organization for Nuclear Research (CERN) in Switzerland collides either two proton beams or two heavy ion beams at record-breaking energies at four interaction points. While Rutherford's team consisted of only a few dozen researchers [2], an accelerator complex like the LHC engages scientists from around $80$ countries and $950$ scientific institutions [3]. Its discoveries have already contributed to several Nobel prizes [4–7]. Yet, despite the success of LHC and other fundamental research experiments around the world, many questions within the Standard Model are still unanswered and the theory remains incomplete. For this reason, several future colliders have been proposed to extend CERN's accelerator program.

These include the Large Hadron electron Collider (LHeC), first proposed in 2006 [8], and the Future Circular Collider for electron-hadron collisions (FCC-eh), proposed in 2018 [9]. The FCC itself is a suggested $90\,\mathrm{km}$ circular collider at CERN, envisioned to operate with electron-positron collisions in the late 2040s and with proton-proton collisions in the late 2070s [10]. The goal of both the LHeC and FCC-eh is to achieve unprecedented high energy electron-proton collisions, concurrently with the other proton-proton experiments. These experiments are part of *deep inelastic scattering (DIS)* physics, in which an elementary electron beam probes the internal structure of the proton. Unlike electrons, protons are not fundamental particles. Protons belong to the group of *hadrons*, which are composed of smaller constituents called *quarks*. The electron beam therefore acts like a high-resolution microscope, resolving the proton's substructure with far greater clarity than is possible in the more complex hadron-hadron collisions.

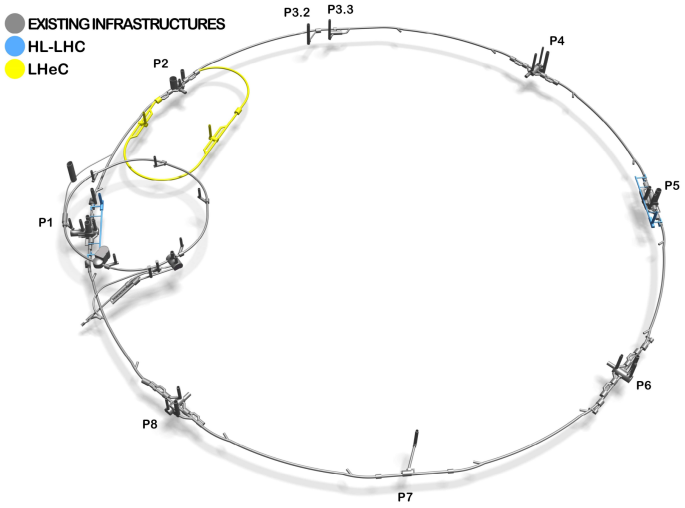


**Figure 1:** Schematic view of a possible layout for LHeC. It displays the ERL (yellow) and the LHC (grey) together with the planned High Luminosity-LHC (HL-LHC) upgrade. The proton-proton collisions take place at point 1, point 5, and point 8. At point 2 the protons can collide with electrons or protons. Figure adapted from [11].

In the proposed designs, the electron beam would be accelerated in an *energy recovery linear accelerator (ERL)*. This type of accelerator can recover an estimated $94\,\%$ [12] of the invested energy used to accelerate the electron beam before the collision by subsequently using the same structure to decelerate the beam and feed its energy back into the system. Such a sustainable accelerator would accelerate the electrons tangentially to the hadron beams of the LHC or the FCC before colliding them with one of the hadron beams. A schematic view of LHeC can be seen in figure 1, while figure 2 shows a schematic view of FCC-eh.

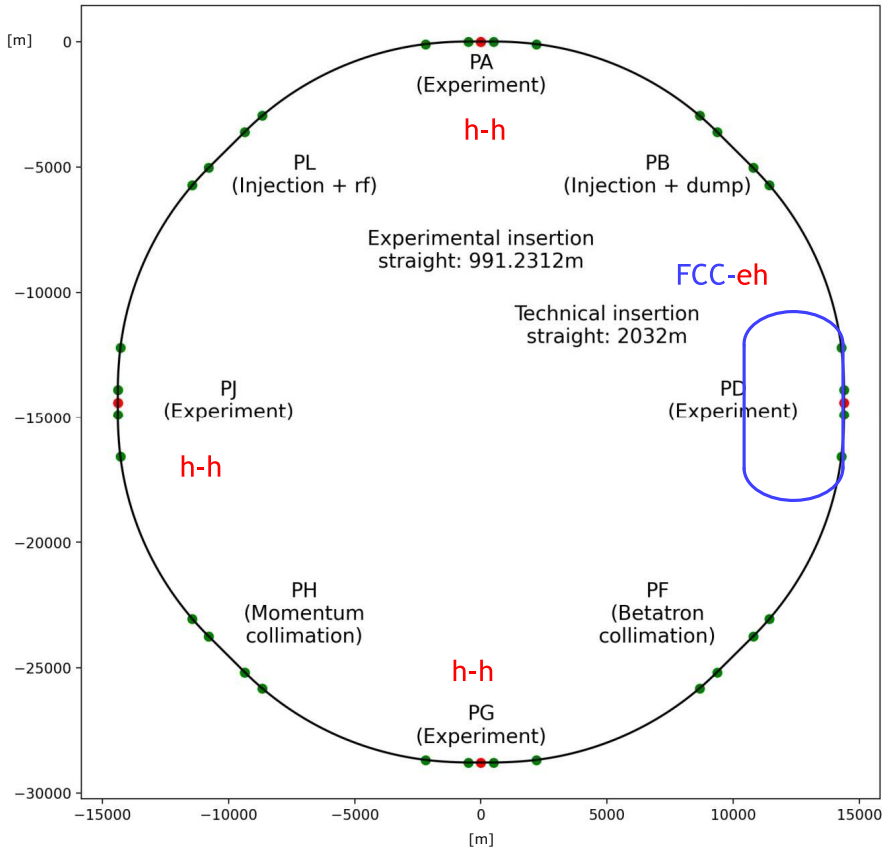


**Figure 2:** Schematic layout of a possible design of FCC-eh. The three hadron-hadron collisions are marked together with an ERL placed at interaction point D (PD) to enable electron-hadron collisions [13, 14].

In previous studies, LHeC was assumed to have its own dedicated electron-proton interaction region. Since 2021 novel considerations have been discussed in which this interaction region could be used for both electron-hadron and hadron-hadron collisions in alternating mode, concurrently with the remaining three hadron-hadron interaction points in LHC [15]. In this PhD thesis an interaction region has been designed for the LHeC that enables alternative operation of electron-proton collisions or proton-proton collisions. Since the two proton beams circulate in the LHC and must be brought into collision at several interaction points (see figure 1 and figure 2), while a single electron beam is provided by the ERL, a total of three particle beams passes through this interaction region. Only one of the proton beams collides with the electron beam at this interaction point, while the second proton beam is guided around this collision. The designed three-beam interaction region for LHeC is the first of its kind and presents a unique opportunity for the synergy of experiments.

For FCC-eh, the necessary hardware for the electron beam has been added to the proton model of the 2023 FCC-hh design study [16], laying the groundwork for an electron–hadron interaction region within the future $90\,\mathrm{km}$ collider.

In addition to the scientific insights that can be gained from an electron-hadron collider, a large-scale international and technological project of this kind often leads to unexpected discoveries and innovations impossible to predict before construction. The field of particle physics has historically driven major technological advancements, including breakthroughs in medical applications such as cancer therapy, developments in information technology (such as the world wide web and semiconductor technologies), and significant contributions to industrial technologies and instrumentation [17–19]. In the words of Marie Curie, who was awarded the Nobel Prize in 1911 [20] for the discovery and isolation of radium, the source of $\alpha$ particles used by Rutherford in his scattering experiments:

*"We must not forget that when radium was discovered no one knew that it would prove useful in hospitals. The work was one of pure science. And this is a proof that scientific work must not be considered from the point of view of the direct usefulness of it. It must be done for itself, for the beauty of science, and then there is always the chance that a scientific discovery may become like the radium a benefit for mankind [21]."*

Projects like LHeC and FCC-eh are motivated by the fundamental curiosity to understand the origins and nature of our universe and ourselves. These proposed machines could be built with the collective effort of people working across borders and disciplines, drawing on the mentioned core strengths of our species: our ability to create tools and to collaborate using a common language.

## 1.1 Physics Case of LHeC and FCC-eh

The physics case of LHeC is presented in detail in the 2021 LHeC design report [11, 22], while the physics case for FCC-eh is presented comprehensively here [23] and information on both projects is available on the collaboration website [24]. The main physics objectives are summarized below. The information in this section was extracted from [11, 22, 23], unless stated otherwise.

In this thesis a design for LHeC is discussed which reaches center of mass energies $\sqrt{s} = \sqrt{4E_eE_p}$ of $1.2\,\mathrm{TeV}$ by colliding a $7000\,\mathrm{GeV}$ proton beam with a $50\,\mathrm{GeV}$ electron beam. This center of mass energy is approximately four times higher than that of its electron-proton predecessor HERA, which reached $320\,\mathrm{GeV}$ [25]. In FCC-eh, $50\,\mathrm{TeV}$ protons collide with $60\,\mathrm{GeV}$ electrons, yielding a center of mass energy of $\sqrt{s}$ =3.46 TeV.

The parton distribution functions (PDFs) describe how the proton's momentum is distributed among the quarks and gluons confined within the proton. Each quark q (or antiquark $\bar{q}$) and each gluon carries a certain probability of taking a fraction $x$ of the proton's momentum. These probabilities depend on the energy scale of the interaction, quantified by the four-momentum transfer $Q^2$, which determines the level of detail with which the proton is probed. In figure 3, $Q^2$ is plotted versus the momentum fraction $x$ for different DIS colliders.

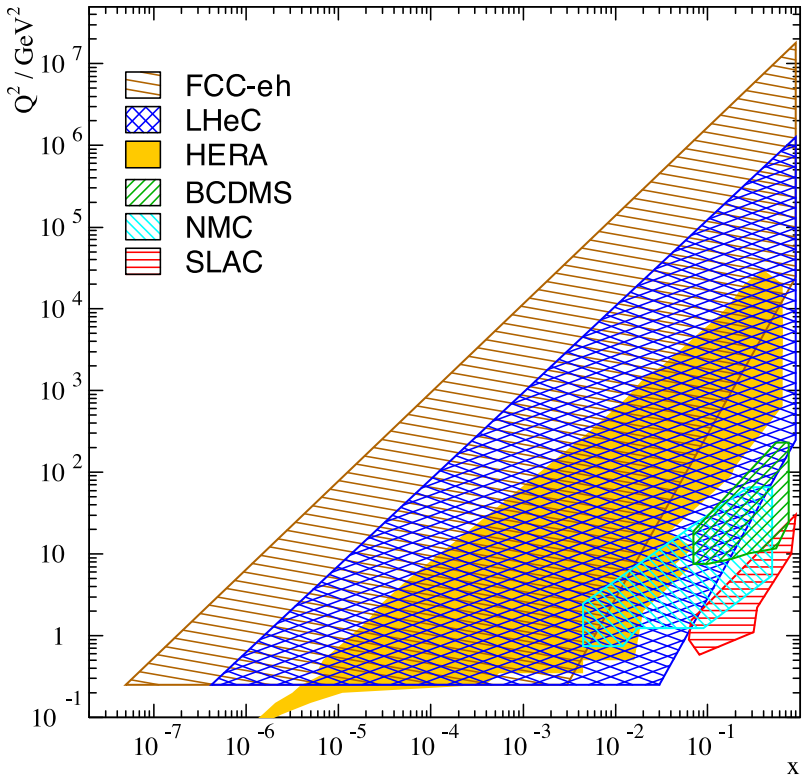


**Figure 3:** Comparison of the kinematic regions that can be explored depending on the DIS collider. The first electron-proton collisions were performed at the Stanford Linear Accelerator (SLAC) in 1968. These were followed by fixed-target muon-scattering experiments, including the Bologna-CERN-Dubna-Munich-Saclay (BCDMS) experiments conducted from 1978 to 1985, and the New Muon Collaboration (NMC), active from 1986 to 1989. The electron-proton collider HERA (Hadron Elektron Ringanlage), which operated from 1992 to 2007, extended the accessible kinematic range substantially [26]. Figure adapted from [11], with modifications.

Compared to previous DIS experiments, LHeC and FCC-eh would extend the accessible ranges in $x$ and $Q^2$ by several orders of magnitude.

This would allow the determination of the **proton PDFs** q=$u_v, d_v, u, \bar{u}, d, \bar{d}, s, c, b, t$ with a single DIS experiment, along with the determination of $\alpha_s$ to a per mille

accuracy [22]. In the low $Q^2$, low $x$ plane, LHeC and FCC-eh could probe **non linear quantum chromodynamics (QCD)**, marked by gluon interactions at extremely small $x$ [11, 22, 27].

Additionally to the PDFs, the LHeC and FCC-eh could produce large samples of **Higgs bosons** in clean DIS environments, enabling the measurement of the six dominant Higgs decay channels ($b\bar{b}$, $W^+W^-$, $gg$, $\tau\bar{\tau}$, $c\bar{c}$ and $ZZ$) and their couplings with percent-level accuracy [22] and, as a result, measure the total Higgs width. Additionally, the CP structure and the magnitude of the top Yukawa coupling could be studied [28].

In **top-quark** physics, the LHeC and FCC-eh provide strong complementarity to their corresponding hadron-hadron experiments. The very large $t\bar{t}$ cross sections at the LHC and the FCC-hh make single-**top** production challenging, whereas at the electron-proton colliders single-top production is the dominant top-quark process and can be studied in a cleaner environment [23]. This single-top production could be used to study the top quark spin and polarization to the percent-level [29], as well as for the search of flavor changing neutral currents (FCNC) [22, 29]. In $t\bar{t}$ production, the photons interact with the top quarks and, as a result, the $t\bar{t}\gamma$ magnetic and electric dipole moments could be probed with these e-p colliders [27].

LHeC and FCC-eh reach momentum transfers $Q^2$ that exceed the weak scale $M^2_{W,Z}$ by two orders of magnitude, opening up unique opportunities for precision **electroweak** studies. For the LHeC this has been studied in [27] and according to this study, the light-quark Z-couplings could be measured to a sub-percent level, the mixing angle $\sin^2(\theta_W)$ could be determined to a precision of about $0.000\,15$ and an indirect W-mass determination with a $6\,\mathrm{MeV}$ uncertainty would be possible.

For studies **beyond the Standard Model**, a nominal electron beam energy of $60\,\mathrm{GeV}$ for the LHeC has been considered [23]. For this energy, LHeC, as well as FCC-eh, could prove useful in the search for heavy neutrinos, dark photons, and axion-like particles [23]. Both of these colliders would provide valuably complementary information to the h-h program of HL-LHC or FCC-hh.

# 2 Theory of Accelerator Physics

This chapter provides an overview of the accelerator physics used in this thesis, as well as the frameworks used to generate the data. It is meant to serve as a basic introduction and more details can be found here [30, 31]. The information in this chapter is based on [11, 32–36].

## 2.1 Linear Beam Optics

In circular accelerators and colliders, particles travel together in a beam that is divided into small groups called *bunches*. Within each bunch, the particles have nearly identical energies and remain close together as they circulate. Magnetic fields steer the beam and focus it, while electric fields accelerate or decelerate the particles. The particles travel along the *design orbit*, which is also-called the *reference orbit*, while performing small oscillations. The *reference orbit* corresponds to the trajectory of a particle with the design momentum and no transversal deviations. This is schematically shown with the dashed black circle in figure 4. While the centrifugal force pulls the particles to the outside, the electromagnetic Lorentz force pulls the particles to the inside.

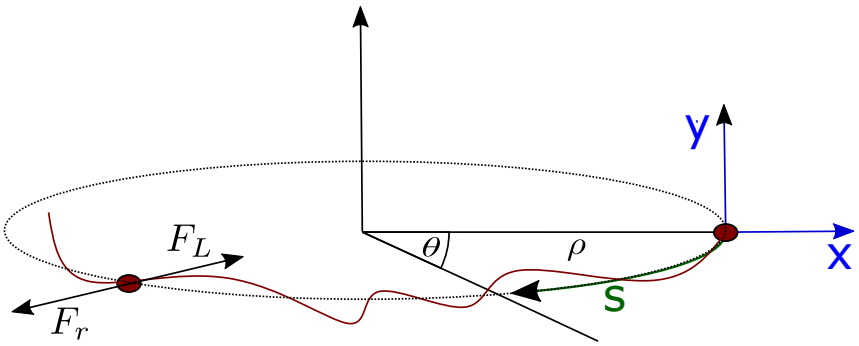


**Figure 4:** Schematic representation of a particle traveling along its reference orbit $s$ (black dashed line) with a radius $\rho$, while performing betatron oscillations. The force which keeps the particle on this track is the Lorentz force $F_L$. The equilibrium of the radial force $F_r$ and the Lorentz force in the inertial system of the particle is shown on the left of the figure. The coordinate system of the particle is indicated in blue and green on the right side of the figure.

In figure 4, the coordinate system used to describe the motions of particles is indicated on the right side. In this reference system the $x$ and $y$ axes correspond to the horizontal and vertical displacement of the particle, along its position $s$ on the orbit.

As particles with a velocity $\vec{v}$ and a charge $q$ pass through a magnetic field of strength $\vec{B}$, they experience the Lorentz force $\vec{F_L}$:

$$\vec{F_L} = q \cdot \left(\vec{E} + \vec{v} \times \vec{B}\right). \tag{1}$$

As can be seen in this equation, the magnetic field strength is multiplied with the velocity of the particles. Since the particles in high-energy accelerators move at velocities close to the speed of light, this term becomes dominant. This is why it is customary to use magnetic fields to steer the particle beam, while electric fields are used to accelerate and decelerate the bunches.

For relativistic particles with a rest mass $m_0$, a velocity $\vec{v}$ and a Lorentz factor $\gamma$, which travel on an orbit of radius $\rho$, the radial force corresponds to:

$$\vec{F_r} = \frac{\gamma m_0 \vec{v}^2}{\rho}. \tag{2}$$

Setting $\vec{F_L} = \vec{F_r}$ and assuming that $\vec{B} \perp \vec{v}$, as well as setting $\vec{E} = 0$ (since only magnetic steering is considered) yields:

$$\frac{\gamma m_0 \vec{v}^2}{\rho} = q \cdot \vec{v} \cdot \vec{B}. \tag{3}$$

By inserting $\vec{p} = \gamma m_0 \vec{v}$, the so-called *beam rigidity* $B \cdot \rho$ can be defined as:

$$B \cdot \rho = \frac{p}{q}. \tag{4}$$

In circular accelerators, the maximal energy that the particles can reach is thus mainly defined by the circumference of the accelerator $\rho$, and the strength of the magnetic field $\vec{B}$. The higher the momentum of the beam, the harder it becomes to bend it and the less flexible it is, hence the term *beam rigidity*.

Equation 4 can be written in more detail for the horizontal displacement $x$ for a particle of charge $q = e$, that moves along the orbit $s$: $\vec{v} = (0, 0, v_s)$. The magnetic field is applied in the transversal planes: $\vec{B} = (Bx, By, 0)$. Calculating the Lorentz force and setting its horizontal component $F_x$ equal to the radial force $F_r$ yields:

$$\frac{1}{\rho} = \frac{e}{p} B_y. \tag{5}$$

This expression can be expanded with a Taylor series in the proximity of the reference orbit $s$:

$$\frac{e}{p} \cdot B_y(x) = \frac{e}{p} \cdot B_{y0} + \frac{e}{p} \cdot \frac{\mathrm{d}B_y}{\mathrm{d}x} x + \frac{e}{p} \cdot \frac{1}{2!} \frac{\mathrm{d}^2 B_y}{\mathrm{d}x^2} x^2 + \frac{e}{p} \cdot \frac{1}{3!} \frac{\mathrm{d}^3 B_y}{\mathrm{d}x^3} x^3 + \mathcal{O}(x^4). \tag{6}$$

Each of the terms in this equation can be considered as a multipole, which has a certain effect on the beam. By normalizing over the beam rigidity $p/e$, and using the terminology used to describe the corresponding field strength of a multipole, this equation can be written as:

$$\frac{e}{p} \cdot B_y(x) = \underbrace{\frac{1}{\rho}}_{\text{dipole}} + \underbrace{k_1 \cdot x}_{\text{quadrupole}} + \underbrace{\frac{1}{2!} k_2 \cdot x^2}_{\text{sextupole}} + \underbrace{\frac{1}{3!} k_3 \cdot x^3}_{\text{octupole}} + \mathcal{O}(x^4). \tag{7}$$

In this equation $k_i$ represents the normalized field strength of the corresponding multipole. Each multipole influences the beam in a certain way. The **dipoles** are used to steer the beam. This is particularly important in circular accelerators, where the maximal energy of the beam is defined by the circumference, as well as the strength of the applied dipoles, as can be seen in equation 4. The **quadrupoles** in an accelerator are used to focus the beam in one transverse plane and defocus in the other. In a system of magnets which only uses dipoles and quadrupoles, one can speak of *linear beam optics* as the highest dependence of the transversal beam displacement $x$ is linear. The **sextupoles** are used to correct the *chromaticity* caused by off-momentum particles passing through quadrupoles (see section 2.4). Octupoles and higher order multipoles are used to control beam stability and to correct field errors. They will not be discussed here and more information can be found for example in [30, 31].

Circular accelerators are usually filled with as many dipoles as possible in order to reach a high particle momentum (see equation 4). Quadrupoles are placed in between the dipoles in an alternating sequence: one quadrupole that focuses in the horizontal plane (F), a drift space (O which may also contain dipoles or other elements) and one quadrupole which defocuses in the horizontal plane, but focuses in the vertical plane (D). This repeated pattern is known as a *FODO*

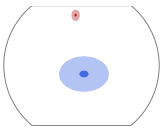

cell, where any periodically repeated structure of elements in an accelerator is referred to as *cell*.

While there are certain regions in accelerators which are used for particular operations, such as the interaction region for collisions, or the radio frequency cavities for acceleration, the majority of the accelerator consists of repeating FODO cells.

### 2.1.1 Hill's Equation

Most particles that move along the orbit do not behave as ideal particles and perform so-called *betatron oscillations* along this orbit in both transversal directions. This is shown schematically in figure 4, as well as figure 5.

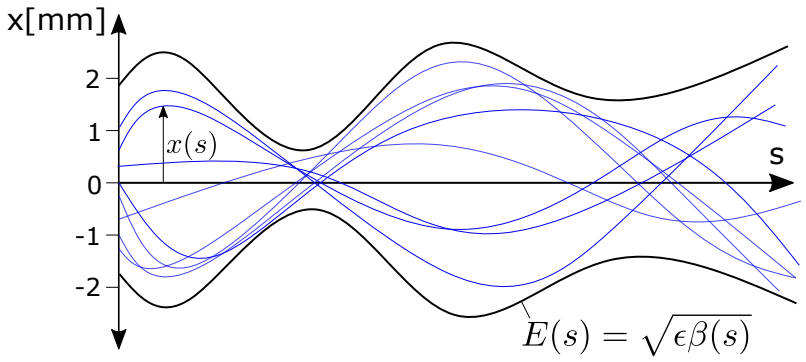


**Figure 5:** Representation of several particles performing betatron oscillation in the horizontal plane $x$, along the reference orbit $s$. The particles are confined within the beam envelope $E(s) = \sqrt{\varepsilon\beta(s)}$.

Small oscillations can be described by *Hill's equation* of motion:

$$\frac{\mathrm{d}^2x(s)}{\mathrm{d}s^2} - k(s)x(s) = 0. \tag{8}$$

In this equation $x(s)$ describes the transversal displacement at a position $s$ along the orbit $s$ and $k(s)$ represents the focusing strength of the quadrupoles.

The solution of this equation is:

$$x(s) = \sqrt{\varepsilon}\sqrt{\beta(s)}\cos\left(\Psi(s) + \Phi\right) \tag{9}$$

with the betatron phase advance $\Psi(s)$:

$$\Psi(s) = \int_0^s \frac{\mathrm{d}\sigma}{\beta(\sigma)}. \tag{10}$$

In these equations $\beta(s)$ represents the *amplitude function*, which depends on the position along the orbit $s$, as well as on the focusing strength of the quadrupoles at this position $k(s)$ [37]:

$$\frac{1}{2}\beta''(s) - \frac{1}{4}\frac{\left(\beta'(s)\right)^2}{\beta(s)} + k(s)\,\beta(s) = 1. \tag{11}$$

It is sometimes referred to as the beta function and describes the amplitude of the betatron oscillation of a particle. Though the particles perform oscillations of different amplitudes, they all stay within the so-called *beam envelope* $E(s) = \sqrt{\beta(s)\varepsilon}$. This is represented schematically in figure 5. In this envelope, the *emittance* $\varepsilon$ is only dependent on the energy of the particles. In simple terms the emittance measures the "chaos" of the particle beam. The smaller the emittance, the more focused the particle beam and vice versa. $\phi$ represents the initial phase of the particle.

The total amount of betatron oscillations performed in one turn is referred to as the *betatron tune* $Q_{x,y}$.

$$Q_{x,y} = \oint \frac{1}{2\pi}\frac{\mathrm{d}\sigma}{\beta(\sigma)}. \tag{12}$$

In this equation $x, y$ represent the corresponding plane of the betatron oscillation for the horizontal and the vertical tune.

### 2.1.2 Courant-Snyder Parameters and the Phase Space Ellipse

The previously presented solution for Hill's equation (see equation 9) can be expressed in the $(x, x')$-phase space, which is sometimes also referred to as the $(x, p_x)$-phase space. Here $x$ represents the transverse position of the particle and $x' = dx/ds$ represents the transverse divergence. The divergence describes the

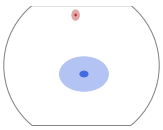

slope of the trajectory and is therefore also referred to as the transverse angle (for small angles $x' \approx \vartheta$). The phase-space can be defined by introducing the *Courant-Snyder parameters*, which are also-called *Twiss parameters*: $\alpha(s)$, $\beta(s)$ and $\gamma(s)$. The amplitude function $\beta(s)$ has already been introduced in section 2.1.1. The other two functions are defined as such:

$$\alpha(s) = -\frac{\beta'(s)}{2} \tag{13}$$

and

$$\gamma(s) = \frac{1 + \alpha^2(s)}{\beta(s)}. \tag{14}$$

$x'(s)$ can then be expressed as:

$$x'(s) = -\frac{\sqrt{\varepsilon}}{\sqrt{\beta(s)}}[\alpha(s)\cos(\Psi(s) + \Phi) + \sin(\Psi(s) + \Phi)]. \tag{15}$$

With equation 9 and equation 15 the *phase space ellipse* can be defined as:

$$\gamma(s)x^2 + 2\alpha(s)x(s)x'(s) + \beta(s)x'^2(s) = \varepsilon. \tag{16}$$

This is the equation for an ellipse with an area of $A = \pi\varepsilon$. This ellipse in the $(x, x')$-phase space is shown in figure 6.

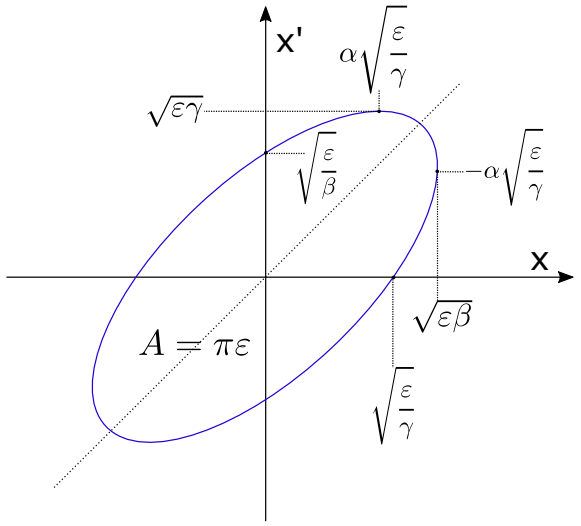


**Figure 6:** Phase space ellipse in the $(x, x')$-plane. The Courant- Snyder Parameters $\alpha$, $\beta$ and $\gamma$ define the shape of the ellipse. The area $A = \pi\varepsilon$ is constant for all particles that are subject to canonical equations of motion.

According to *Liouville's Theorem*: *the phase space distribution function is constant along the trajectories of a system, if all the particles follow the canonical equations of motion* [30]. This means that the area inside the ellipse $A = \pi\varepsilon$ stays constant in a conservative system. As a result, a beam with a small surface $x = \sqrt{\beta\varepsilon}$ will have a correspondingly large divergence $x' = \sqrt{\varepsilon\gamma}$ and vice versa. This trade-off imposes strong constraints on the design of colliders.

### 2.1.3 Gaussian Beam Profile and Aperture

The emittance $\varepsilon$ is used to define the phase space area of a single particle. It therefore defines the envelope of this particle $E(s) = \sqrt{\beta(s)\varepsilon}$. When looking at a particle beam with many particles, the emittance needs to be defined statistically.

In particle accelerators, the transverse charge distribution $\rho\,(x, y)$, which shows how many particles are located at each transverse position, is usually assumed to be of Gaussian shape [38]:

$$\rho\,(x, y) = \frac{Ne}{2\pi\sigma_x\sigma_y}\exp\left(-\frac{x^2}{2\sigma_x^2} - \frac{y^2}{2\sigma_y^2}\right). \tag{17}$$

This distribution is plotted for the horizontal plane $x$ in figure 7. $N$ represents the number of particles with a charge $e$ in the beam and $x, y$ the transverse position of the particles.

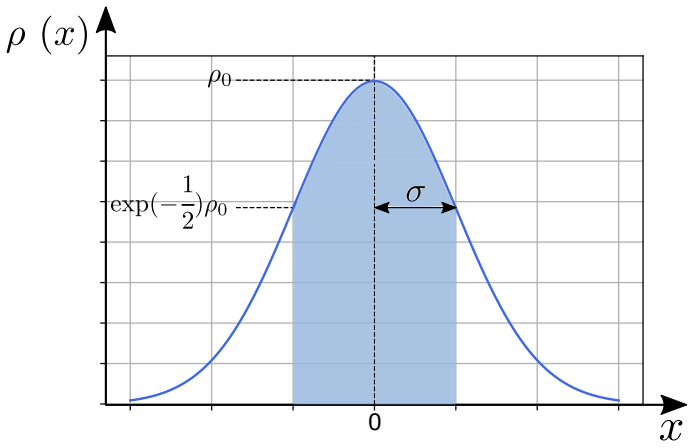


**Figure 7:** Exemplary horizontal charge distribution of a Gaussian particle beam as a function of the horizontal position of the particles $x$. One standard deviation $\sigma$ is marked in the plot in the highlighted area.

In figure 7, $\sigma_{x,y}$ represents one standard deviation of this charge density distribution. The emittance $\varepsilon_{\mathrm{std}}$ can then be defined as the emittance of the particles that are positioned exactly one standard deviation away (shaded area in figure 7) from the center. With this emittance, the beam size of these particles can be defined as:

$$\sigma_{x,y}(s) = \sqrt{\varepsilon_{\mathrm{std}} \beta_{x,y}(s)}. \tag{18}$$

In this equation, the beta function $\beta_{x,y}(s)$ represents the amplitude of the beam at the position $s$ in the corresponding plane. $\sigma_{x,y}(s)$ thus represents the beam envelope for $68\,\%$ of the particles in the beam. In this PhD, the emittance is defined over equation 18 and will be written as $\varepsilon$ without the index $\mathrm{std}$.

In equation 18, it can be seen that the size of the beam depends strongly on the amplitude function $\beta(s)$. If there is enough space for the beam, even particles with large oscillation amplitudes can circulate safely. The *aperture* is defined as the mechanical available space for the beam within the structure of the accelerator and is often expressed in units of the beam's standard deviation.

### 2.1.4 Beam Envelope and Beta Function Evolution with Matrix Propagation

As the particles propagate through the collider, they pass through different magnetic multipoles. Such a sequence of arranged magnets that make up the accelerator is referred to as *lattice*. The multipoles are placed in a manner, that they influence the beam differently depending on the desired behavior of the beam at this particular position in the lattice (beam collisions, momentum cleaning, acceleration, etc.). The amplitude function $\beta(s)$ is then manipulated to keep as many particles as possible on a stable trajectory and to achieve the most collisions. It can therefore reach very different amplitudes along the orbit and as a consequence, lead to different beam sizes.

It is possible to analytically calculate the propagation of the particles throughout the lattice with the help of matrix multiplications. The trajectory vector of the particle in phase space can be written as:

$$\mathbf{X} = \begin{pmatrix} x \\ x' \end{pmatrix}.$$

The beta matrix $\mathbf{B}$ is defined as:

$$\mathbf{B} = \begin{pmatrix} \beta & -\alpha \\ -\alpha & \gamma \end{pmatrix} \tag{19}$$

with the determinant $\det(\mathbf{B}) = 1$. In this matrix $\alpha, \beta, \gamma$ express the Courant-Snyder parameters of a particle. Using this matrix, the beam optics can be expressed compactly at a certain point along the lattice. Calculating the product:

$$\mathbf{X^T} \cdot \mathbf{B^{-1}} \cdot \mathbf{X} = \gamma x^2 + 2\alpha x x' + \beta x'^2 = \varepsilon \tag{20}$$

shows that it corresponds to the beam emittance from equation 16 and thus this product is constant along the lattice for canonical motions. While the total area within the phase space ellipse is conserved due to *Liouville's Theorem*, the Courant-Snyder parameters do change along the lattice.

The impact on the optics of the beam of different elements in the accelerator lattice can be expressed with a matrix $\mathbf{M}$. This matrix can represent a single element or the multiplication of several elements that the particles pass through. Using

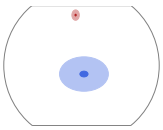

the beta matrix at a start position $\mathbf{B_0}$ at $s_0$, the matrix $\mathbf{B_1}$ at a position $s_1$, after passing through several elements, represented with the transfer matrix $\mathbf{M}$, can be calculated with:

$$\mathbf{B_1} = \mathbf{M} \cdot \mathbf{B_0} \cdot \mathbf{M^T}. \tag{21}$$

With this equation it is possible to calculate the optical functions at any given point in the accelerator.

### 2.1.5 Mini $\beta$ Insertions

When the beam propagates through the accelerator, it is steered by the dipoles and focused by the quadrupoles. But once it reaches the interaction region, it needs to enter the particle detector in order to collide with the other beam or a fixed target in its center. This requires a substantial magnet-free region, meaning that no focusing elements are present over the distance of the detector. The beam therefore travels through a drift space all the way to the interaction point (IP). This interaction point acts as a symmetry point in the amplitude function $\beta$.

The shape of the $\beta$ function around a symmetry point in the lattice can be determined by applying equation 21 for the propagation of the optical functions. This point is conventionally marked with a superscript $^*$. As this point is symmetric, $\alpha^*$, which is proportional to the derivative of $\beta^*$, equals zero. Using equation 19and equation 21, the beta matrix $\mathbf{B_1(s)}$ at a distance $s$ from the symmetry point can be calculated:

$$\mathbf{B_1(s)} = \mathbf{M} \cdot \mathbf{B_0} \cdot \mathbf{M^T} = \begin{pmatrix} 1 & s \\ 0 & 1 \end{pmatrix} \cdot \begin{pmatrix} \beta^* & 0 \\ 0 & \frac{1}{\beta^*} \end{pmatrix} \cdot \begin{pmatrix} 1 & 0 \\ s & 1 \end{pmatrix} = \begin{pmatrix} \beta^* + \frac{s^2}{\beta^*} & \frac{s}{\beta^*} \\ \frac{s}{\beta^*} & \frac{1}{\beta^*} \end{pmatrix}. \tag{22}$$

In this equation $\beta^*$ represents the optical amplitude function at the interaction point. The matrix $\mathbf{M}$ represents the propagation of the beam through a drift space. Using equation 19 the shape of $\beta(s)$ and $\alpha(s)$ at a distance $s$ from the interaction point can be deduced to be:

$$\beta(s) = \beta^* + \frac{s^2}{\beta^*} \tag{23}$$

and

$$\alpha(s) = -\frac{s}{\beta^*}. \tag{24}$$

The amplitude function $\beta$ is plotted for the x-plane in figure 8 for different sizes of $\beta^*$. Note that this is not a representation of the actual beam size $\sigma = \sqrt{\beta(s)\varepsilon}$, because the geometrical emittance is extremely small and the amplitude function can reach very large values. The shape of these amplitude functions is a direct result of *Liouville's Theorem*, see figure 6. When the beam is squeezed to lower $\beta^*$ values in order to reduce its transverse size and thereby maximizing the probability of collisions, the total area within the phase space must be conserved. As a consequence, the divergence of the beam increases, leading to higher peaks upstream and downstream of the interaction point (see equation 23). Therefore, the final focusing magnets before the interaction point need to have a large aperture to accommodate the beam.

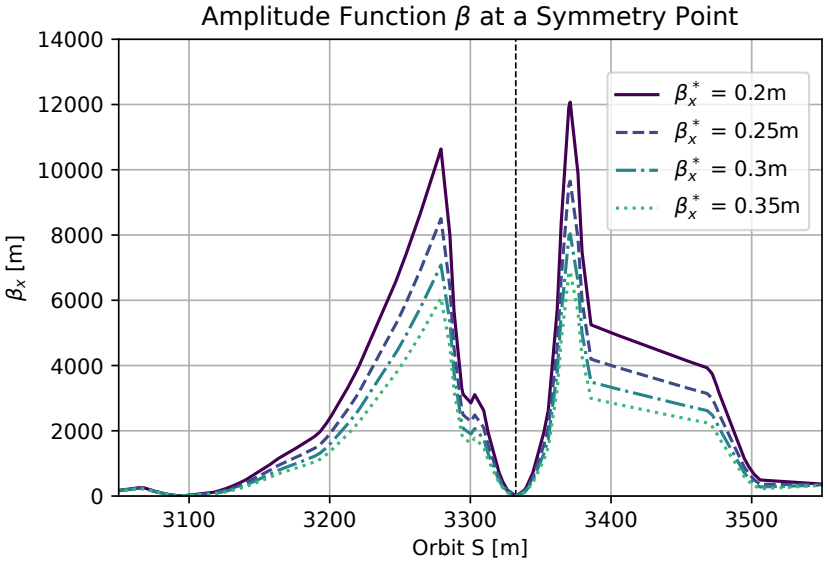


**Figure 8:** Plot of the horizontal amplitude function $\beta_x$ around an interaction point of the LHC. The position of the interaction point is marked with a black dashed line. Different beam amplitudes $\beta_x^*$ at the IP are plotted.

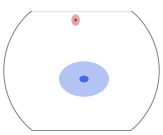

## 2.2 Luminosity

The primary parameter determining the physics potential of a collider is the energy of the colliding particles. A key figure of merit used to quantify the collision production rate is the so-called *luminosity* $\mathcal{L}$. Events with a cross section $\sigma_p$ are linked to their production rate $\mathrm{d}R/\mathrm{dt}$ via the luminosity $\mathcal{L}$:

$$\frac{\mathrm{d}R}{\mathrm{dt}} = \mathcal{L} \cdot \sigma_p. \tag{25}$$

Luminosity quantifies the number of collisions produced per unit area per unit time. In the design of a collider, maximizing the luminosity is therefore essential to increase the probability of observing physics events.

For the collision of two round Gaussian beams of the same size at the interaction point, the luminosity $\mathcal{L}$ can be calculated using the following equation:

$$\mathcal{L} = \gamma \frac{n_b \cdot N_1 \cdot N_2 \cdot f_{rev}}{4 \cdot \pi \cdot \sigma^{*2}} \cdot G \cdot B \cdot F. \tag{26}$$

Here, $n_b$ describes the number of bunches, $N_1$ and $N_2$ describe the amount of particles per bunch for the corresponding beam, and $f_{rev}$ is the revolution frequency. $\sigma^*$ represents the beam size at the interaction point, while $G$ represents the geometric reduction factor.

This reduction factor $G$ expresses the loss of luminosity due to the geometry of the collisions. It therefore reaches a value between $0$ and $1$. Usually, the particle bunches collide at an angle and as a result, the overlap of the bunches is effectively smaller and the luminosity reduced. Additionally, the overlap of the bunches at the collision is reduced due to the so-called *hourglass effect*. In figure 8 it can be seen that the smallest $\beta^*$ value is positioned precisely at the position of the interaction point. However, not all particles collide exactly at the interaction point. Some interact slightly upstream or downstream, where the beam size is larger and the resulting luminosity is reduced.

A further factor that reduces the luminosity in equation 26 is the filling factor $F$. As the particles propagate in their bunches through the accelerator complex, they move in a so-called bunch train. This means that a certain gap is left at the end of the train, and that not the whole accelerator is filled with particle bunches. These gaps can be useful for injection and dumping, for example.

The beam-beam correction factor $B$ accounts for changes in the luminosity due to the beam-beam effect (see section 6.3.1).

Looking at equation 26, it becomes clear why increasing the luminosity using beam optics is challenging. To increase the luminosity, the transverse beam size $\sigma^* = \sqrt{\beta^* \cdot \varepsilon}$ should be minimized. However, due to *Liouville's Theorem* and the resulting conservation of phase space, the beam size increases upstream and downstream of the interaction point, as the divergence grows. Consequently, one of the main limitations of colliders is the available aperture of the magnets in the final focusing system.

### 2.2.1 Beam-Beam Effects

Another major limitation of the luminosity in high energy colliders is the beam-beam effect. The beams carry a large amount of charge concentrated over a small area, leading to strong electromagnetic interactions between them. These forces between the particle beams are non-linear and can be focusing or defocusing, depending on the charge of the beams. For opposite charges, the beam-beam force has a focusing effect and vice versa.

The beam-beam effects are strongest when the beams collide. This is called the *short range* beam-beam effect. The strong interaction can result in the expansion of the other beam, called a *beam blow up* and this in turn leads to a significant decrease in luminosity. The *long range* effects refer to the beam-beam interaction of the beams, as they pass next to each other without colliding (for example during the energy ramp up, the beams pass next to each other in the interaction regions without colliding). These so-called *parasitic* encounters have a smaller effect on the beams, but they occur on every turn and affect many particles. Over time they lead to orbit distortions, tune shifts and beam instabilities (see section 2.3).

For round Gaussian beams, the non-linear beam-beam force $F_u(r)$ at a distance $r = \sqrt{x^2 + y^2}$ from the center of the beam, in the transverse direction $u$ (where $u = x, y$) can be calculated using:

$$F_u(r) = -\frac{Ne^2(1+\beta^2)}{2\pi\varepsilon_0}\frac{u}{r^2}\cdot\left[1-\exp(-\frac{r^2}{\sigma_u})\right]. \tag{27}$$

In this equation, $N$ denotes the number of particles per bunch in the opposing beam, $e$ is the elemental charge, and $\beta$ represents the relativistic velocity factor:

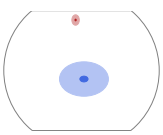

$\beta = v/c$. The quantity $\varepsilon_0$ is the vacuum permittivity, while $\sigma_u$ represents the transverse beam size in the corresponding direction. The distance $r$ from the center of the beam defines the magnitude of the radial beam force, whereas the coordinate $u$ specifies its component along the x- or y-direction.

In figure 9, the horizontal component of the beam-beam force $F_x$ is plotted as a function of the transverse displacement $x$. For particles with $x > 0$, an attractive beam-beam force interaction pulls the particle back toward the beam center, whereas a repulsive interaction pushes it further outward to larger $x$.

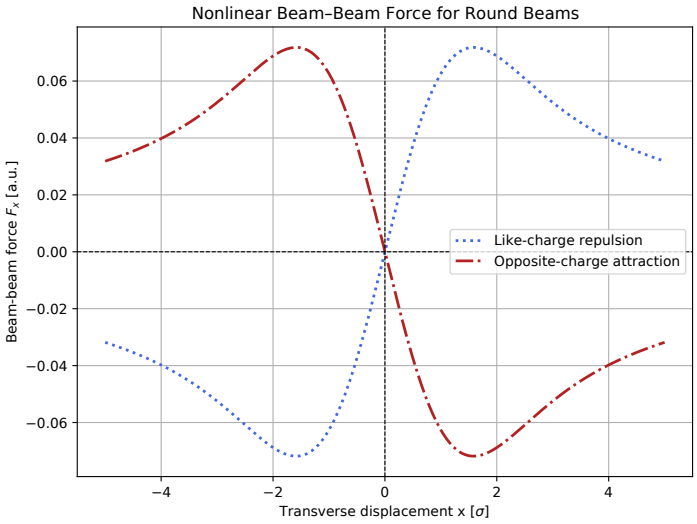


**Figure 9:** Plot of the horizontal component of the beam-beam force $F_x$ as a function of the horizontal particle displacement $x$, expressed in units of beam size $\sigma$. The force is shown for beams of opposite charges (red) and for beams with the same charge (blue). At small transverse displacements, the force behaves approximately linearly.

In figure 9 it can be seen that at very low displacements ($x \approx 0$), the beam-beam force behaves linearly. At higher amplitudes the force becomes non-linear, reflecting the Gaussian behavior of the beam distribution. The non-linear shape of the form implies the presence of higher order multipoles, which can lead to tune shifts and as a result drive many resonances and ultimately lead to particle loss (see 2.3).

For small displacements $x$, the effect of the beam-beam force on the beam can be expressed using the *linear beam-beam parameter* $\xi_u$:

$$\xi_u = \frac{N r_0 \beta_u}{2\pi\gamma\,\sigma_u(\sigma_x + \sigma_y)}, \qquad u = x, y. \tag{28}$$

In this equation $r_0$ represents the classical particle radius and $\beta_u$ represents the amplitude function with the corresponding beam size $\sigma_u$. The parameter $\gamma$ denotes the relativistic Lorentz factor.

For small values of $\xi_{x,y}$ and tune values that are far away from any driving resonances, the induced tune shift can be approximated as: $\xi_{x,y} \approx \Delta Q_{x,y}$ for the corresponding transverse plane.

## 2.3 Linear Beam Imperfections

The magnets placed inside an accelerator are subject to different imperfections. Two effects caused by linear beam imperfections will be briefly explained here, as they impact the work in this PhD.

The main errors affecting the magnets are field errors and alignment errors. In the LHC the magnets are aligned up to a precision of $0.1\,\mathrm{mm}$ [39]. A particle injected with a transverse offset does not pass through the center of the magnet. In an ideal machine without imperfections, this is not an issue as this particle will simply oscillate around the design orbit. However, if a magnet is slightly displaced from its nominal position, the design orbit itself is shifted. As a result, the particle oscillates around an orbit different from the design orbit, called the *closed orbit*. In more severe cases the particle might hit the mechanical aperture of the accelerator, leading to beam loss.

**Feed Down Effect** If a particle passes through a misaligned magnet, it is subject to the so-called *feed down effect*. Higher-order magnetic fields generate additional lower-order field components. For example, a sextupole with an offset therefore behaves as a combination of sextupole, a quadrupole, and a dipole. Likewise, an offset quadrupole produces an additional effective dipole component.

For horizontal offsets, the generated lower order multipoles act in the horizontal plane. For vertical offsets, additional *skew* components can be created, meaning that also horizontal multipoles are created. This introduces so-called *coupling* between the transversal planes.

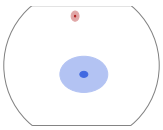

**Tune Resonances** The tune defines the amount of betatron oscillation around the closed orbit in each transversal plane, see equation 12. In circular colliders the optimal tune, the *working point*, is usually an irrational number. If the tune were an integer, the particle would encounter the same magnetic imperfections at the same phase on every turn. This repeated coherent kick can drive a resonance, leading to a growth in oscillation amplitude and ultimately to particle loss.

Since there are two tunes in the accelerator (one in each plane), two working points need to be chosen which avoid resonances in both planes. In the higher order multipoles the resonances can even be coupled, as the position of the beam in one plane will affect how strongly a magnetic field impacts the beam in the other plane.

The resonance condition is therefore:

$$mQ_x + nQ_y = p. \tag{29}$$

In this equation $m$, $n$ and $p$ represent integers, while $Q_{x,y}$ represents the working point in the corresponding plane. The order of the resonance is defined as: $|m| + |n|$. A plot of the resonances up to the third order can be seen in figure 10.

In an ideal case, a working point is chosen that does not touch any resonance line. However, the effect of a resonance diminishes with its order, so it is particularly important to select working points away from resonances up to the third order.

The quadrupoles in a collider are used to focus the beam in both transversal planes. If the strength of a quadrupole is changed due to a field error, the focusing changes, which in turn changes the tune. The tune shift is approximately:

$$\Delta Q = \frac{1}{4\pi} \int_{s_0}^{s_0+l} \Delta k(s)\beta(s)\mathrm{ds}. \tag{30}$$

In this equation $\Delta Q$ represents the tune shift, $\Delta k(s)$ represents the quadrupole error at a position $s$ and $\beta(s)$ the amplitude function at this position. From this equation it can be seen that the caused tune shifts are particularly impactful in regions with high amplitude functions. It is therefore important to have very precise fields in the interaction region, as the amplitude function reaches its highest value just before the collision (see section 2.1.5).

It is important to correct these tune shifts, as they can push the working points towards the resonances.

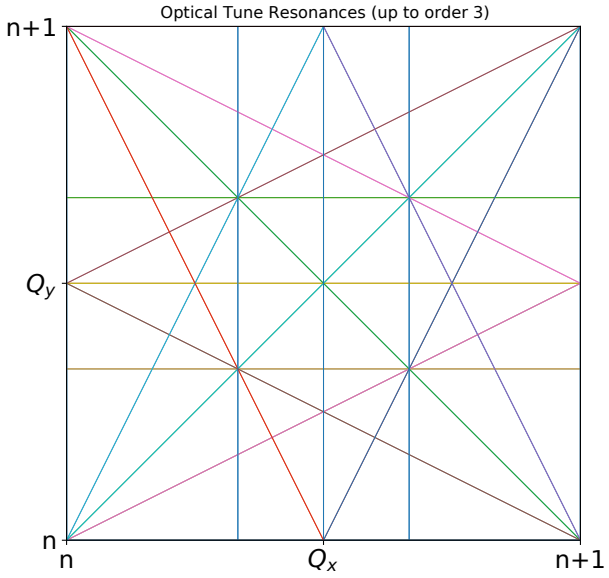


**Figure 10:** Betatron tune diagram showing the resonances up to the third order for both transversal planes. It is crucial to choose working points that are as far away as possible from these resonances.

## 2.4 Momentum Spread, Dispersion and Chromaticity

Not all particles in the accelerator move with the design momentum $p_0$. Usually the particles have slightly different momenta $p$. The momentum spread $\Delta p$ can be expressed as:

$$\Delta p = p - p_0 \ll p_0 \tag{31}$$

As a result, Hill's equation (see equation 8) needs to be modified to also consider off-momentum particles [40]:

$$\frac{\mathrm{d}^2 x(s)}{\mathrm{d}s^2} - k(s)x(s) = \frac{1}{\rho} \cdot \frac{\Delta p}{p} \tag{32}$$

In this equation, $x(s)$ represents the transverse displacement of the particle at a position $s$, $k(s)$ expresses the quadrupole strength, and $\rho$ the bending radius of

the accelerator. The general solution to this equation $x_g(s)$ can then be written as:

$$x_g(s) = x(s) + x_D(s) = x(s) + D(s)\frac{\Delta p}{p}. \tag{33}$$

In this equation, $x(s)$ represents previously calculated solution to *Hill's equation* (see equation 9), and $D(s) = \frac{x_D(s)}{\Delta p/p}$ represents the *dispersion*, which quantifies how the transverse orbit changes due to a relative momentum deviation. It therefore defines a new closed orbit for particles with momenta different from the design momentum, called the *off-momentum orbit* or *dispersion orbit*. While $D(s)$ describes the offset of the position of the transverse particle, the derivative function $D'(s)$ describes the corresponding angle offset. The dispersive angle is given by:

$$D'(s) = x'_D(s)\frac{\Delta p}{p}. \tag{34}$$

Additionally to propagating on a distorted orbit, the transversal size of the beam $\sigma_x$ increases for off-momentum particles:

$$\sigma_x = \sqrt{\varepsilon\beta_x + (D\sigma_\delta)^2}. \tag{35}$$

Here, $\beta_x$ represents the amplitude function of the beam, $\varepsilon$ represents the emittance, and $\sigma_\delta$ denotes the relative momentum spread of the beam: $\sigma_\delta = \Delta p/p$.

It is therefore important to achieve $D = 0$, as well as $D' = 0$ at the interaction points, to achieve the lowest beam size and hence the highest luminosity. However, in the momentum cleaning insertion, a finite dispersion is intentionally generated to amplify the transversal position of the very off-momentum particles, so that they can be scraped off with the use of collimators.

When off-momentum particles pass through a quadrupole, they experience a different effective focusing strength. This can be seen schematically in figure 11. The particles with a higher momentum are focused too little, while the particles with a lower momentum are focused too strongly. This shift in focusing leads in turn to a shift in the betatron tune. The resulting momentum dependence of the tune is quantified by the *chromaticity* $\xi$ (not to be confused with the beam-beam parameter, which traditionally uses the same symbol):

$$\xi = \frac{\Delta Q}{\Delta p/p} = \frac{1}{4\pi} \oint k(s)\beta(s)\mathrm{ds}. \tag{36}$$

In equation 36 it can be seen that the tune shift is particularly strong at locations with large quadrupole gradients $k(s)$ and high amplitude functions $\beta(s)$. In this equation the chromaticity is calculated by integrating over all quadrupoles in the accelerator. This is necessary as the off-momentum particles pass through every quadrupole with a field error.

Different values of the tune are reached depending on the energy of the particles. If these lie on tune resonances, the chromaticity can lead directly to particle losses.

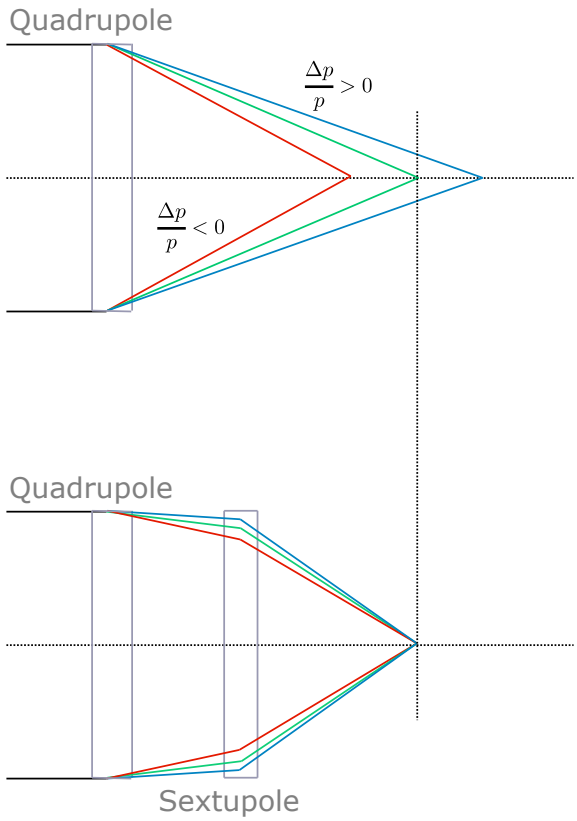


**Figure 11:** Schematic representation of chromaticity for particles with different momenta. At the top, three trajectories are shown for particles with $\Delta p/p < 0$ (red), $\Delta p/p = 0$ (green) and $\Delta p/p > 0$ (blue). Only the particles with design momentum are focused at the nominal focal point (marked with a dashed line). In the lower part of the figure, a sextupole placed downstream of the quadrupole, corrects the chromaticity by restoring the focal point for off-momentum particles. Figure inspired by [41].

It is therefore necessary to control the chromaticity. This is possible with the introduction of sextupoles. The strength of the focusing field of a sextupole increases with the transversal position of the particle inside the sextupole magnet. With sextupoles, the off-momentum particles are focused more strongly the more their dispersive orbit differentiates from the design orbit. Particles which pass right through the middle of the sextupole do not see a field. This can be seen in the lower part of figure 11. The drawback of using these sextupoles is that not only off-momentum particles are focused differently, but also particles with high amplitudes. As a result, these particles can be lost. This effectively shrinks the aperture available to the beam. This aperture, which is determined not only by the linear optics but also by considering higher order magnetic fields, as well as machine imperfections, is referred to as the *dynamic aperture*. It can be determined by performing so-called *particle tracking simulations*.

## 2.5 Frameworks for the Data Generation

This section provides an overview of the computational frameworks used in this thesis to generate the beam optics and the tracking simulation data.

### 2.5.1 MAD-X

All of the optics calculations in this thesis have been performed using the MAD-X framework (Methodical Accelerator Design -X) [42]. This software is developed at CERN and is used worldwide for the design and optimization of particle accelerators. MAD-X computes the beam optics and particle trajectories based on the sequence of magnetic elements and with the use of matrix calculations.

Fully defining a beam optics requires setting the parameters summarized in table 1. These include the Courant-Snyder parameters $\beta_{x,y}$ and $\alpha_{x,y}$, and the phase advances $\mu_{x,y}$ in both transversal planes, as well as the horizontal dispersion $D_x$ and its derivative $D'_x$.

It is possible to adjust the optical functions at a specific location by changing the strengths of the quadrupoles upstream. This is essential for example at the interaction points, but also in general to ensure that the beam stays within the aperture. Using the matrix formalism described in section 2.1.4, MAD-X applies different optimization routines to iteratively adjust the quadrupoles strengths until the right conditions in the accelerator are met. This numerical computation is called *optics matching*.

**Table 1:** Optical parameters required to fully define the beam optics in the horizontal and vertical planes.

| Parameter | Horizontal | Vertical |
|---|---|---|
| Amplitude function | $\beta_x$ | $\beta_y$ |
| Alpha function | $\alpha_x$ | $\alpha_y$ |
| Phase Advance | $\mu_x$ | $\mu_y$ |
| Dispersion | $D_x$ | - |
| Derivative of the Dispersion | $D'_x$ | - |

### 2.5.2 Xsuite

As higher order, non-linear magnetic fields and imperfections are introduced into the accelerator lattice, it becomes impossible to calculate the stable trajectory of the particles analytically. Numerical simulations are therefore used to determine the stability of particles over many turns and the resulting *dynamical aperture*. These *tracking simulations* numerically integrate the equations of motion for each particle, considering the actual magnetic and electric fields, nonlinearities, and imperfections in the lattice.

The tracking calculations presented in section 7 were performed using the *Xsuite* framework [43]. Xsuite provides a set of tools for numerical particle tracking, particularly suited for non-linear beam dynamics studies. In this thesis, the tracking simulations were executed on parallelized GPUs to handle the large amount of turns the particles performed. Xsuite is optimized for such parallel computation and was therefore used to complement the lattice design calculations carried out with MAD-X.

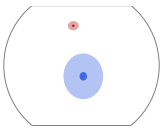

# 3 Concurrent Operation of LHeC and HL-LHC

This chapter defines the goal of this PhD. It briefly summarizes the previous work on the Large Hadron electron Collider (LHeC) study and explains how this PhD makes a meaningful contribution to it.

## 3.1 The Large Hadron electron Collider Study

The first collider to realize high-energy electron-proton (e-p) collisions in order to investigate deep inelastic scattering physics (DIS) was the German Hadron Elektron RingAnlage (HERA) [44]. With a circumference of $6.3\,\mathrm{km}$, it reached final energies of $27.6\,\mathrm{GeV}$ for the electrons and $920\,\mathrm{GeV}$ for the protons [45]. At its peak performance, this resulted in center of mass energies of $318\,\mathrm{GeV}$. Following its footsteps, the LHeC is a design study which investigates the possibility of performing high luminosity electron-proton collisions in one of the four interaction points of the LHC. LHeC's center of mass energy would exceed that of HERA by a factor of 3 [11], realizing e-p collisions of $1.2\,\mathrm{TeV}$.

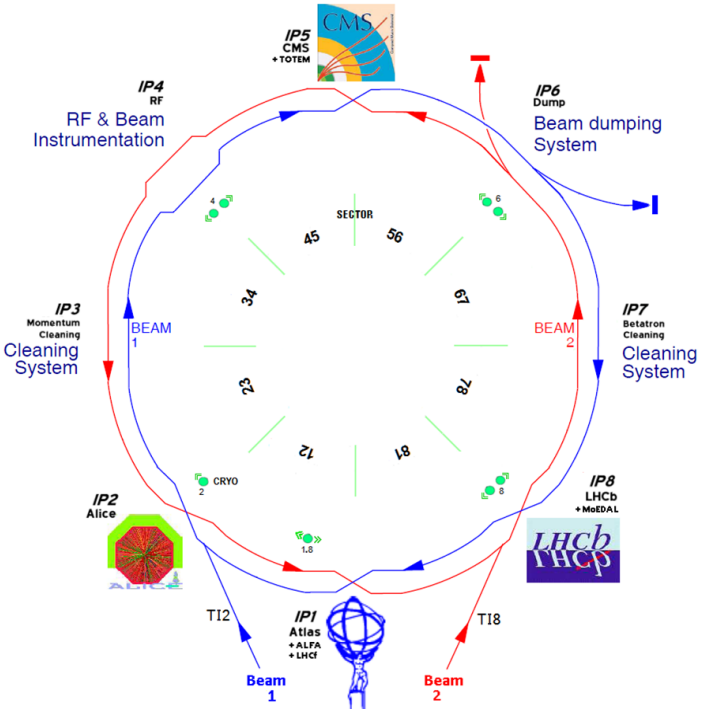


**Figure 12:** Schematic view of the large hadron collider. It shows the two circulating proton beams, as well as the main components of this collider. Figure adapted from [46].

During LHC operation, two hadron beams circulate through the collider, see figure 12. The beam circulating clockwise is traditionally referred to as beam 1 (B1), while the beam circulating counter clockwise is referred to as beam 2 (B2). The two hadron beams collide in four interaction points (IP) of LHC: in IP1 in the ATLAS detector, in IP2 in the ALICE detector, in IP5 in the CMS detector, and finally in IP8, where the LHCb detector is located. The two hadron beams circulate in their corresponding beam pipes and only shortly share the same beam pipe in the four interaction regions (IR) in order to collide.

The core concept of the LHeC is to add an energy recovery linac (ERL) to the LHC complex. This ERL would accelerate electrons to collide them with proton B1 of LHC. In the suggested design for LHeC, IP2 would be used to perform electron-proton collisions. A possible layout of one design for the LHeC can be seen in figure 13.

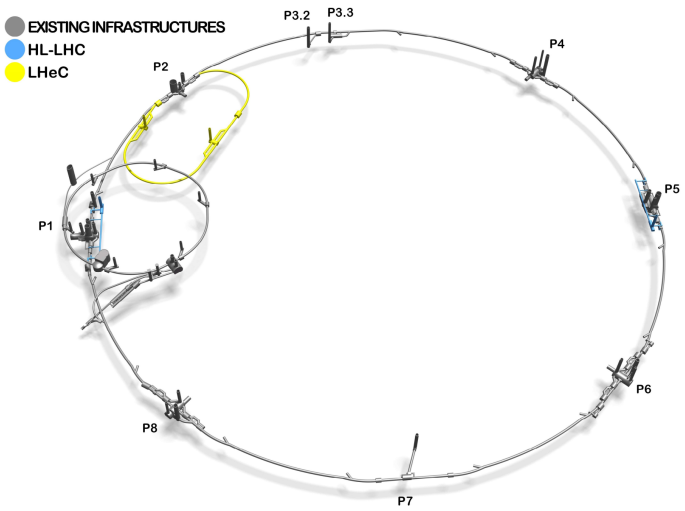


**Figure 13:** Schematic view of a possible layout for LHeC. It displays the energy recovery linac (yellow) and the super proton synchrotron with the LHC (grey). The high luminosity upgrade in IP1 and IP5 is shown in blue. Figure adapted from [11].

The second proton beam (B2) needs to be guided around this interaction point in order for the two proton beams to perform proton-proton (p-p) collisions in the other three interaction points.

The 2021 LHeC conceptual design report [11] suggests different layouts for the ERL. Among other distinctions, they differ in their size and thus in the final energy that the electrons reach before the collision. In this report, the optimal ERL-to-LHC size ratio is taken to be one-fifth, as this value provides the best balance

between physics performance and cost efficiency [11]. The calculations in this PhD were performed assuming an ERL of this size. The developed source code can however be easily adapted to a different ERL design.

The ERL designed for LHeC consists of two linear accelerators, which are connected by a total of six arcs, see figure 14. After being injected at $0.5\,\mathrm{GeV}$ the electrons are accelerated in the two linacs over three turns to their final collision energy of $50\,\mathrm{GeV}$. Since their energy increases with each acceleration, different arcs are needed, to accommodate for the different momenta of the particles and the corresponding beam rigidity. After the third turn, the electron beam is steered into collision with B1. Most of the particles do not take part in this collision. After exiting through a detector aperture, they are steered back into the linacs. When the electron bunches reenter the linac, their phase advance is shifted by $\pi$ relative to the accelerating phase [47]. This can be achieved by adjusting the path length accordingly. This way, their energy can be fed back into the linac cavities while the electrons are decelerated. Consequently, it is easier to dump the beam and most of the energy used in the acceleration can be recovered ($94$-$96\%$ [12]).

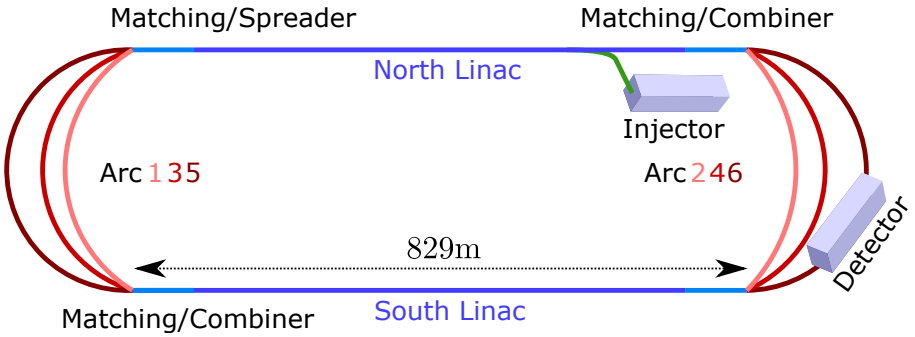


**Figure 14:** Schematic display of the energy recovery linac suggested for the LHeC. This design shows an ERL of one fifth of the size of LHC. The two linacs are connected over six arcs, which have different sizes to accommodate for the different beam rigidities after each acceleration.

The parameters that were chosen for the calculations and simulations for the ERL in this PhD are summarized in table 2.

Previous studies tested the compatibility of LHeC with the other HL-LHC experiments [48]. In these previous works, the LHeC interaction region was considered as a so-called **stand alone experiment**. This means that the interaction point IP2 would **only be used for e-p or electron-ion (e-a)** collisions, while still running in parallel to the remaining three p-p (or a-a) experiments in HL-LHC. The second proton beam would be kept separate from IP2 by sending it through this interaction region with a strong crossing angle and shifting IP2 by a quarter of the bunch spacing along the orbit. This way, the second proton beam would avoid

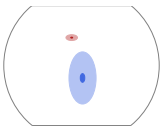

| Parameter | Value | Unit |
|---|---|---|
| Maximum Energy $E_e$ | 50 | GeV |
| Transverse Normalized Emittance $\varepsilon$ | 30 | µm |
| Frequency | 801.58 | MHz |
| Number of Particles $N_e$ | $3.1 \times 10^9$ | - |
| Electron Current $I_e$ | 20 | mA |
| Acceleration Gradient | 19.73 | MV/m |
| Bunch Charge | 499 | pC |
| Bunch Spacing | 24.95 | ns |
| Relativistic $\gamma$ | 97 847 | - |
| Total Length | 5332 | m |

**Table 2:** Key beam parameters for the LHeC energy recovery linac used in this thesis [11].

any interactions with the e-p collisions [48]. Consequently, p-p or a-a collisions would not be possible in IP2 anymore. This separation concept is illustrated in figure 15.

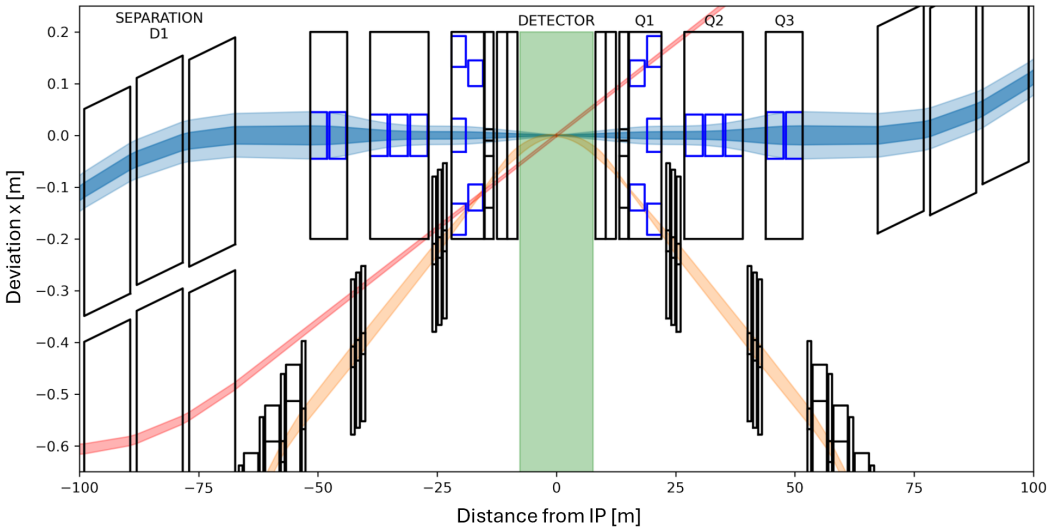


**Figure 15:** A possible beam separation scheme for a **stand alone** LHeC layout. The colliding proton beam B1 is shown in blue and the electron beam is represented in orange. The second proton beam B2, which needs to be separated from this collision, is shown in red. The triplet magnets of the final focusing system are named Q1, Q2 and Q3. B2 does not pass through the triplet magnets, as it does not take part in the e-p collision. The separation dipole, which is used to guide the proton beams back into their respective beam pipes, is named D1 [32]. Figure provided by K.D.J. André.

**In this PhD thesis an interaction region has been designed, which would allow two very different modes or operation: e-p or p-p**. To the author's knowledge, this is the first time this has been done.

This type of design would also demand a new kind of multipurpose detector. This detector needs to be capable to detect the asymmetric e-p collisions, as well as the high multiplicity a-a interactions studied in the ALICE experiment. Several detector designs have been investigated in the scope of the LHeC study. One of the more recent summaries of the detector concepts can be found in [49], as well as a more detailed overview in [23, 50].

## 3.2 Scheduled Upgrades for the Large Hadron Collider

Before going into detail about the interaction region designed in this PhD thesis, a short overview of the planned upgrades to the LHC complex will be presented. The information on these planned upgrades was extracted from [10, 51–54]. It is important to note that this timeline represents only a possible implementation of the LHeC, and all of the presented future schedules are still subject to change or have not yet been finalized.

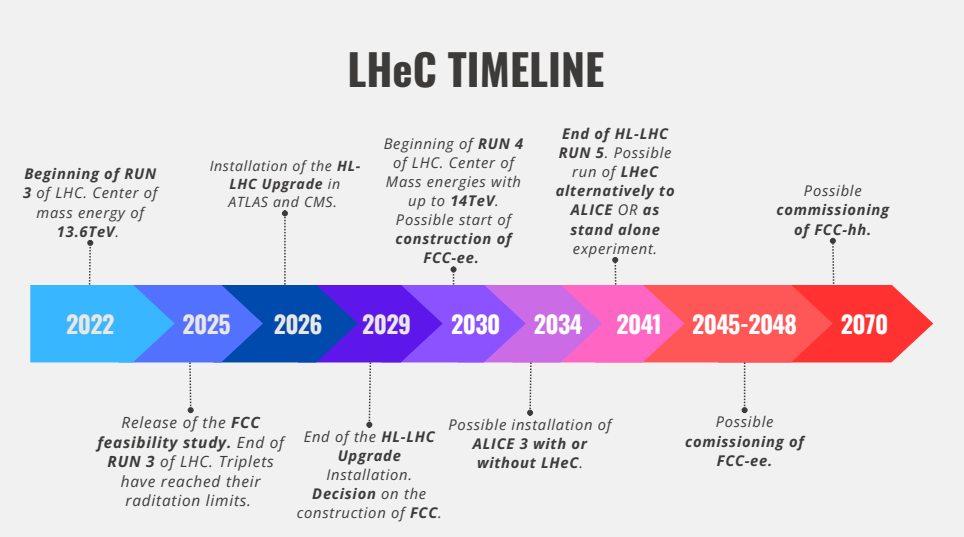


**Figure 16:** The scheduled timeline of the current proton run of LHC, together with the HL-LHC upgrade. The **possible** future scenarios for LHeC, as well as FCC-ee and FCC-hh are shown in the chart. The information used to create this timeline has been taken from [10, 51, 52], as well as [53].

Figure 16 shows the planned upgrades to the LHC infrastructure. Run 3 of the

LHC started in 2022 and will conclude in 2025, followed by the third long shutdown (LS3) from 2026 to 2029. During LS3, the HL-LHC upgrades will be installed in IP1 and IP5 for the two high-luminosity experiments, ATLAS and CMS. According to CERN's current planning, the decision on whether to construct the Future Circular Collider (FCC) will be taken in 2028 by the CERN Member States and funding partners, following the release of the FCC feasibility study in 2025 [55]. Run 4 is planned to start in 2030 and continue until 2033, after which LS4 will take place between 2033 and 2035. Run 5 of the HL-LHC is foreseen to operate until 2041.

Energy-recovery linac (ERL) technology is still under development. The PERLE (Powerful ERL for Experiments) test facility for the LHeC ERL in IJCLab in Paris is expected to demonstrate multi-turn operation by 2034 [56]. Depending on ERL readiness, the LHeC could be installed together with ALICE 3 during LS4 (2034–2035), or after the end of HL-LHC operation in 2041. It is assumed that the ERL itself could be constructed in parallel with HL-LHC operation. Because the timeline is tight for a three-turn ERL by 2034, a $20\,\mathrm{GeV}$ single-turn ERL design is currently under study [22].

The interaction region designed in this thesis is designed to work together with the other experiments in HL-LHC and in alternating mode to the planned upgrade for the ALICE 3 detector. It can be used for all suggested electron beam energies ($20\,\mathrm{GeV}$ to $60\,\mathrm{GeV}$).

FCC-ee construction could begin in 2030 and commissioning is anticipated to happen between 2045 and 2048. A later upgrade to hadron-hadron and hadron-electron operation is foreseen to start commissioning in 2070. During this FCC-ee construction period, LHeC could serve as a high luminosity stand alone experiment and act as a bridge project between the LHC and the future FCC program.

### 3.2.1 The High Luminosity Large Hadron Collider (HL-LHC) Upgrade

The scheduled upgrade for the LHC is meant to reach a peak luminosity of $7.5 \times 10^{34}\,\mathrm{cm^{-2}s^{-1}}$ [57]. This exceeds the nominal design luminosity of $1 \times 10^{34}\,\mathrm{cm^{-2}s^{-1}}$ [58] by a factor of $7.5$, and the current peak luminosity of $2 \times 10^{34}\,\mathrm{cm^{-2}s^{-1}}$ [59] by a factor of $3.75$. This increase in luminosity can be achieved with hardware changes in the two high luminosity experiments ATLAS and CMS, see figure 13. The final focusing system in these interaction points currently consist of triplets (three quadrupoles) built out of Niobium Titanium (NbTi) technology. By the end of 2025 this triplet is assumed to have reached its radiation limit. During the following shutdown it will be replaced by a Niobium Tin triplet

($Nb_3Sn$). The major advantage of this material is that it offers a much larger aperture to the beams in the triplet. This allows for a stronger focusing of the beam in the interaction point. Table 3 summarizes the parameters of the triplet magnets.

| Parameter | Unit | LHC Q1/Q2/Q3 | HL-LHC Q1/Q2/Q3 |
|---|---|---|---|
| Conductor material | | NbTi | $Nb_3Sn$ |
| Magnetic field gradient | T/m | 205 | 132.6 |
| Magnetic length | m | 6.37/5.5/6.37 | 4.20/7.15/4.20 |
| Aperture radius | mm | 70 | 150 |

**Table 3:** A summary of the magnet values of the triplets of the two interaction points that will be upgraded in the long shutdown 3 (LS3) between 2026 and 2029. The NbTi triplets of IP1 and IP5 will be replaced with triplets made of $Nb_3Sn$. Q1, Q2 and Q3 represent the quadrupoles of the triplets seen in figure 17. These values have been extracted from [57, 60] and [58, 61].

The larger aperture is necessary not only to focus the beams before their collision, but also to distance the two proton beams far enough to minimize their beam-beam effects on each other. During the HL upgrade, the bunch population is increased from $1.15 \times 10^{11}$ protons/bunch to $2.2 \times 10^{11}$ protons/bunch [58, 62], which increases the beam-beam effects. The corrector magnets in these interaction regions, as well as the dipoles D1 and D2 used to steer the two proton beams into their corresponding beam pipes will also be replaced with magnets that offer a larger aperture. These dipoles are used to bend the proton beams into a common beam pipe before the collision, and to send them back into their own beam pipe after the collision. The warm separation/recombination dipole D1 will be replaced by a superconducting one, offering a higher field quality [63, 64]. Replacing it with a superconducting one decreases its length massively and adds space in these interaction regions. The newly installed triplet, as well as the replacement of the separation dipole can be seen in figure 17.

Another strategy to increase the luminosity in these interaction regions is to install *crab cavities* in the newly created space between the D2 magnet and the matching quadrupole Q4. The two proton beams in the HL-LHC collide at an angle to minimize their beam beam effects on each other. This can be seen in section 3.3. This angle reduces the overlap of the bunches during collision. Crab cavities apply a kick to the beam bunches which rotates them before their collision, maximizing the overlap of the bunches. More information can be found here [65].

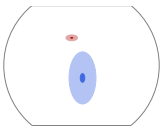

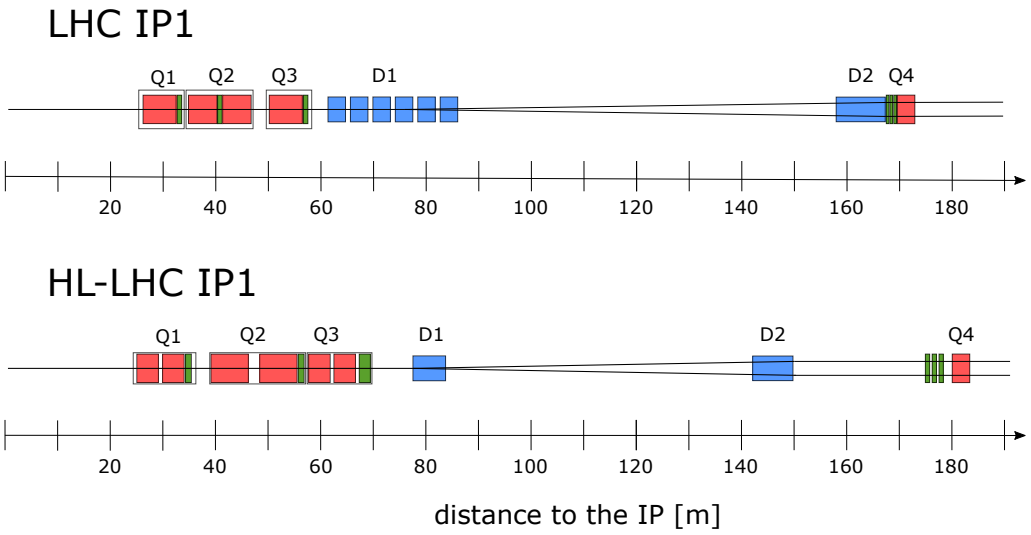


**Figure 17:** A schematic representation of the main changes concerning the triplet in the HL-LHC upgrade in IP 1/5. On the top, the current interaction region is shown and below the upgraded one. The main changes include a replacement of the current triplet magnets Q1, Q2, Q3 and the replacement of the warm separation/recombination dipole D1 by a superconducting one, as well as the replacement of the current superconducting separation/recombination dipole D2 with a magnet that offers more aperture. Additionally, the second separation/recombination dipole D2 is moved closer to the triplet. The correctors embedded in the triplet are also exchanged by correctors which offer more aperture. The space created between the D2 dipole and the Q4 quadrupole will be used to install crab cavities.

### 3.3 The Mutlipurpose Interaction Region

The interaction region designed in this thesis allows two modes of operation. The first one being the current mode of operation of the LHC, hosting either p-p or ion-ion collisions in the four interaction points of the LHC. The second mode of operation enables e-p operation in IP2, concurrently to p-p operation in the other interaction points: namely in IP1 (ATLAS), IP5 (CMS) and IP8 (LHCb). The two proton beams are accelerated in LHC, while the electron beam is accelerated in the ERL and then brought into collision with the clockwise rotating proton beam B1. Each proton beam circulates in its own beam pipe, except in the four interaction points, where they are diverted into a common beam pipe. During LHeC operation, the second proton beam (B2), is guided around the e-p collision in the same beam pipe as B1 so that it can collide with B1 in IP1, IP5 and IP8.
A concept for the LHeC interaction region has been developed in this thesis, which separates B2 from B1, while B1 collides with the electron beam. This includes changes to the orbit as well as to the optics of the proton beams.

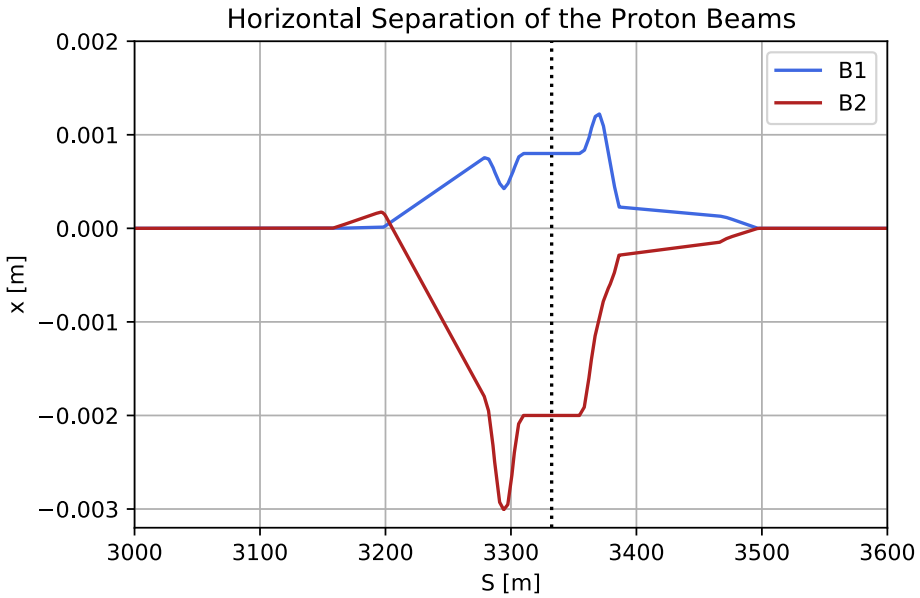


**Figure 18:** Separation scheme for the two proton beams in the horizontal plane. The colliding proton beam B1 is represented in blue, while the spectating proton beam B2 is represented in red. The dashed line marks the position of interaction point 2.

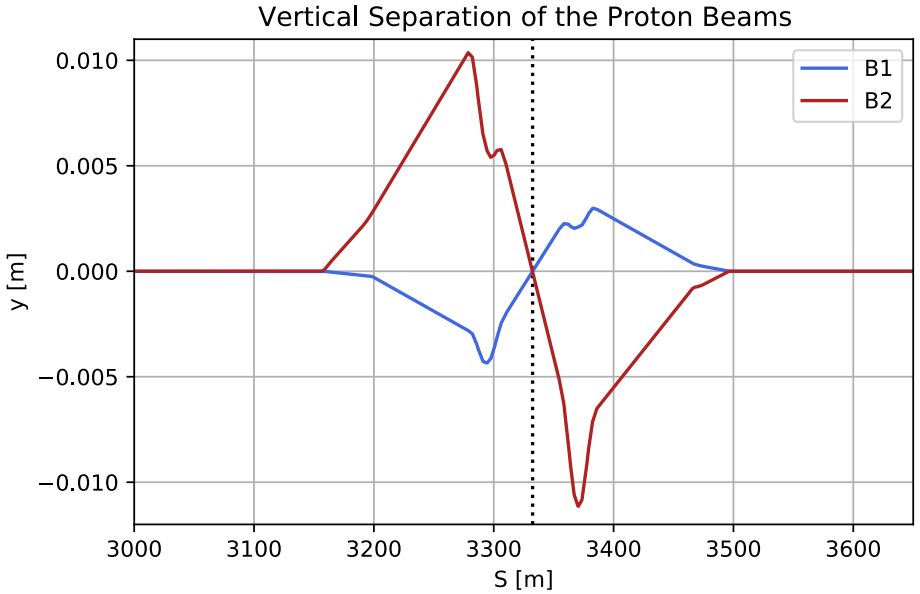


**Figure 19:** Separation scheme for the two proton beams in the vertical plane. The proton beam B1, which participates in the e-p collisions is represented in blue, while the second proton beam B2 is represented in red. The dashed line marks the position of interaction point 2.

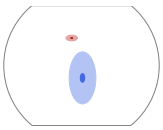

The two proton beams are first separated by adjusting their orbits. As a result, the trajectories of the two proton beams in their shared beam pipe differ. In the horizontal plane, the two proton beams are separated using separation bumps. These consist of a combination of dipoles and are normally used to separate the beams during injection and during the energy ramp in their common beam pipe in the interaction regions. In the vertical plane, crossing angles are applied to the two proton beams to separate them further from each other. This concept can be seen in figure 18 and figure 19. The vertical crossing bumps are used during the collisions in LHC to minimize beam-beam effects between the two proton beams before and after their collision.

The optics of B1 are designed to focus the beam as much as possible and in turn achieve the highest luminosity. Due to *Liouville's theorem*, this causes a large expansion in the beam size, upstream and downstream of the collision. In order to keep a safety margin to the beam pipe, the magnitude of the orbit bumps for B1 is significantly smaller than for B2.

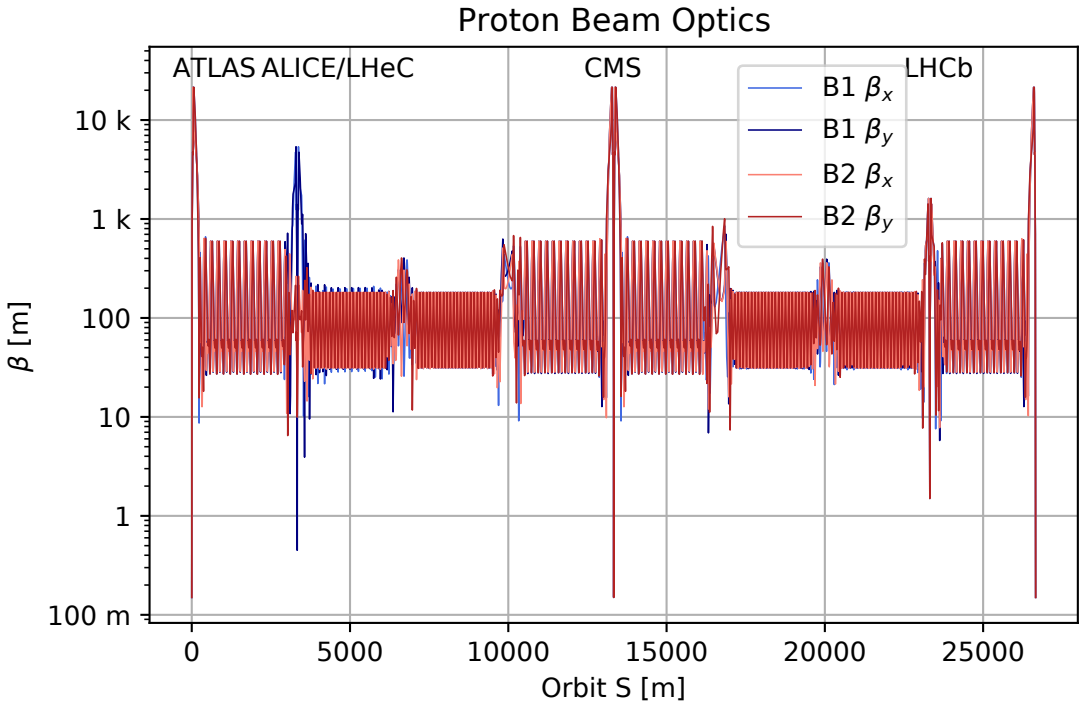


**Figure 20:** Optics of the two proton beams along the HL-LHC (semi-logarithmic scale). Both beams are focused in the high luminosity experiments ATLAS and CMS, as well as in the LHCb experiment. In IP2, only B1 (blue) goes into collision with the electron beam, while B2 (red) is guided around this collision. B2 is only weakly focused in this point.

The optics of B2 on the other hand, needs to minimize the potential beam blow up. This can be achieved by keeping the beam only weakly focused at the IP, effectively making it more ”relaxed”. The advantage of this approach is that B2 remains more compact in the region where B1 expands. A plot of the optics for both proton beams across all of HL-LHC can be seen in figure 20. Figure 21 shows a zoom-in of the LHeC interaction region.

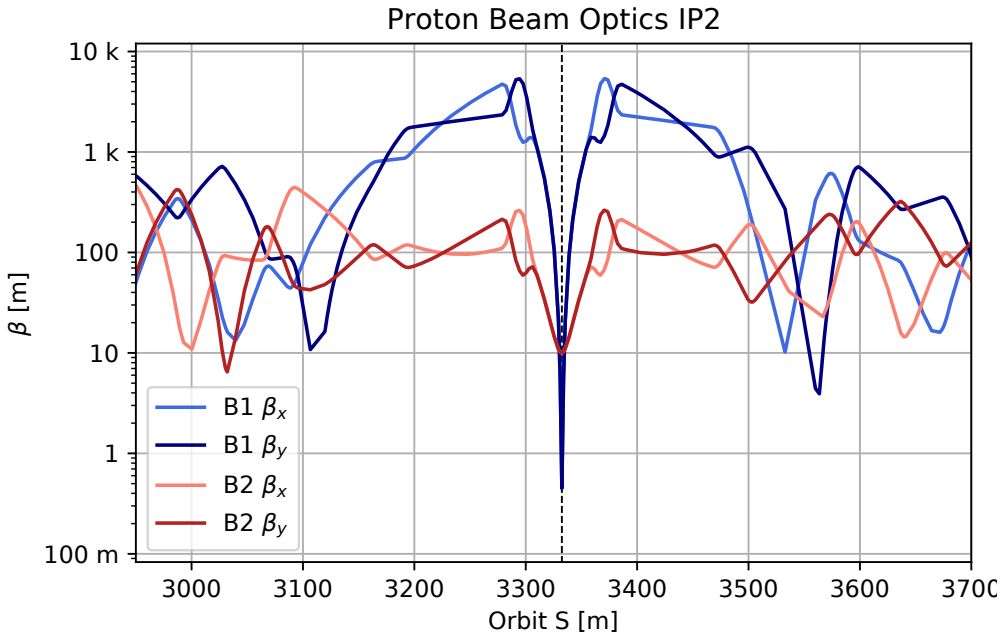


**Figure 21:** Zoom-in of the optics of the proton beam optics at IP2 during LHeC operation. The proton beam which collides with the electrons is represented in blue, while the second proton beam, which does not collide in this IP, is displayed in blue. For clarity, the optics are displayed on a semi-logarithmic scale.

This separation concept is displayed in its entirety in three dimensions in figure 22.

The following chapters explain the steps to optimize the distance between the two proton beams while pushing for a high e-p luminosity.

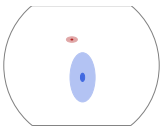

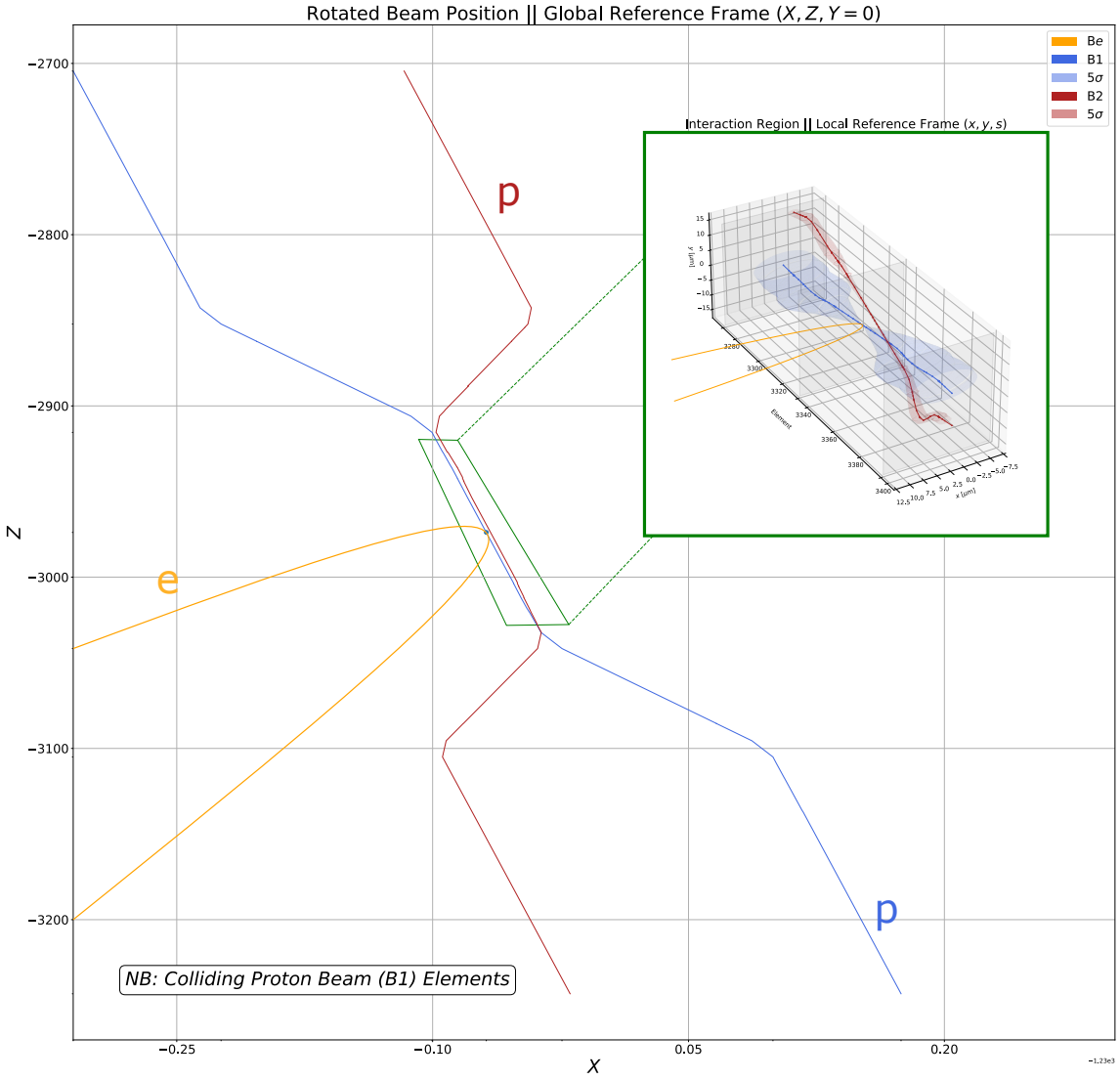


**Figure 22:** Display of the separation concept developed in this thesis to enable e-p collisions in this interaction region, while the second proton beam bypasses the collision. It shows the electron beam in orange, the colliding proton beam in blue, and the bypassing proton beam in red. The bigger picture shows how the two proton beams move from their corresponding beam pipes into the shared interaction region. A zoom-in of the interaction point is shown, which displays a 3D representation of the three beams. In this zoom, the different optics of the beams can be seen, as $5\,\sigma$ of the beam envelopes are plotted. This plot was developed with significant contributions of Matthew Smith, as part of his internship at CERN in 2022 [66].

# 4 Installation of the Electron Insertion

This chapter covers the installation of additional magnets into the LHC lattice, which guide and focus the electron beam and examines their impact on the proton beams.

In order to realize e-p collisions in interaction point 2 of LHC, additional magnets need to be installed in this region. This electron interaction region has been designed by Kévin Daniel Joel André in his PhD Thesis [32], in a way that minimizes the electron synchrotron radiation [1]. It consists of a quadrupole doublet, and two bending dipoles. The dipoles are used to guide the electron beam from the ERL into the e-p collision and then back into the ERL. The doublet focuses the electron beam before the collision to the same size as the proton beam. The electron insertion is schematically displayed in figure 23, together with the final focusing system of the protons. It also shows the electron beam, as well as the two proton beams.

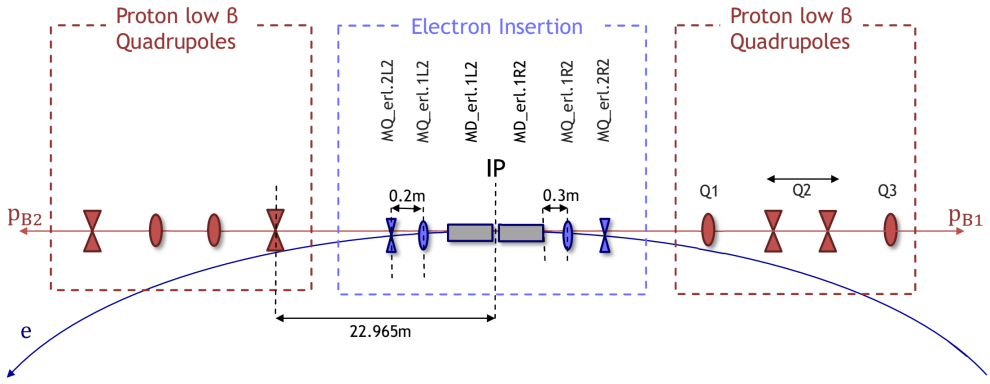


**Figure 23:** Schematic display of the final focusing system of the protons (red), as well as the final focusing system of the electrons (blue) and their bending magnets (grey). The spherical shapes indicate quadrupoles that focus in the horizontal plane, while the hourglass shapes represent quadrupoles that focus in the vertical plane. The electron beam is schematically represented in blue, while the proton beams are represented in red. The names of the newly inserted magnets are marked on the top.

The bending dipoles are placed to the left and to the right of the interaction point. On the left side, the beams pass through a horizontally defocusing quadrupole

[1] Charged particles emit synchrotron radiation when their trajectories are bent. The radiated power $P_\gamma$ scales as $P_\gamma \propto \frac{\gamma^4}{\rho^2}$ with the Lorentz factor $\gamma = \frac{E}{mc^2}$. Because of the strong $\gamma^4$ dependence and the small mass of the electron, electrons lose significant amounts of energy on strongly bent trajectories with radii $\rho$ [30].

and a horizontally focusing quadrupole. On the right side of the interaction point, this doublet is mirrored. The quadrupole magnets of the doublet are slightly misaligned in reference to the electron beam orbit, as well as to the proton beam orbit. This creates a feed down effect, which is exploited here to additionally bend the electron beam's trajectory. In between the dipole and the focusing quadrupole there is a $30\,\mathrm{cm}$ drift space, and there is a $20\,\mathrm{cm}$ drift space between the two quadrupoles.

The electron beam is bent away before reaching the first proton quadrupole $22.965\,\mathrm{m}$ after the IP. The electrons therefore do not pass through any part of the focusing system of the protons. However, the two proton beams do pass through the electron insertion. The protons have a collision energy of $7000\,\mathrm{GeV}$, compared to the $50\,\mathrm{GeV}$ of the electron beam. Hence, the impact of the electron insertion on the proton beam needs to be scaled with a factor of $50/7000 \approx 0.0072$. This factor has been taken into account when implementing the electron insertion for the protons in MAD-X.

When the electron insertion is integrated into the proton HL-LHC lattice to study its impact on the protons, the positions of the magnets are determined based on their lengths. This way, when different values and lengths are assigned to the elements, they can be loaded and installed without additional modifications to the source code. The position $p_f$ of the focusing quadrupoles on the left and on the right side of the IP, can be calculated as such:

$$p_f = l_{\mathrm{dipole}} + 0.3\,\mathrm{m}. \tag{37}$$

Here $l_{\mathrm{dipole}}$ corresponds to the length of the dipole. The $30\,\mathrm{cm}$ corresponds to the drift space between the dipole and the focusing quadrupole. The distance for the defocusing quadrupole $p_d$ is calculated using:

$$p_d = l_{\mathrm{dipole}} + 0.3\,\mathrm{m} + l_{\mathrm{quad}} + 0.2\,\mathrm{m}. \tag{38}$$

With $l_{\mathrm{quad}}$ being the length of the quadrupoles and the $20\,\mathrm{cm}$ corresponding to the drift space between the focusing and the defocusing quadrupoles.

A detailed overview of the MAD-X files used for installing the electron insertion, as well as the magnet settings applied to the HL-LHC lattice, can be found in appendix A.1.

## 4.1 Calculation of the Misalignment of the Quadrupole Doublet in Reference to the Proton Orbit

The electrons are bent into, as well as out of the collision with the use of the two dipole magnets. By misaligning the quadrupoles slightly in reference to the electron orbit, the feed down effect can be used to create an additional dipole component to bend the electron beam's trajectory. This offset $\Delta x_{\text{quad}}$ of the quadrupole magnets is taken into account by applying a misalignment to them in the installation file. When installing these additional magnets into the proton lattice, the misalignment in reference to the proton orbit needs to be recalculated. This is because the electron and the proton orbits differ slightly.

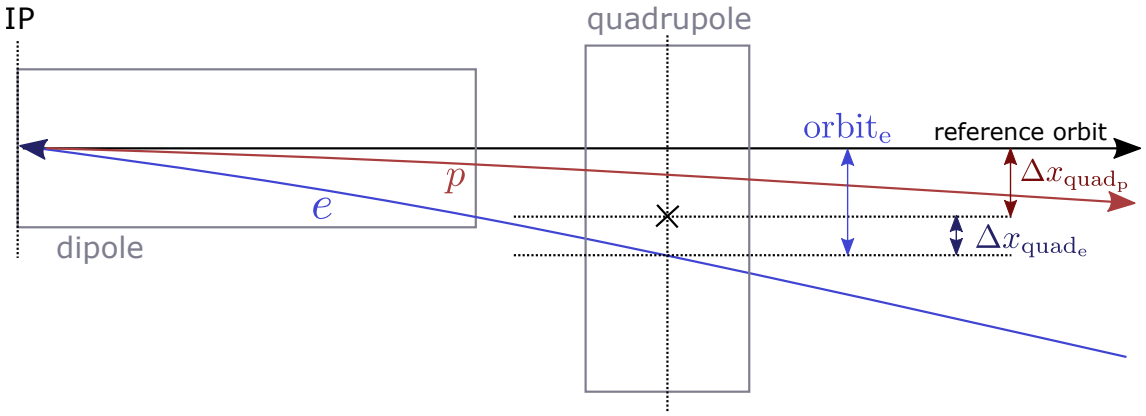


**Figure 24:** Schematic view of the colliding proton beam (red) and electron beam (blue) before their interaction. The proton beam is bent away from its reference orbit by the dipole magnet. The distance of the electron beam to the reference proton orbit is denoted as $\text{orbit}_\text{e}$ and the misalignment of the quadrupole in reference to the electron orbit is referred to as $\Delta x_{\text{quad}_e}$. The misalignment of the quadrupole in reference to the reference proton orbit is called $\Delta x_{\text{quad}_p}$.

All of the misalignments of the four quadrupoles in the electron insertion need to be readjusted for the protons. The calculation is demonstrated here for the first quadrupole on the right side of the interaction point: MQ_erl.1R2 in figure 23. This calculation is then repeated analogously for the other three quadrupole magnets at their corresponding positions. The misalignment of the quadrupole compared to the distorted proton orbit is referred to as $\Delta x_{\text{quad}_\text{p}}$. A schematic view of the misalignment of the first quadrupole in reference to the electron orbit and the distorted proton orbit, as well as the reference proton orbit is shown in figure 24.

This displacement $\Delta x_{\text{quad}_p}$ can be determined by first calculating the trajectory of the electrons $\text{orbit}_\text{e}$ in this magnet and subtracting the misalignment of this magnet in reference to the electron orbit $\Delta x_{\text{quad}_e}$:

$$\Delta x_{\mathrm{quad}_p} = \mathrm{orbit_e} - \Delta x_{\mathrm{quad}_e}. \tag{39}$$

Figure 25 indicates different positions $s_i$ marked in the lattice.

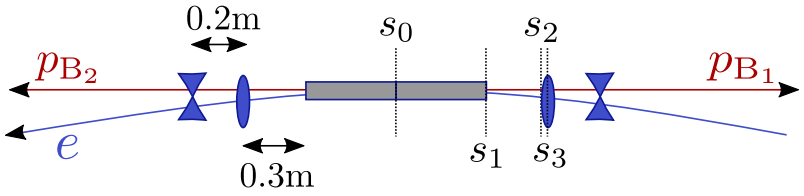


**Figure 25:** Schematic display of the two proton beams (red), as well as the electron beam (blue), as they pass through the electron magnet insertion. Different positions along the orbit $s$ in the lattice are marked.

To calculate $\Delta x_{\mathrm{quad_p}}$, the electron orbit must first be determined. This requires calculating both the divergence $x'$, which corresponds to the angle of the trajectory for small angles $\vartheta$, and the transverse displacement $x$ at position $s_3$ shown in figure 25. These calculations are symmetric for the magnets on the left and right sides of the interaction point.

In the following, the trajectories of the particles through a drift space, as well as through a dipole and a quadrupole are defined. These equations, if not otherwise specified, can be found in [30].

When passing through a **drift space**, the displacement $x$ at the position $s$ can be calculated using:

$$x(s) = x_0 + \vartheta_0 \cdot s \tag{40}$$

and the angle $\vartheta(s)$ at the position $s$ can be calculated using:

$$\vartheta(s) = \vartheta_0. \tag{41}$$

In these equations, $x_0$ and $\vartheta_0$ denote the initial particle displacement. When the particles pass through a **dipole**, their displacement $x$ at a position $s$ can be calculated using:

$$x(s) = x_0 + \vartheta_0 \cdot s + \frac{1}{\rho} . \frac{s^2}{2}. \tag{42}$$

In this equation, $\rho$ represents the bending radius of the dipole. The angle $\vartheta_{\text{bend}}$ of a **dipole** can be calculated with:

$$\vartheta_{\text{bend}} = \int_0^s \frac{B}{B\rho} \text{ds}' \approx \frac{B}{B\rho} s. \tag{43}$$

In this equation $B$ represents the magnetic field strength of the dipole. This equation can be found in [67]. Inserting it into equation 42, the transversal trajectory of a particle through the **dipole** at a position $s$ can be calculated using:

$$x(s) = x_0 + \vartheta_0 s + \frac{\vartheta_{\text{bend}} \cdot s}{2}. \tag{44}$$

With equation 43 the angle $\vartheta(s)$ at a position $s$ in a **dipole** can be calculated using:

$$\vartheta(s) = \vartheta_0 + \vartheta_{\text{bend}}. \tag{45}$$

As the particles pass through a **quadrupole**, their displacement $x(s)$ at a position $s$ can be calculated using:

$$x(s) = x_0 + \vartheta_0 s + \frac{G}{B \cdot \rho} \cdot (x_0 - \Delta x_{\text{quad}}) \cdot \frac{s^2}{2}. \tag{46}$$

Here, $G$ corresponds to the magnetic field gradient of the quadrupole and $\Delta x_{\text{quad}}$ represents the misalignment of the quadrupole with reference to the orbit. The factor $\frac{G}{B \cdot \rho}$ is called normalized quadrupole strength $k$, as it is normalized by the beam rigidity.

The angle $\vartheta(s)$ at a position $s$ after the propagation through a **quadrupole** can be calculated using:

$$\vartheta(s) = \vartheta_0 + \frac{G}{B \cdot \rho} \cdot (\vartheta_0 - \Delta x_{\text{quad}}) \cdot s. \tag{47}$$

In the following, the **orbit of the electrons** at position $s_3$ in figure 25 is calculated, so that the misalignment of the proton quadrupole $\Delta x_{\text{quad}_\text{p}}$ can be calculated. This is an iterative process and as a result, the orbit needs to be calculated for every previous position. At the position of the interaction point $s_0$ the angle $\vartheta_0$ and the position $x_0$ correspond to $0$:

$$\vartheta(s_0) = 0 \tag{48}$$

$$x(s_0) = 0. \tag{49}$$

Between $s_0$ and $s_1$ the particles pass through a dipole. At $s_1$ the orbit $x(s_1)$ for the electrons can be calculated using equation 44:

$$x(s_1) = x(s_0) + \vartheta(s_0) \cdot l_{\text{bend}} + \frac{\vartheta_{\text{bend}} \cdot l_{\text{bend}}}{2} = \frac{\vartheta_{\text{bend}} \cdot l_{\text{bend}}}{2}. \tag{50}$$

With $l_{\text{bend}}$ and $\vartheta_{\text{bend}}$ representing the length and the deflection angle of the dipole magnet. The angle $\vartheta(s_1)$ at $s_1$ for the electrons can be calculated using equation 45:

$$\vartheta(s_1) = \vartheta(s_0) + \vartheta_{\text{bend}} = \vartheta_{\text{bend}}. \tag{51}$$

.

At the position $s_2$ the electron beam has propagated through a drift space of $30\,\text{cm}$. Therefore the position $x(s_2)$ of the electrons is calculated using equation 40:

$$x(s_2) = x(s_1) + \vartheta(s_1) \cdot 0.3\,\text{m} \tag{52}$$

and the angle of the beam at position $s_2$ is calculated using equation 41:

$$\vartheta(s_2) = \vartheta(s_1) = \vartheta_{\text{bend}}. \tag{53}$$

Position $s_3$ marks the center of the focusing quadrupole. The distance that the particles travel within the quadrupole up to this point is therefore $\frac{l_{\text{quad}}}{2}$, where

$l_{\text{quad}}$ corresponds to to the total length of the quadrupole. The orbit $x(s_3)$ at position $s_3$ can then be calculated using formula 46:

$$x(s_3) = x(s_2) + \vartheta(s_2) \cdot \frac{l_{\text{quad}}}{2} + kf_e \cdot (\Delta \text{x}_{\text{quad}_e}) \cdot \frac{\left(\frac{l_{\text{quad}}}{2}\right)^2}{2}. \tag{54}$$

Here, $\Delta x_{\text{quad}_e}$ corresponds to the distance of the magnetic center to the electron beam, shown in figure 24 and $kf_e$ represents the quadrupole strength, scaled for the electrons.

The angle of the beam at position $s_3$ is calculated using formula 47:

$$\vartheta(s_3) = \vartheta(s_2) + kf_e \cdot (\Delta x_{\text{quad}_e}) \cdot \frac{l_{\text{quad}}}{2}. \tag{55}$$

The electron orbit at the position of the second focusing quadrupole MQ_erl.2R2 (see figure 23) can then be calculated analogously. The **orbit of the protons** is obtained using the same procedure. However, in this case, the strengths of the quadrupoles, as well as the dipoles, need to be scaled for the energy of the protons. Finally, the misalignment of the quadrupole $\Delta x_{\text{quad}_\text{p}}$ can be computed using formula 39. These values are computed in the installation file of the electron insertion. This way, different strengths or misalignments for the electron magnets can be loaded and the corresponding values are automatically calculated for the protons, as the new elements are inserted into the proton lattice.

## 4.2 Impact of the Electron Insertion on the Proton Beams

The two proton beams pass through the electron insertion. Considering a proton collision energy of $7000\,\text{GeV}$ and an electron collision energy of $50\,\text{GeV}$, the impact of this insertion on the protons is small. It is however not negligible and needs to be corrected. The extent of this impact, as well as its compensation is explained in the following. It is shown for proton B1, the clockwise rotating proton beam. Since the proton beams are symmetric, the impact on the counter clockwise rotating proton B2 is of the same order of magnitude. The correction of the orbit and optics is performed in the same manner.

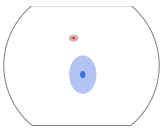

### 4.2.1 Impact of the Electron Insertion on the Orbit of the Proton Beams

The two installed dipole magnets modify the orbit of the proton beam. The quadrupoles are misaligned in the x-plane in reference to the orbit, and thus they also slightly impact it. Since the dipoles act only in the horizontal plane and the quadrupole misalignments are also purely horizontal, only the horizontal orbit is distorted.

The distorted orbit at a position $s$ for a dipole deflection can be calculated using:

$$x(s) = \frac{\vartheta}{2\sin(\pi Q)}\sqrt{\beta(s)\beta(s_0)}\cos(|\psi(s) - \psi(s_0)| - \pi Q). \tag{56}$$

Here $s_0$ marks the position of the dipole, $\vartheta$ describes the deflection angle applied at $s_0$, and $\psi(s)$ describes the phase advance at the position $s$, while $\psi(s_0)$ describes the phase advance at the location of the dipole. $\beta(s)$ represents the beta function at the measured position and $\beta(s_0)$ the beta function at the position of the dipole. This equation can be found in [68].

Before installing all of the elements of the electron insertion into the HL-LHC lattice, only one dipole is installed to verify its impact on the proton orbit. The dipole on the right side of the interaction point, namely MD_erl.1r2 (see figure 23), is installed into the proton lattice. Using equation 56, the orbit distortion is calculated between the interaction point and the position of the dipole. For B1, this manually calculated value amounts to $0.242\,\mathrm{mm}$. This scenario is subsequently modeled in MAD-X. The extracted value for the orbit distortion at the position of the dipole equals to $0.228\,\mathrm{mm}$. The two results agree well, with the MAD-X value expected to be more precise. It is therefore assumed, that the modeled dipole is well defined and the remaining elements of the electron insertion are installed into the proton lattice.

In figure 26 the impact of the elements of the electron insertion on the proton orbit in the x-plane can be seen. It shows, that the orbit distortion is stronger at points with higher beta functions, for example at ATLAS and CMS, as can be derived from formula 56.

The orbit distortion is subsequently corrected in MAD-X. This correction is performed by using a set of orbit correctors. These orbit correctors are small dipoles, which bend the proton orbits locally. By using a combination of dipoles, these correctors are usually used to create orbit bumps. In LHC, the corrector closest to the interaction point is called corrector 1. Moving further away from the IP, the correctors are subsequently numbered. Correctors 1, 2 and 3 act on both beams.

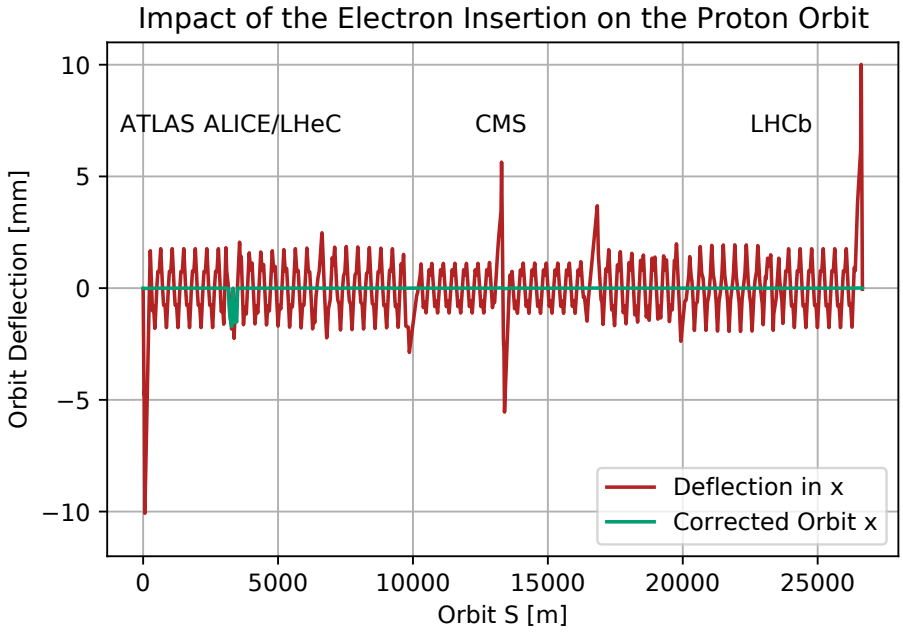


**Figure 26:** Orbit deflections in the x-plane for B1 after installation of the electron insertion. The dipoles and misaligned quadrupoles deflect the beam in the horizontal plane. The four interaction points are marked with their corresponding experiments. The applied correction on the horizontal orbit is shown in green.

For correctors number 4 and above, each beam has its own dedicated set. In this orbit correction, the correctors numbered 4 and 5 on the left and the right side of the interaction point are used.

The orbit is rematched at three positions. First, upstream of the interaction point, at the end of the dispersion suppressor (DS), referred to as E.DS.L2.B1. Then, at the IP; and finally downstream of the IP at the start of the dispersion suppressor, referred to as S.DS.R2.B1. It is favorable to rematch at these particular points, as they are located before the beams reenter into the arcs and thus a local correction only affecting IR2 can be performed. At each of these three positions the horizontal position $x$ and the divergence $x'$ are matched back to $0$. In figure 26 this orbit correction is shown in green.

A zoom-in of the interaction region, where the orbit is corrected, can be seen in figure 27.

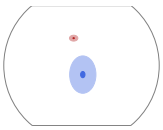

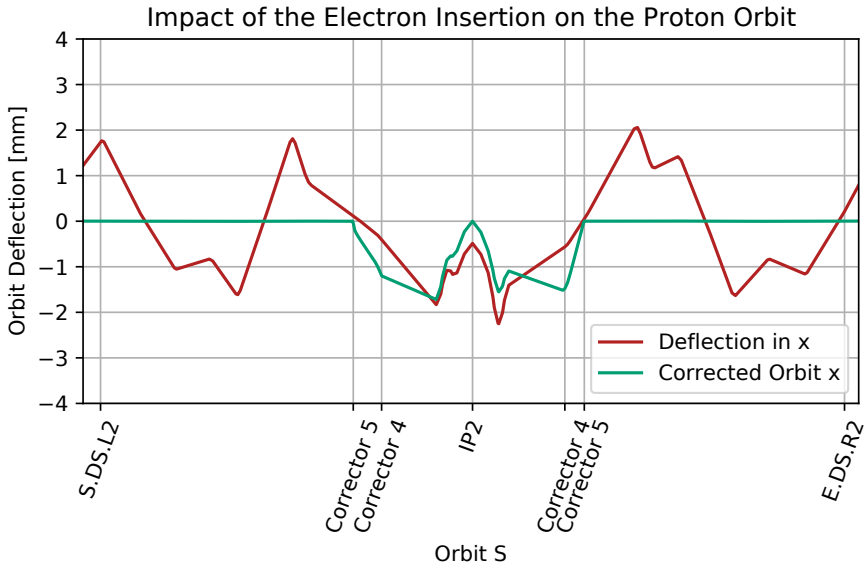


**Figure 27:** Zoom-in of the area in which the orbit is corrected. The three positions at which the orbit is rematched are the dispersion suppressors of the lattice before the beams reenter into the periodic arcs, as well as the interaction point: S.DS.L2, IP2, and E.DS.R2. The positions of the used orbit correctors are marked.

After correcting the orbit for the proton beams, the impact of the electron magnets on the proton optics is investigated.

### 4.2.2 Impact of the Electron Insertion on the Optics of the Proton Beams

The inserted quadrupoles affect the proton optics by slightly modifying the amplitude function and thereby introducing a tune shift. In the proton beam optics, the quadrupoles of the electron insertion are treated as quadrupole field errors. The change of the beta function $\Delta\beta$ at a position $s$ due to a quadrupole placed at $s_0$ can be calculated using:

$$\Delta\beta(s) = -\frac{\beta(s)\beta(s_0)}{2\sin(2\pi Q)} \cdot \Delta k \cdot L \cdot \cos(2|\psi(s) - \psi(s_0)| - 2\pi Q). \tag{57}$$

In this equation, which can be found in [68], $\Delta k$ describes the quadrupole strength error and $L$ represents the length of the quadrupole. $Q$ represents the tune and $\psi(s)$ and $\psi(s_0)$ the phase advances at the corresponding positions.

In figure 28 the beta-beat is plotted against the position $s$ along the orbit of the protons. This beta-beat is calculated as the difference of the original beta function $\beta_0(s)$ and the new beta function value $\beta(s)$ at a position $s$ and by normalizing it over the original beta function:

$$\frac{\Delta\beta(s)}{\beta(s)}[\%] = \frac{\beta_0(s) - \beta(s)}{\beta_0(s)} \cdot 100. \tag{58}$$

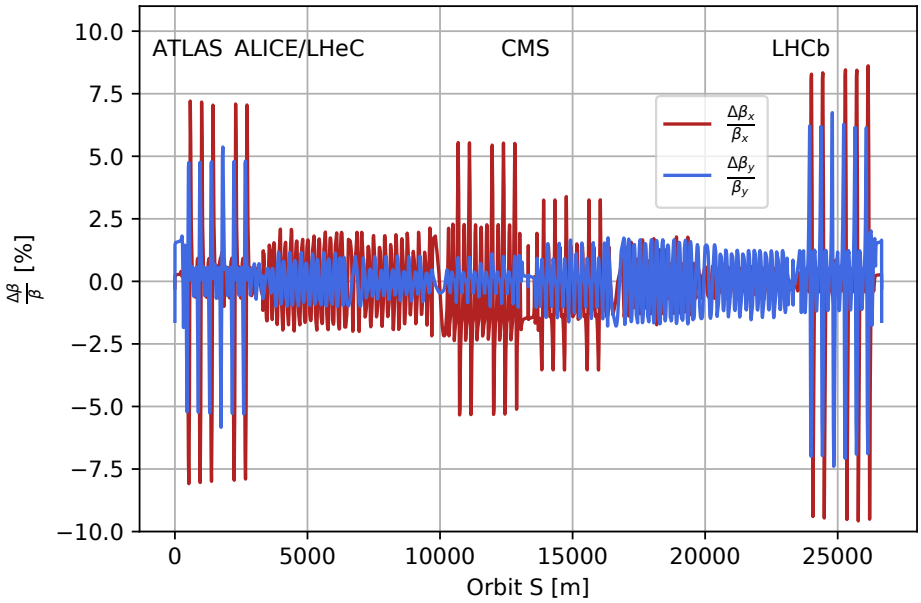


**Figure 28:** Relative change in the beta function of proton B1 in the x- (red) and the y- (blue) plane after insertion of the electron elements into the HL-LHC proton lattice.

Using equation 57 the change in the horizontal beta function at the first quadrupole can be calculated manually to be $-0.3265\,\mathrm{m}$. The value calculated by MAD-X is $-0.2534\,\mathrm{m}$. The slight difference in the values can be explained by MAD-X taking into account the misalignment of the magnet.

The impact on the optics is subsequently corrected by using the matching quadrupoles of interaction region 2 in the LHC. Every interaction region in LHC has its own set of matching quadrupoles in order to well define the beam at the interaction point. The matching quadrupoles are positioned upstream of the point where the beams enter into the common beam pipe. The optics are corrected at

two positions. Once at the interaction point IP2 and once at the end of the dispersion suppressor on the right side of IP2: E.DS.R2.B1. In order to correct the optics, 8 parameters need to be rematched. They are summarised in table 4.

| Position | Matching Parameters |
|---|---|
| IP2 | $\beta_x, \beta_y, \alpha_x, \alpha_y, D_x, D'_x, \mu_x, \mu_y$ |
| E.DS.R2.B1 | $\beta_x, \beta_y, \alpha_x, \alpha_y, D_x, D'_x, \mu_x, \mu_y$ |

**Table 4:** Parameters that need to be rematched to correct the impact of the electron insertion on the proton optics. These parameters include the beta function $\beta_{x/y}$, as well as the correlation function $\alpha_{x/y}$ in both transversal planes, the dispersion in $x$ called $D_x$, the gradient of the dispersion $D'_x$ and finally, the phase advances in both planes $\mu_{x/y}$. They were rematched at two positions.

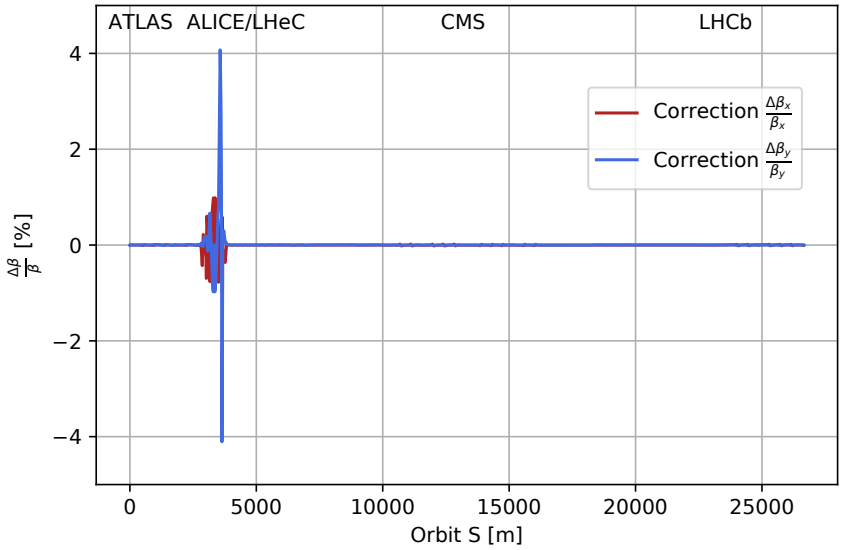


**Figure 29:** Corrected beta-beat across the whole length of LHC for both planes for proton B1. After the correction, only a slight disturbance can be seen at the ALICE/LHeC experiments.

These parameters are matched by using the matching quadrupoles of this interaction region, as well as some of the trim quadrupoles. A detailed summary of the used magnets can be found in appendix A.1.1. The results of the beta-beats of the rematched optics in both transversal planes are shown in figure 29.

A zoom-in of the interaction region is shown in figure 30. This is the area where the correction is performed. A slight deviation can be seen in the region just

before and after the IP, where the electron magnets have been inserted and the correction of the matching quadrupoles is performed.

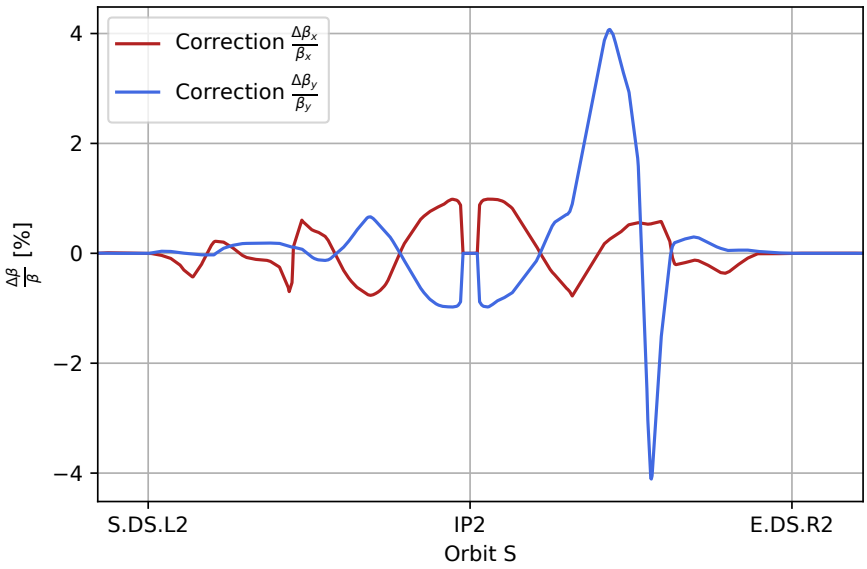


**Figure 30:** Zoom into the region in which the proton optics is corrected. The optics is corrected at the IP, as well as on the right side at the start of the dispersion suppressor (S.DS.L2) and downstream of the IP at the end of the dispersion suppressor (E.DS.R2.).

In addition to causing a distortion of the beta function, a quadrupole error also induces a change in the machine tune. This tune shift $\Delta Q$ is calculated using [30]:

$$\Delta Q \approx \frac{\beta(s_0) \cdot \Delta k \cdot l_{\text{quad}}}{4\pi}. \tag{59}$$

Here $\beta(s_0)$ represents the beta function at the position $s_0$ of the quadrupole error $\Delta k$ with a quadrupole of length $l_{\text{quad}}$.

Before installing all of the electron insertion, only one of the quadrupoles was installed and the corresponding tune shift was quantified. When inserting the quadrupole MQ_erl.1r2 (see figure 23) into the HL-LHC lattice of the protons (see figure 23), a tune shift of $0.0051$ in the horizontal plane was observed in the MAD-X output. Using equation 59, the tune shift can be calculated approximately. The manually calculated value is $0.0054$. The approximation aligns well with the MAD-X output. It was therefore assumed that this quadrupole is well defined.

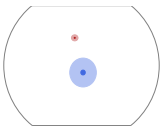

The horizontal and the vertical tune shifts are corrected in the local optics correction. As shown in table 4, the horizontal, as well as the vertical phase advance, are corrected locally. As a result, the global tune is corrected.

This chapter demonstrates that the impact of the electron insertion on the proton orbit and optics is small but not negligible. Its effects can be corrected locally requiring only minor adjustments in interaction region 2 of the HL-LHC lattice.

# 5 Flexible Proton Optics for LHeC

This chapter explains the process of creating the optics for the two proton beams. The designed optics aims to maximize the separation between the two proton beams at the e-p collision point, while achieving the highest possible e-p luminosity in this three-beam layout. Two interaction region designs have been developed. One based on a final focusing system using niobium titanium (NbTi) technology, and one using niobium tin ($Nb_3Sn$) technology.

## 5.1 Achromatic Telescopic Squeeze Optics in the LHC and the HL-LHC

The high luminosity collision optics used in the LHC, as well as in the HL-LHC upgrade, employ the so called achromatic telescopic squeeze (ATS) scheme [69–71]. It is applied in the two high luminosity interaction points of LHC (IP1 and IP5) and in the adjacent arcs. The ATS optics increases the luminosity at IP1 and IP5 by enabling lower $\beta^*$ values, while controlling chromatic distortions arising from the high quadrupole gradients required in the interaction regions.

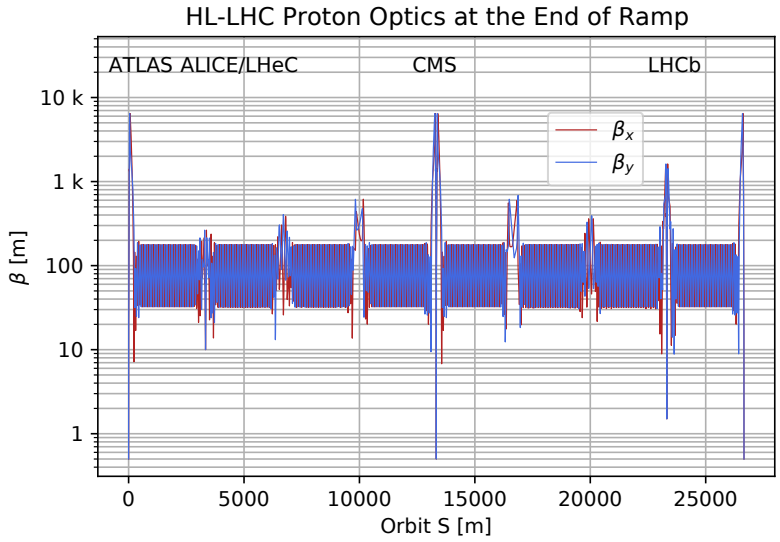


**Figure 31:** Plot of the optics for a round proton beam at the end of the energy ramp, just before the squeeze in the HL-LHC. The amplitude function $\beta(s)$ is plotted against the orbit $s$. In red for the x-plane and in blue for the y-plane. The $\beta^*$ value at ATLAS and CMS corresponds to $50\,\mathrm{cm}$. For improved visibility, a semi-logarithmic scale has been used.

The effectiveness of the sextupoles in the ATS arcs is improved by increasing the amplitude function at every second sextupole. This allows for higher quadrupole gradients in the interaction regions. As a result, the $\beta^*$ value in the interaction points can be further reduced, ultimately increasing the luminosity.

The LHC lattice features four interaction points with their corresponding experiments: IP1 (ATLAS), IP2 (ALICE/LHeC), IP5 (CMS) and IP8 (LHCb). During the so-called *presqueeze*, the amplitude functions $\beta^*$ at the four interaction points are matched to low values with the use of the quadrupole magnets of their corresponding interaction regions. In figure 31 the beam size as a function of the amplitude function of such a *presqueeze* is displayed.

The ATS scheme is applied at the interaction points of the high-luminosity experiments ATLAS and CMS, situated in IP1 and IP5. Additionally to *presqueezing* the beam in these points, the phase advance per arc cell is adjusted to exactly $\pi/2$. This phase advance is crucial for the next step in this type of LHC operation: the so-called *squeeze*. During the *squeeze*, the matching quadrupoles of the adjacent interaction points to the two ATS interaction points are used to push the $\beta^*$ to an even lower value. This causes beta beating waves in these arcs, which reach their maximum at every second sextupoles, due to the matched phase advance in the arc cells [69]. This can be seen in figure 32.

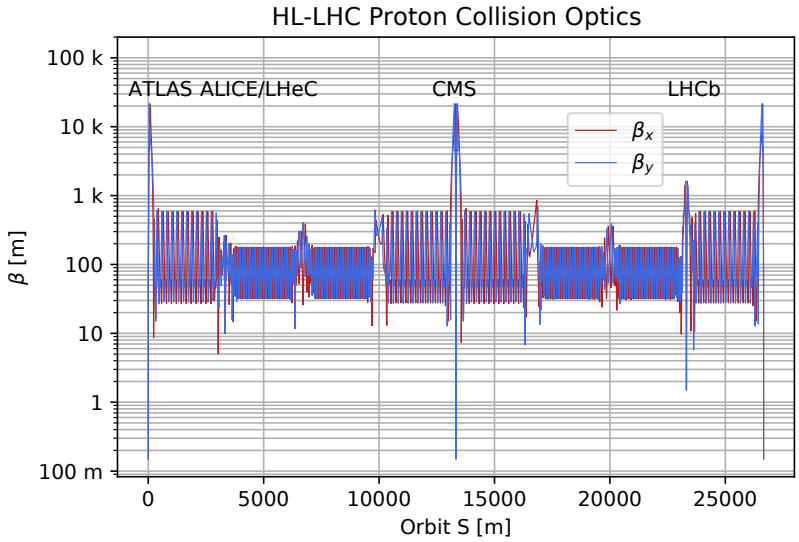


**Figure 32:** Plot of the collision optics for a round proton beam in the HL-LHC. The amplitude function $\beta(s)$ is plotted against the orbit $s$. In red for the x-plane and in blue for the y-plane. The $\beta^*$ value at ATLAS and CMS corresponds to $15\,\mathrm{cm}$. For improved visibility, a semi-logarithmic scale has been used.

In equation 60 the dependence of the the chromaticity $\Delta\xi$ on the amplitude function $\beta(s)$ at a position $s$ and the normalized sextupole strength $k_2$ is displayed. This equation can be found in [72]:

$$\Delta\xi = \frac{1}{4\pi}\int k_2(s)\beta(s)\,\mathrm{ds}. \tag{60}$$

By increasing the amplitude function $\beta(s)$ at locations of the sextupoles, the chromaticity can be controlled more effectively without excessively increasing the strength of the sextupoles $k_2$ or pushing to its operational limits.

The information in this section is based on [69] and [73]. The optics created in this PhD thesis are compatible with the ATS optics designed for the HL-LHC.

## 5.2 High Luminosity Optics for the Niobium Titanium Triplet

The proton beam that will go into collision with the electron beam in IR2 is the clockwise rotating B1, while the counter clockwise rotating B2 will be guided around the e-p collision. For the focusing of the two proton beams, a matching routine has been developed. A simplified version of the designed algorithm is shown in figure 33. It matches different $\beta^*$ values for the two proton beams, as well as includes the electron insertion with the necessary corrections.

The developed routine works by first modeling the collision optics in the HL-LHC lattice for both proton beams without any modifications and saving the optics parameters at several crucial positions in the lattice. In this PhD, a collision optics was used which reaches values of $15\,\mathrm{cm}$ at IP 1/5, $10\,\mathrm{m}$ at IP2 and $1.5\,\mathrm{m}$ at IP8 [74]. Afterwards, the electron insertion is installed and the orbit for both beams is corrected, as explained in section 4. Up until this point, both beams have been treated the same.

In order to fully define a beam optics, eight parameters need to be matched [30]. Starting with the twiss parameters: the amplitude functions $\beta_{\mathrm{x,y}}$ and the correlation functions $\alpha_{\mathrm{x,y}}$ in both planes, in order to define the beam envelope. Additionally, the horizontal dispersion $D_x$, together with its derivative $D'_x$ need to be matched to correct possible off-momentum effects. The vertical dispersion is assumed to be zero. Finally, the phase advances $\mu_{\mathrm{x,y}}$ need to be matched, to make sure that the tune stays at the desired working point and that the ATS criteria are met.

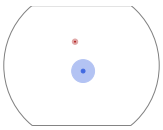

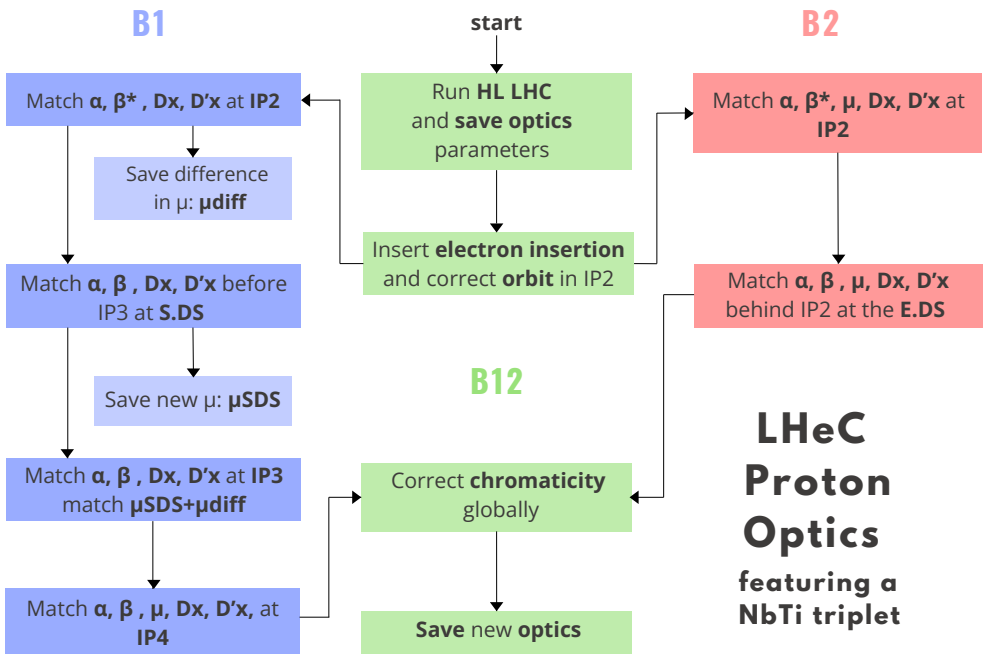


**Figure 33:** A simplified flowchart of the algorithm developed to create the proton optics for LHeC. On the left side the changes performed on the colliding beam B1 (blue) are shown. On the right side the changes performed on the spectator beam B2 are shown (red). In the middle, the changes which concern both beams are shown (green).

Since B1 will collide with the electron beam in IP2, its $\beta^*$ value needs to be as low as possible (see equation 26) at the IP. In the algorithm presented in figure 33, the desired $\beta_{x,y}$* value is matched in IP2 as a first step. The $\alpha_{x,y}$ function in this interaction point is matched to $0$, as this marks the local minimum of this symmetry point. Additionally, the horizontal dispersion $Dx$ and its derivative $D'_x$ are matched to $0$. It was possible to achieve very low $\beta^*$ values by matching these six parameters, but not matching the phase advances $\mu_{x,y}$ in this point. Therefore, the difference between the originally saved $\mu_{x,y}$, and the newly achieved value at the IP, is saved as $\mu_{diff}$. As it was not possible to rematch the phase advance locally in IR2 for such a low $\beta^*$ value, the optics needed to be rematched at the start of the dispersion suppressor (S.DS) in IP3. The dispersion suppressors are often used in matching routines of LHC, since they are placed between the straight interaction regions and the periodic arcs and therefore allow for local corrections in the interaction regions. An example for an optics created this way for B1 is shown in figure 34.

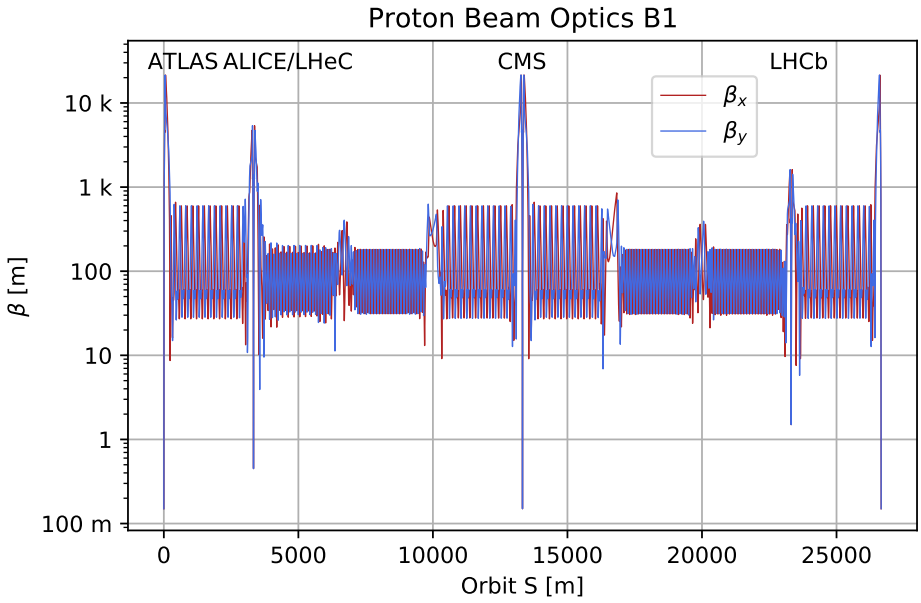


**(a)** Optics extending over the whole length of LHC. The horizontal amplitude function is shown in red, and the vertical amplitude function is shown in blue.

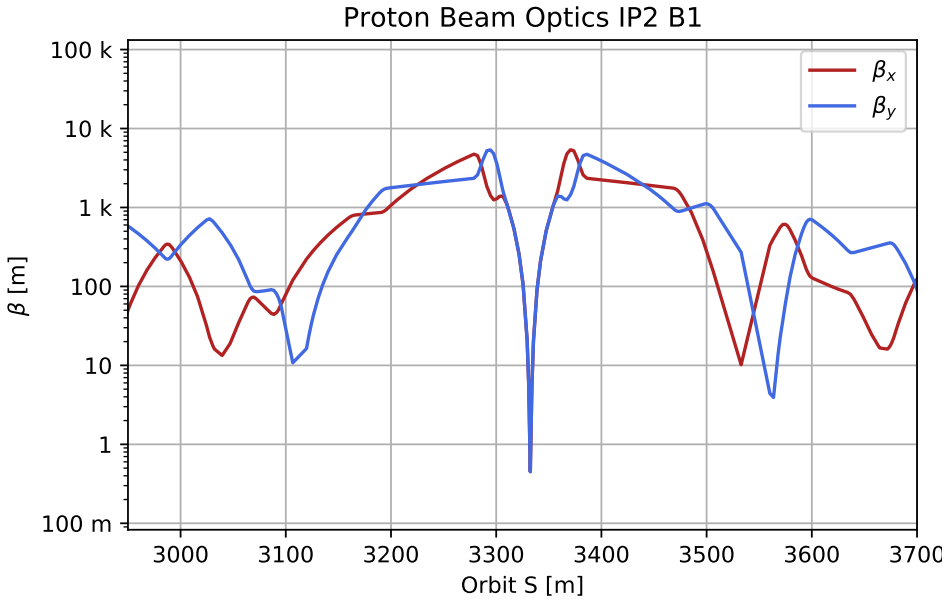


**(b)** Zoom into interaction region 2 for the optics created for B1. In this case a $\beta^*$ value of $45\,\mathrm{cm}$ is displayed.

**Figure 34:** Optics created for LHeC for B1.

After matching six parameters at the dispersion suppressor on the left side of IP3, the difference between the achieved value for $\mu_{x,y}$ and its desired value is saved as $\mu_{diff}+\mu_{SDS}$. This makes it possible to assure that the difference of phase between the S.DS and IP3 does not change, when the optics is rematched in this point. Finally, to recover the phase and the tune, all eight optics parameters are rematched in IP4 of HL-LHC. For proton B2, the match is significantly more simple. This is because all eight optics parameters can be rematched locally at IP2 and downstream at the end of the dispersion suppressor (E.DS.R2). As a last step, the chromaticity of both beams is corrected with the use of the sextupoles in the arcs. All of the matching has been performed using the matching quadrupoles in the used interaction regions, as well as some of the tune correctors and the arc sextupoles. A detailed overview of the used scripts can be found in the appendix A.2. In figure 35 an example of optics designed for B2 is shown.

These plots show that the expansion in the amplitude function at IP2 is significantly larger for B1 than for B2. This is due to the strong focusing of the amplitude function at the IP and due to *Liouville's theorem*.

A set of optics has been created for this machine configuration. In table 5 the designed optics for the two proton beams together with their corresponding e-p luminosities are shown.

| $\beta_1^*$ [m] | 0.2 | 0.25 | 0.3 | 0.35 | 0.45 |
|---|---|---|---|---|---|
| $\beta_2^*$ [m] | 10-40 | 10-40 | 10-40 | 10-40 | 10-40 |
| Luminosity [$\mathrm{cm^{-2}\,s^{-1}}$] | $2.5\times10^{33}$ | $2.0\times10^{33}$ | $1.7\times10^{33}$ | $1.4\times10^{33}$ | $1.1\times10^{33}$ |

**Table 5:** Summary of the optics matched for the two proton beams for the LHeC. B1 is matched to low $\beta_1^*$ values, while B2 is matched to high $\beta_2^*$ values, between $10\,\mathrm{m}$ to $40\,\mathrm{m}$ in steps of $1\,\mathrm{m}$. In the last row of the table the achievable luminosities for the e-p collisions with these corresponding $\beta_1^*$ values are shown. The parameters used for the calculation of the luminosity are taken from 8.

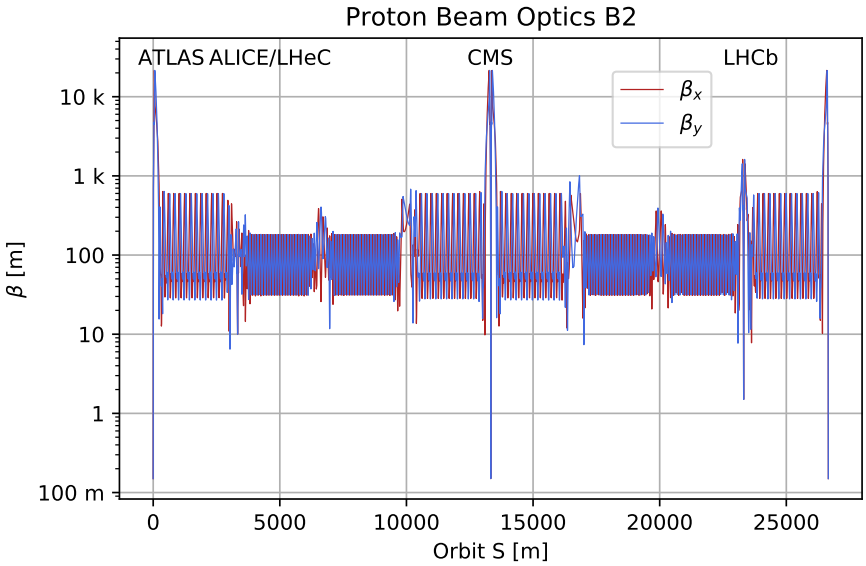


**(a)** Optics extending over the whole length of LHC. The horizontal amplitude function is shown in red, and the vertical amplitude function is shown in blue.

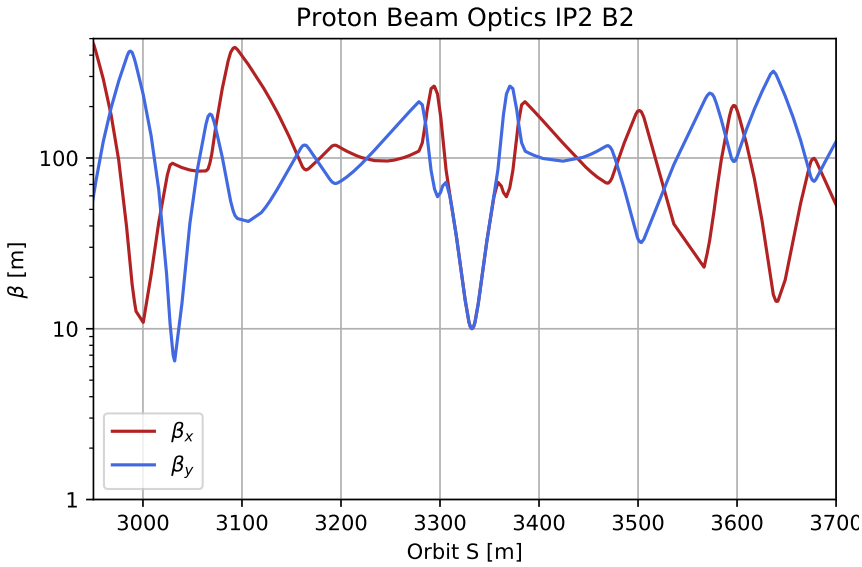


**(b)** Zoom into interaction region 2 for one of the optics created for B2. In this case a $\beta^*$ value of $10\,\mathrm{m}$ is displayed. As the $\beta^*$ is relaxed to higher values, the amplitude function around the IP becomes flatter. This decreases the size of the beam expansion and moves it further away from the center.

**Figure 35:** Optics created for LHeC for B2.

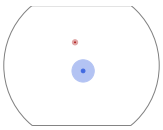

### 5.2.1 Necessary Hardware Changes for this Machine Layout

This interaction region was designed to minimize hardware modifications to the existing LHC layout. It therefore uses the currently installed triplet based on niobium titanium technology. The only necessary hardware changes in this interaction region include:

- **the installation of the electron insertion**
- **a recabling of the quadrupoles used in the interaction region of LHeC**

A detailed description of the installation of the magnets used for the electrons can be found in section 4.

The so called *matching quadrupoles* are the quadrupoles placed symmetrically around the interaction regions to establish a smooth transition between the periodic arcs and the interaction points. In the matching quadrupoles each beam travels through its own beam pipe. The schematic cross section of one such quadrupole, namely a MQY, is shown in figure 36.

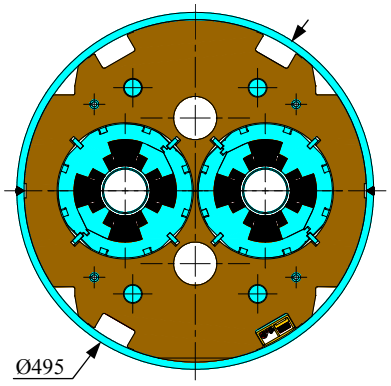


**Figure 36:** Schematic view of one of the quadrupoles used to focus the proton beams before their interaction point. Figure adapted from [57].

This quadrupole has two individually powered apertures, one for each beam, while both apertures share the same yoke. This is the case for all magnets, except

the ones in the interaction regions, where there is only one beam pipe. In the current design, three cables are used to power the matching quadrupoles: one cable each for an individual feed, and one common return cable. This introduces a dependence in the powering of the two apertures of $50\%$ [75].Consequently, one aperture cannot be powered at $100\%$ while the other is operated below $50\%$. If four cables are used, two can be used for an individual feed of each aperture, and two for an individual return. This would result in an independence of powering of the two apertures. During the long shutdown 2 (LS2) between 2019 and 2021, a fourth cable has been installed in IP1 and point IP5 in the scope of the High Luminosity Upgrade [57], to enable independent powering of the two apertures.

In the designed interaction region for LHeC, extremely asymmetric optics were created for the two proton beams. A necessary hardware change for this design would include a recabling of some of the quadrupoles used for their focusing in IP2, similar to the upgrades performed in IP1 and IP5 [76].

## 5.3 High Luminosity Optics for the Niobium Tin Triplet

A second interaction region to the one presented in section 5.2 has been designed in the scope of this thesis. In this design, the currently used niobium titanium (NbTi) triplet in IR2 is replaced with the same niobium tin ($Nb_3Sn$) triplet as foreseen for IP1 and IP5 in the HL-LHC upgrade, see section 3.2.1. The major advantage of this new triplet is that it offers an aperture with more than twice the size of the current one. Table 6 from section 3.2.1 shows the difference of the newly installed triplet magnets Q1, Q2, and Q3. It is repeated here for convenience.

| Parameter | Unit | LHC Q1/Q2/Q3 | HL-LHC Q1/Q2/Q3 |
|---|---|---|---|
| Conductor material | | NbTi | $Nb_3Sn$ |
| Magnetic field gradient | T/m | 205 | 132.6 |
| Magnetic length | m | 6.37/5.5/6.37 | 4.20/7.15/4.20 |
| Aperture radius | mm | 70 | 150 |

**Table 6:** A summary of the magnet values of the triplets of the two interaction points that will be upgraded in the long shutdown 3 (LS3) between 2026 and 2029. The NbTi triplets of IP1 and IP5 will be replaced with triplets made of $Nb_3Sn$. Q1, Q2 and Q3 represent the quadrupoles of the triplets seen in figure 37. These values have been extracted from [57, 60] and [58, 61].

In this design for the LHeC, the same triplet foreseen for IP1 and IP5, has been installed in IP2 of LHC. This triplet makes it possible to achieve a greater beam

separation than with the currently used triplet of NbTi and to focus B1 down to a lower $\beta^*$.

### 5.3.1 Installation of the Niobium Tin Triplet

Several changes need to be performed on IR2, when installing the new triplet magnets. A scaled overview of the performed changes can be seen in figure 37.

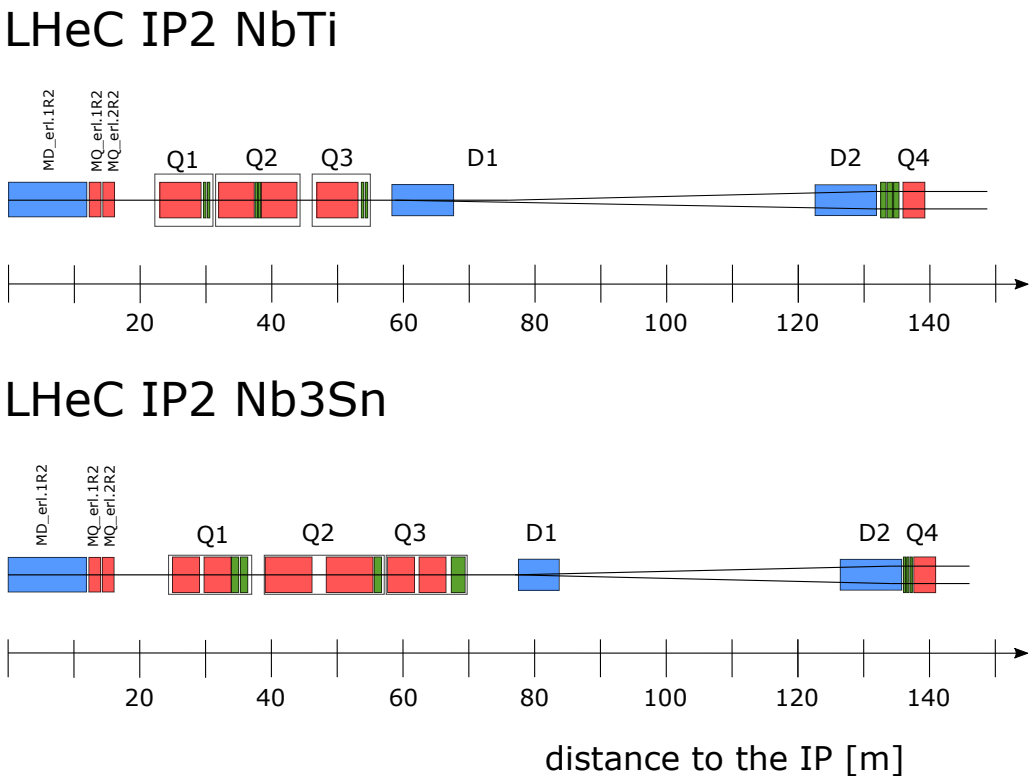


**Figure 37:** Overview of the changes performed to the lattice in IP2, when installing the $Nb_3Sn$ triplet magnets. The magnets Q1, Q2 and Q3 represent the final focusing triplet magnets, where both beams pass through. The magnets D1 and D2 represent the recombination and separation dipoles, which guide the proton beams back into their corresponding beam pipes. In green the nested orbit correctors for the horizontal and the vertical planes are shown. The electron insertion featuring a dipole magnet, as well as two quadrupoles is visible, adjacent to the IP. Finally, the first matching quadrupole, namely Q4, can be seen at approximately $140\,\mathrm{m}$ downstream of the IP.

The new triplet is longer than the old triplet, as can be seen in table 6, as well as in figure 37. In total, $6.3\,\mathrm{m}$ of space need to be gained.

A graphic overview of the hardware changes performed in MAD-X is shown in figure 38. The first step in this routine is thus to remove the triplet magnets, together with their nested correctors. The separation and recombination dipoles D1 and D2 are also removed, together with higher order correctors, such as sextupoles, octupoles, as well as dodecapoles. The beam position monitors (BPMs) in this area are also removed.

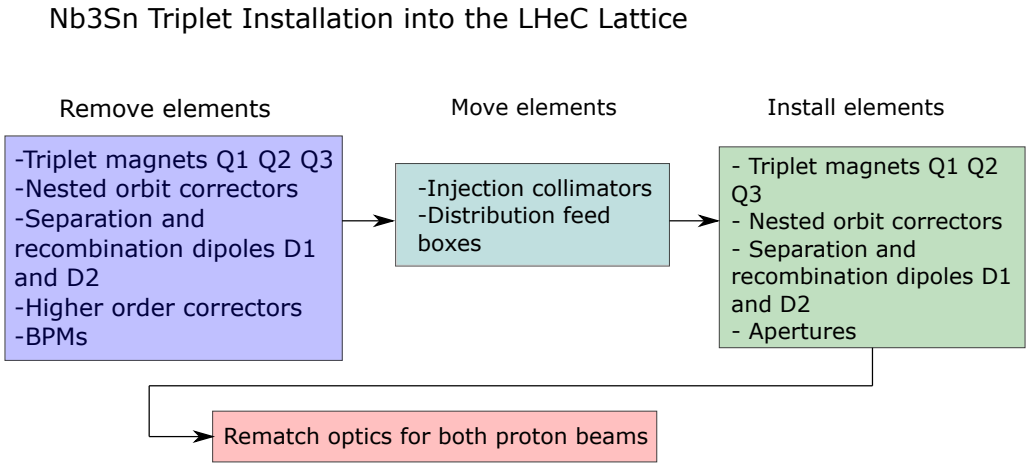


**Figure 38:** A flow chart representing the designed algorithm that was used to install the $Nb_3Sn$ triplet for LHeC into IP2 of the HL-LHC lattice.

Some of the elements were not removed, but moved by $6.3\,\mathrm{m}$, as this space needs to be gained in order to install the $Nb_3Sn$ magnets. The moved elements include the injection collimators, as well as several distribution feed boxes. B1 is injected into LHC in IP2. Therefore this interaction region includes the injection collimators, which put additional boundary conditions on this design. Afterwards, the new elements were installed into the lattice. These include the $Nb_3Sn$ triplet, as well as the nested orbit correctors and the separation and recombination dipoles D1 and D2. These new orbit correctors have a larger aperture, and so do the separation and recombination dipoles. The installed D1 and D2 dipoles are of the same type as those used in the upgraded HL-LHC interaction regions. Finally, the optics for both beams are rematched. In the scope of this thesis, the higher order correctors, as well as the beam position monitors (BPMs) have not been reinstalled, as it is meant to serve as a proof of principle machine layout and higher order effects were not studied for this machine design. These higher order magnets would also need to be replaced by magnets which have a larger aperture, as will be done in the scope of the high luminosity upgrade in IP1 and IP5 [77]. A detailed overview of the changes performed on the HL-LHC lattice during this routine can be found in the appendix A.2.2.

After having been moved, as well as replaced, the bending angles of the two

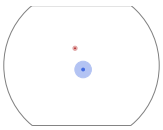

recombination dipoles $D_1$ and $D_2$ need to be revised. A conceptual illustration of the two proton beams passing through the recombination dipoles $D_1$ and $D_2$ can be seen in figure 39. This sketch represents the right side of the interaction region. The two dipoles each deflect the beams by an angle of $\vartheta_{D_{1/2}}$. Since the two proton beams travel in opposite directions, the dipoles deflect them in opposite directions.

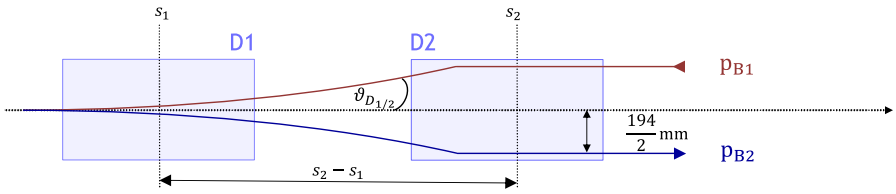


**Figure 39:** Schematic view of the recombination and separation dipoles $D_1$ and $D_2$ and the two proton beams passing through them. The positions $s_1$ and $s_2$ of the corresponding dipoles are marked. After passing through the dipoles, the beams return to their own respective beam pipes with a total distance of $194\,\mathrm{mm}$ between them.

The proton beams in the HL-LHC travel through their own corresponding beam pipes with a distance of $194\,\mathrm{mm}$ between them [78]. Using figure 39, the following relation between the position of the dipoles $s_{1/2}$ and the bending angle of the dipoles $\vartheta_{D_{1/2}}$ can be deduced:

$$\tan(\vartheta_{D_{1/2}}) \approx \frac{0.194\,\mathrm{m}/2}{s_2 - s_1}. \tag{61}$$

With ($s_2$-$s_1$) representing the distance between the two dipoles. This can be rearranged to:

$$\vartheta_{D_{1/2}} \approx \arctan\left(\frac{0.194}{2\,(s_2 - s_1)}\right). \tag{62}$$

This equation has been implemented into this $Nb_3Sn$ triplet installation in MAD-X. The optics of the two proton beams are rematched locally to the round collision optics of HL-LHC values [74]. In these optics a $\beta^*$ value of $10\,\mathrm{m}$ is foreseen at the IP for both proton beams. Both beams are rematched to their original values before they head back into the arcs (at the dispersion suppressors), as well as at the IP.

### 5.3.2 High Luminosity Optics for the $Nb_3Sn$ Triplet

The MAD-X routine developed in order to define the optics for LHeC with the $Nb_3Sn$ triplet is based on a similar procedure as the one developed for the currently used NbTi triplet in subsection 5.2.

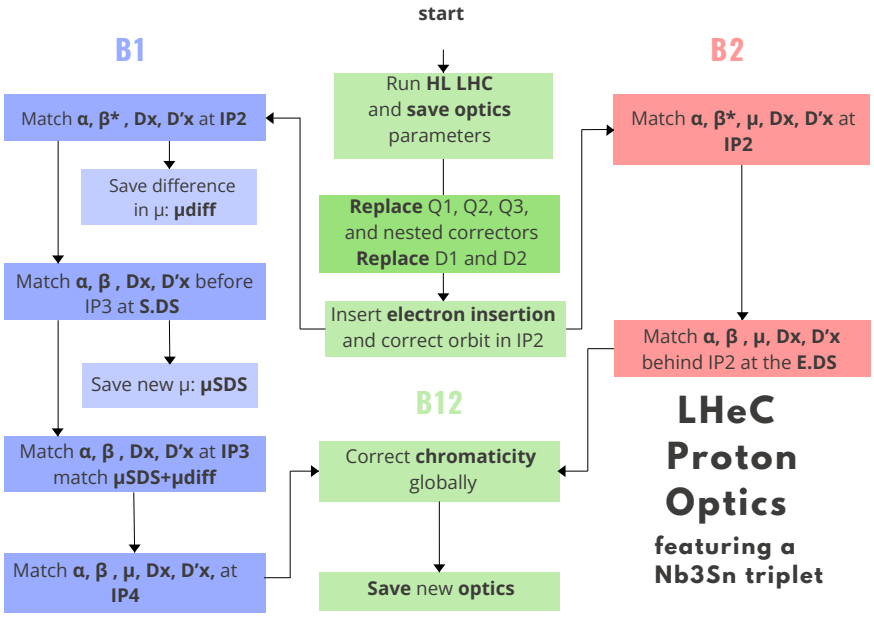


**Figure 40:** Simplified flowchart showing the algorithm designed to match the optics for the two proton beams B1 and B2 for an LHeC interaction region with triplets using $Nb_3Sn$ technology (darker green). On the left side the operations performed for B1 are shown, in the middle the ones concerning both proton beams are shown and on the right side the ones concerning B2 are displayed.

A simplified flowchart of this routine is shown in Fig. 40. The routine is identical to that used to generate the proton optics with the final focusing system based on NbTi technology (Fig. 33), with the additional modification of installing the $Nb_3Sn$ triplet.

In figure 41 an optics created with this algorithm for B1 is shown, while in figure 42 an optics designed for B2 is displayed.

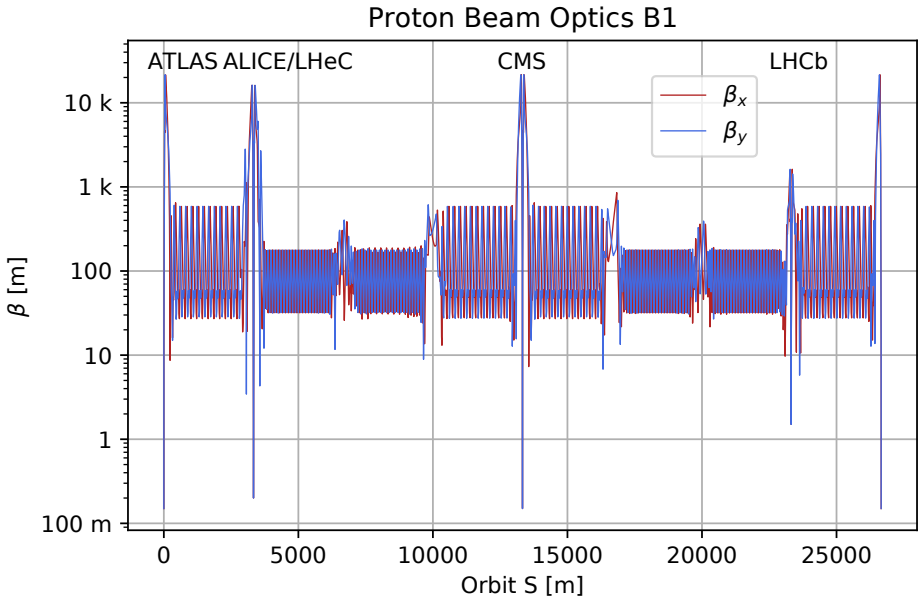


**(a)** Optics extending over the whole length of LHC. The horizontal amplitude function is shown in red, and the vertical amplitude function is shown in blue.

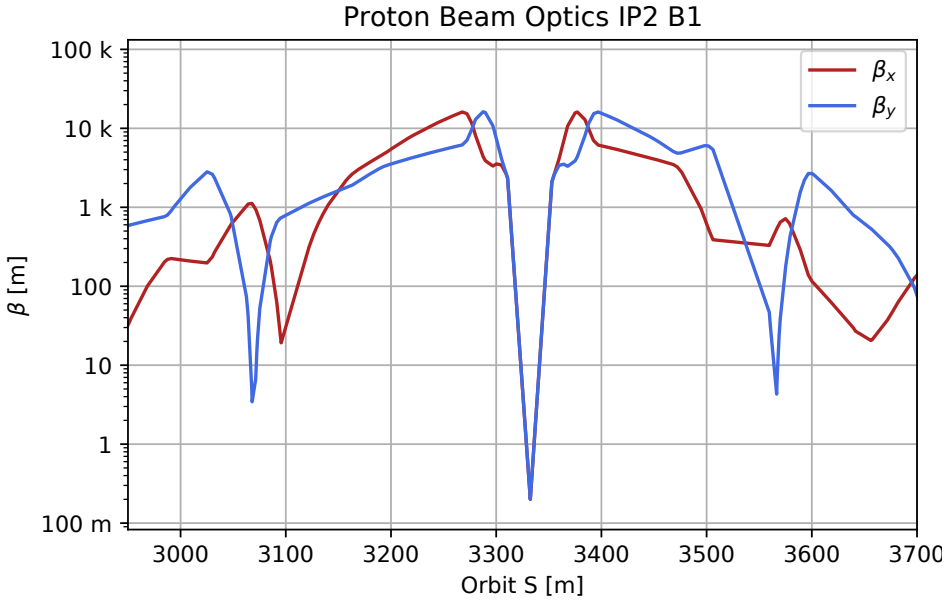


**(b)** Zoom into interaction region 2 for one of the optics created for B1. In this case a $\beta^*$ value of $20\,\mathrm{cm}$ is displayed.

**Figure 41:** Optics created for LHeC for B1.

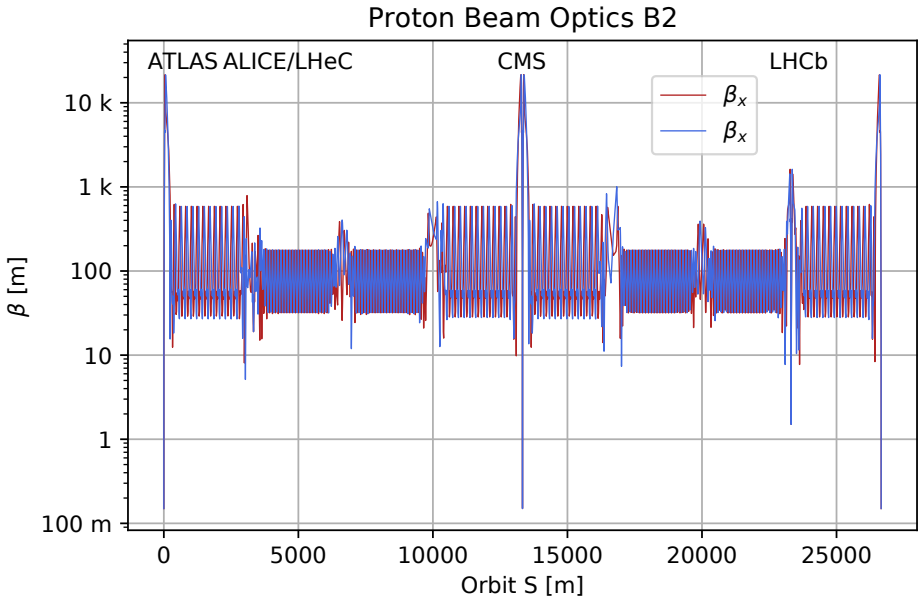


**(a)** Optics extending over the whole length of LHC. The horizontal amplitude function is shown in red, and the vertical amplitude function is shown in blue.

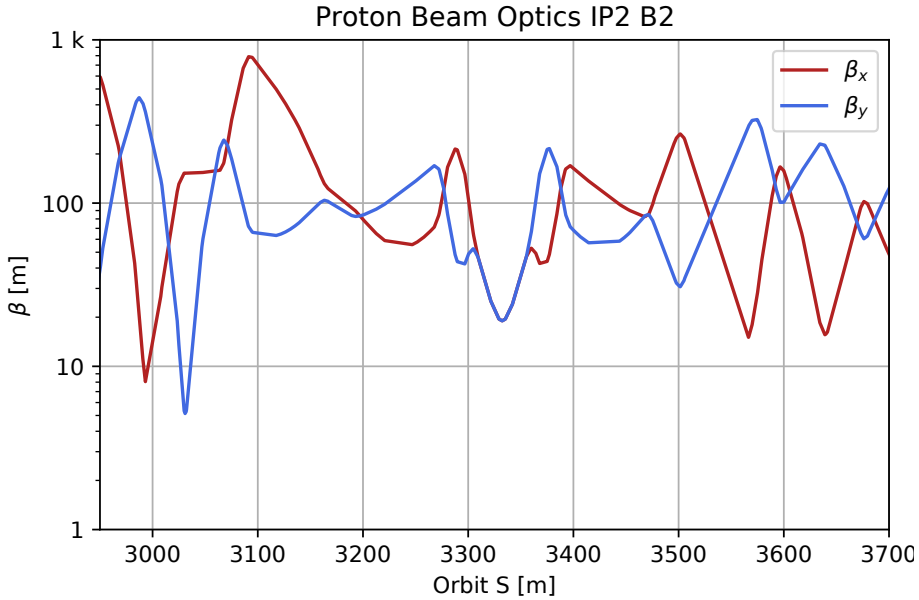


**(b)** Zoom into interaction region 2 for one of the optics created for B2. In this case a $\beta^*$ value of $19\,\mathrm{m}$ is displayed.

**Figure 42:** Optics created for LHeC for B2.

In figure 42 a zoom-in of the interaction region is shown. As B2 is relaxed to high $\beta^*$ values, it does not increase in size as strongly, as it is the case for B1. For B2, a peak of approximately $800\,\mathrm{m}$ can be seen in the horizontal amplitude function upstream of the IP. Since the beam is not tightly squeezed at the IP, it does not expand as close to the IP as B1 does, and the location of the peak is shifted further upstream. Consequently, B2 remains comparatively broad before and throughout the passage through the IP.

This algorithm is used to create a set of optics. The created optics are summarized in table 7 with their corresponding e-p luminosities.

| $\beta_1^*$ [m] | 0.2 | 0.25 | 0.3 | 0.35 |
|---|---|---|---|---|
| $\beta_2^*$ [m] | 14-40 | 14-40 | 14-40 | 14-40 |
| Luminosity [$\mathrm{cm}^{-2}\,\mathrm{s}^{-1}$] | $2.5 \times 10^{33}$ | $2.0 \times 10^{33}$ | $1.7 \times 10^{33}$ | $1.4 \times 10^{33}$ |

**Table 7:** Summary of the proton optics matched for the two proton beams for the LHeC featuring a triplet of $Nb_3Sn$ in IP2. B1 is matched to low $\beta^*$ values, while B2 is matched to high $\beta^*$ values, between $14\,\mathrm{m}$ to $40\,\mathrm{m}$. In the last row of the table the achievable luminosities for the e-p collisions with these corresponding $\beta^*$ values are shown. The luminosities have been calculated using the parameters of table 8.

After creating this set of optics, the optics and orbit configuration that provides the best proton-beam separation and the highest e-p luminosity was chosen with the designed optimization routine in section 6.

# 6 Optimization of the Proton Beam Separation

In LHC the two proton beams share the same beam pipe at the four interaction points: IP1, IP2, IP5, and IP8. During LHeC operation, the clockwise-rotating proton beam (B1) collides with the electron beam in IP2, while the counter-clockwise-rotating proton beam (B2) must be guided around this e–p collision. Within the scope of this PhD, a separation scheme was developed to steer B2 around the e–p collision point. This scheme was first introduced in section 3.3 and is repeated here for convenience and to clarify the variables used.

This chapter presents an optimization routine that was developed to maximize the e-p luminosity while positioning B2 as far as possible from the e-p collisions.

## 6.1 Principle of the Proton Beam Separation

When the two proton beams enter the same beam pipe in the e-p interaction region, they are separated in the horizontal plane with the use of separation bumps. The separation bumps distance the proton beams at the position of the IP from their design orbits by a distance of $\mathrm{sep}_{\mathrm{B1}}$ and $\mathrm{sep}_{\mathrm{B2}}$ for B1 and B2, respectively. This can be seen in figure 43.

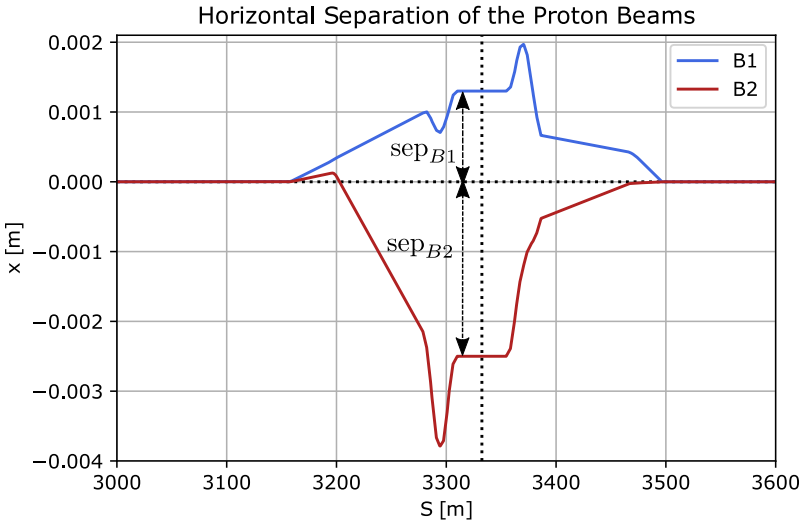


**Figure 43:** Plot showing the horizontal orbit separation of the two proton beams at IP2. The interaction point and the design orbit are indicated by black dashed lines. The horizontal distance between B1 and the design orbit at the IP is denoted as $\mathrm{sep}_{\mathrm{B1}}$, while the distance between B2 and the design orbit is denoted as $\mathrm{sep}_{\mathrm{B2}}$.

In the vertical plane, the two beams are separated with the use of crossing bumps, as shown in figure 44. As they are displaying a crossing of the beams, these angles are referred to as $\mathrm{x}_{\mathrm{B1}}$ for B1 and $\mathrm{x}_{\mathrm{B2}}$ for B2, where the $\mathrm{x}$ represents a cross.

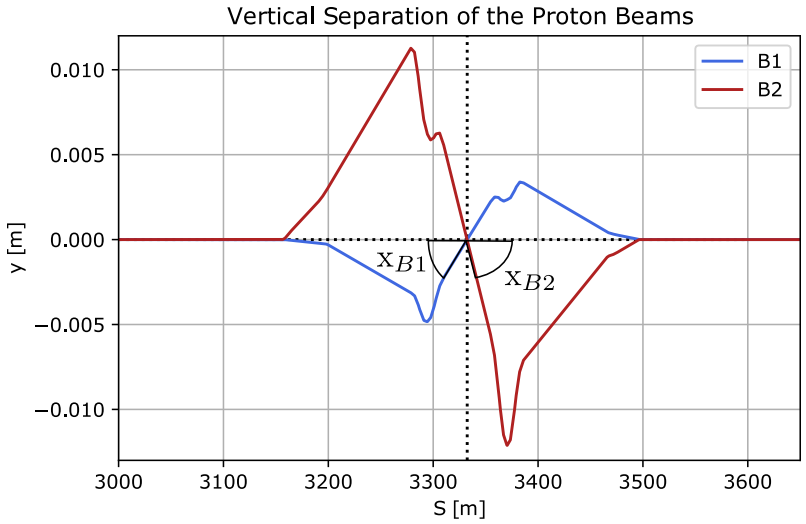


**Figure 44:** Plot showing the vertical orbit separation of the two proton beams at IP2. The interaction point and the design orbit are indicated by black dashed lines. The angle between B1 and the design orbit at the IP is denoted as $\mathrm{x}_{\mathrm{B1}}$, while the angle between B2 and the design orbit is denoted as $\mathrm{x}_{\mathrm{B2}}$.

On each proton beam a separation bump is applied in the horizontal plane, and a crossing bump is applied in the vertical plane. As a result, the spatial separation of the two proton beams in both transversal planes depends on a total of four variables: $\mathrm{sep}_{B1,B2}$ and $\mathrm{x}_{B1,B2}$.

In order to maximize the luminosity of the e-p collisions, as well as to maximize the distance between the two proton beams, asymmetric optics have been used for B1 and B2. B1 is focused down to very low $\beta$* values, while B2 is relaxed to high $\beta$* values to minimize its phase space expansion. A detailed explanation of the creation of the optics can be found in section 5.2. A zoom-in of one such optics of the two proton beams at the LHeC interaction point is displayed in figure 45.

The different $\beta^*$ values for each beam add two more parameters to the possible separation scheme. All variable parameters of the proton beam separation are summarized in table 8.

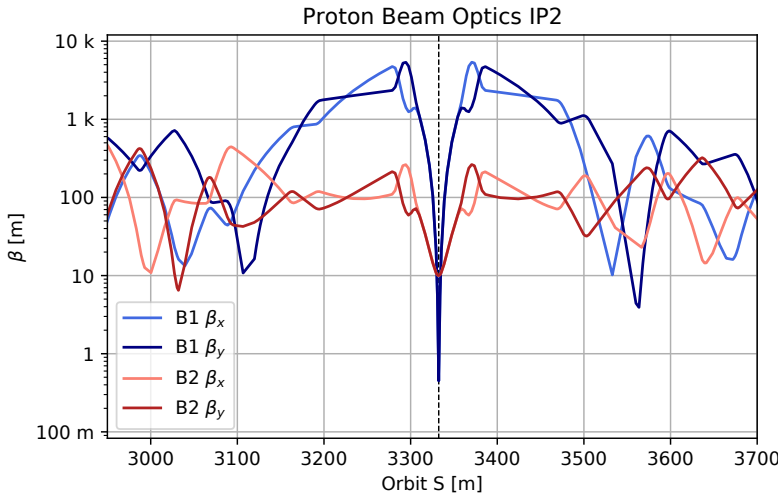


**Figure 45:** Zoomed-in view of the amplitude functions of the two proton beams at IP2, with a value of $0.45\,\mathrm{m}$ for B1, and $10\,\mathrm{m}$ for B2. The position of the IP is marked with a black dashed line.

**Table 8:** Summary of the parameters for the proton beam separation.

| Parameter | B1 | B2 |
|---|---|---|
| Horizontal separation bump | $\mathrm{sep}_{\mathrm{B1}}$ | $\mathrm{sep}_{\mathrm{B2}}$ |
| Vertical crossing angle | $\mathrm{x}_{\mathrm{B1}}$ | $\mathrm{x}_{\mathrm{B2}}$ |
| Betafunction at the IP | $\beta^*_{\mathrm{B1}}$ | $\beta^*_{\mathrm{B2}}$ |

## 6.2 Optimization of the Proton Inter Beam Distance

An optimization routine has been developed in this thesis to maximize the distance between B1 and B2 in IP2 during LHeC operation in their shared beam pipe.

The parameter which has been optimized in this routine is referred to as the inter beam distance $d$. It has been defined as the distance between the centers of the two proton beams.

Figure 46 shows a cross section of the two protom beams in the shared beam pipe of the NbTi interaction region design, with an envelope of $10\,\sigma$. This is at the position of the third triplet quadrupole on the left side of the IP (Q3 in figure 37), approximately $47\,\mathrm{m}$ upstream of the IP. As the two proton beams are separated by

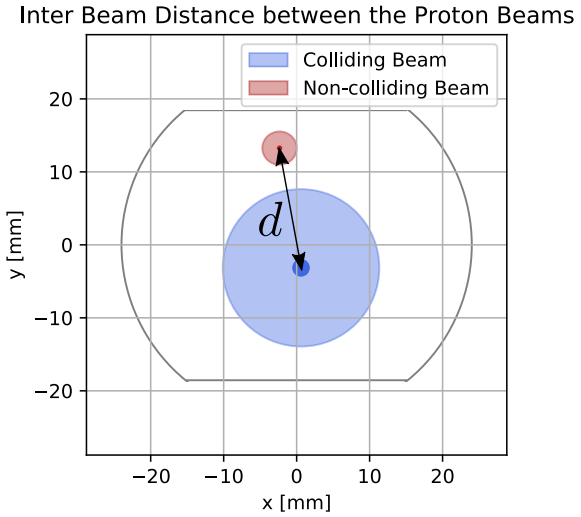


**Figure 46:** Cross section of the beam pipe as the two proton beams pass through the third triplet quadrupole upstream of the IP (MQXA.3L2), at a distance of $47\,\mathrm{m}$. The dark blue region represents $1\,\sigma$ of B1 and the light blue area represents an envelope of $10\,\sigma$. In dark red $1\,\sigma$ of B2 can be seen, enclosed by an envelope of $10\,\sigma$ in lighter red. In light grey the aperture limit of the beam screen is indicated. The black line shows the inter beam distance $d$ between the two centers of the proton beams.

a combination of orbit bumps, one can see that their beam centers are offset with respect to the center of the beam pipe. As this is a representation of B1, before being focused down for collision, it is now already significantly larger than B2, since the optics of B1 show a major expansion before the IP (see figure 45). The distance $d$ between the two centers of the proton beams is indicated in this plot with a black line.

The distance $d$ can be measured in $\mathrm{m}$ or in units of beam sizes $\sigma$. To estimate the effective separation between the two proton beams, it is convenient to normalize this distance to the beam size. When measuring this distance in units of beam sizes, it can be defined in units of sigma of B1 ($\sigma_{\mathrm{B1}}$) or in units of sigma of B2 ($\sigma_{\mathrm{B2}}$) or in units of the average of their beam sizes B12 ($\sigma_{\mathrm{B12}}$).

The distance $d$ is calculated using:

$$d = \sqrt{(x_1 - x_2)^2 + (y_1 - y_2)^2} = \sqrt{\Delta x^2 + \Delta y^2} \tag{63}$$

In this equation $x_{1,2}$ and $y_{1,2}$ mark the transversal orbit positions of proton B1 and B2, respectively. One example of these values can be seen in figure 47. Here, another cross section of the two proton beams is shown. This time the beams are

positioned in the triplet downstream of the IP (Q2). This plot shows how B1 is squeezed into an oval shape.

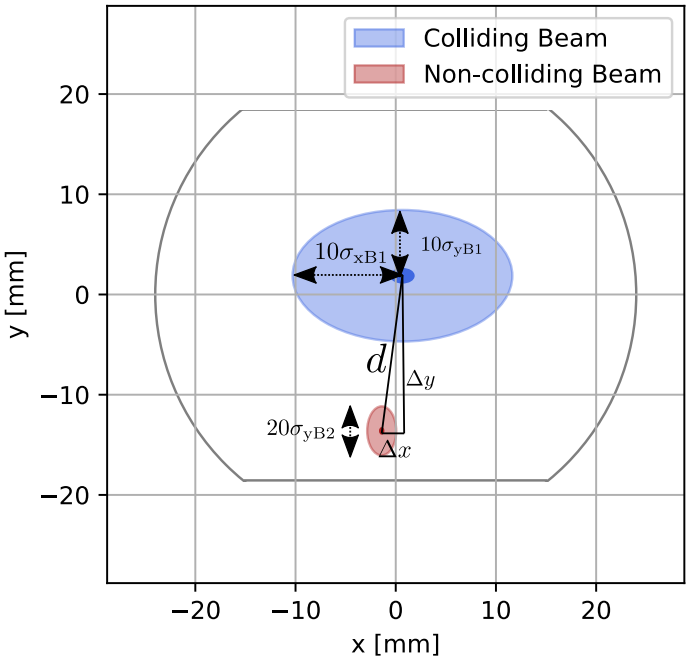


**Figure 47:** Cross section of the beam pipe as the two proton beams pass through the second triplet magnet on the right side of the IP (Q2). The dark blue region represents $1\,\sigma$ of B1 and the light blue area represents an envelope of $10\,\sigma$. In dark red $1\,\sigma$ of B2 can be seen, enclosed by an envelope of $10\,\sigma$ in lighter red. In light grey the aperture limit of the beam screen is indicated. The black line represents the inter beam distance $d$ between the two centers of the proton beams.

The beam size $\sigma(s)$ at a position $s$ is given as:

$$\sigma(s) = \sqrt{\beta(s) \cdot \varepsilon}. \tag{64}$$

Where $\varepsilon$ represents the energy dependent emittance and $\beta(s)$ the amplitude function. Since the two proton beams have asymmetric optics, they vary greatly in their amplitude function, as can be seen in figure 45.

Figure 48 defines the radii of the beam ellipses along $d$. $r_{1,2}$ represent the semi-axes of the beam ellipse of B1 and B2, respectively. These are representations of the actual beam shapes, which are elliptical, and should not be confused with the phase space ellipse defined in section 2.1.2.

Using figure 48, the angular coordinate $\vartheta$ of the ellipses can be calculated using:

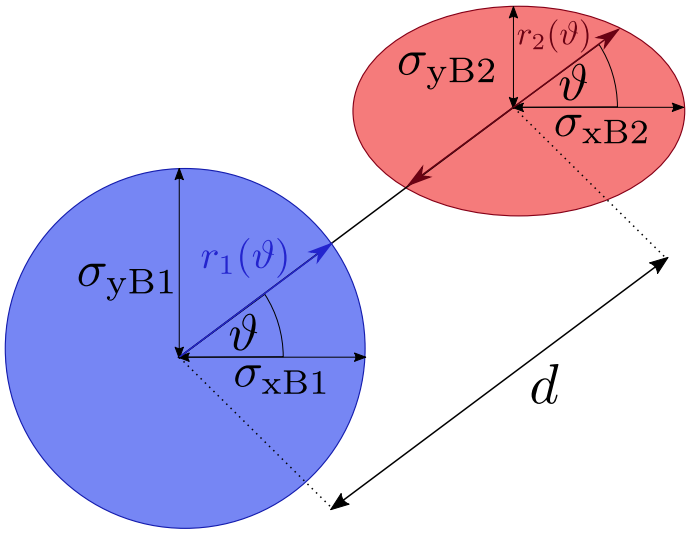


**Figure 48:** Schematic view of the two proton beam ellipses. Here, the blue region represents $1\,\sigma$ of B1. In red $1\,\sigma$ of B2 can be see. The black line represents the inter beam distance $d$ connecting the two centers of the proton beams. The radii $r_1$ and $r_2$ correspond to the local semi-axes of the two beam ellipses along $d$.

$$\vartheta = \arctan\left(\frac{\Delta\, y}{\Delta\, x}\right) \tag{65}$$

For an ellipse with the semi-major axis $a$ and the semi-minor axis $b$, the radius at the polar angle $\vartheta$ can be calculated with [79]:

$$r(\vartheta) = \frac{a \cdot b}{\sqrt{(b\cos(\vartheta))^2 + (a\sin(\vartheta))^2}} \tag{66}$$

With equation 16 and figure 48, the radii of the beams can be expressed as:

$$r_i(\vartheta) = \frac{\sigma_x \cdot \sigma_y}{\sqrt{(\sigma_y\cos(\vartheta))^2 + (\sigma_x\sin(\vartheta))^2}} \tag{67}$$

Here, index $i = 1, 2$ denotes the corresponding proton beam. The parameters $\sigma_x$ and $\sigma_y$ are the beam sizes in the horizontal and vertical planes, respectively, corresponding to the semi-axes of the beam ellipse. The function $r_i(\vartheta)$ represents

the radius of the ellipse along a line at an angle $\vartheta$ relative to the horizontal axis. It therefore represents the beam size in the direction of $d$.

The inter beam distance $d$ in units of the beam size $\sigma$ can then be defined as such:

$$d\left[\sigma_i\right] = \frac{\sqrt{\Delta x^2 + \Delta y^2}}{r_i(\vartheta)}. \tag{68}$$

This equation is used in this optimization to express the inter beam distance in convenient units of the beam size of B1 and B2. In order to express $d$ in units of the average beam sizes, the mean radius of the beam ellipses along the inter beam distance $d$ is calculated with:

$$\sigma_{B12} = \frac{r_1(\vartheta) + r_2(\vartheta)}{2}. \tag{69}$$

Plugging this into equation 68, the inter beam distance expressed in the mean beam size $d\left[\sigma_{\mathrm{B12}}\right]$ can then be calculated as such:

$$d\left[\sigma_{\mathrm{B12}}\right] = 2 \cdot \frac{\sqrt{\Delta x^2 + \Delta y^2}}{r_1(\vartheta) + r_2(\vartheta)}. \tag{70}$$

Figure 49 shows the inter beam distances in the shared beam pipe between the two proton beams for the optimal configuration scenario. In this case the following parameters were used: $\beta_1^*$= 0.45 m, $\beta_2^*$= 40 m, $\mathrm{sep_{B1}}$ = 0.5 mm, $\mathrm{sep_{B2}}$ = 2.0 mm, $\mathrm{x_{B1}}$ = 80 µrad and $\mathrm{x_{B2}}$ = 350 µrad. The following sections will explain why this combination of parameters was chosen. The position of the IP, as well as the positions of the triplet magnets are marked on the x-axis. The inter beam distance is calculated from the moment the protons pass through the separation and recombination dipole into their shared beam pipe until they are guided back into their own beam pipe at the other separation and recombination dipole.

In figure 49, three different curves are shown. They represent the inter beam distance $d$ measured in beam sizes of B1 (blue), B2 (red) or their mean size B12 (green). The plot shows how much the inter beam distance varies depending on which beam's units are used for the measurement. It is helpful to look at the optics in figure 45 of these two beams to understand why: when measuring in units of $\sigma_{\mathrm{B2}}$, the separation is mainly achieved by the orbit manipulation, since B2 barely changes in size. Therefore the minimum is reached at the IP, where both

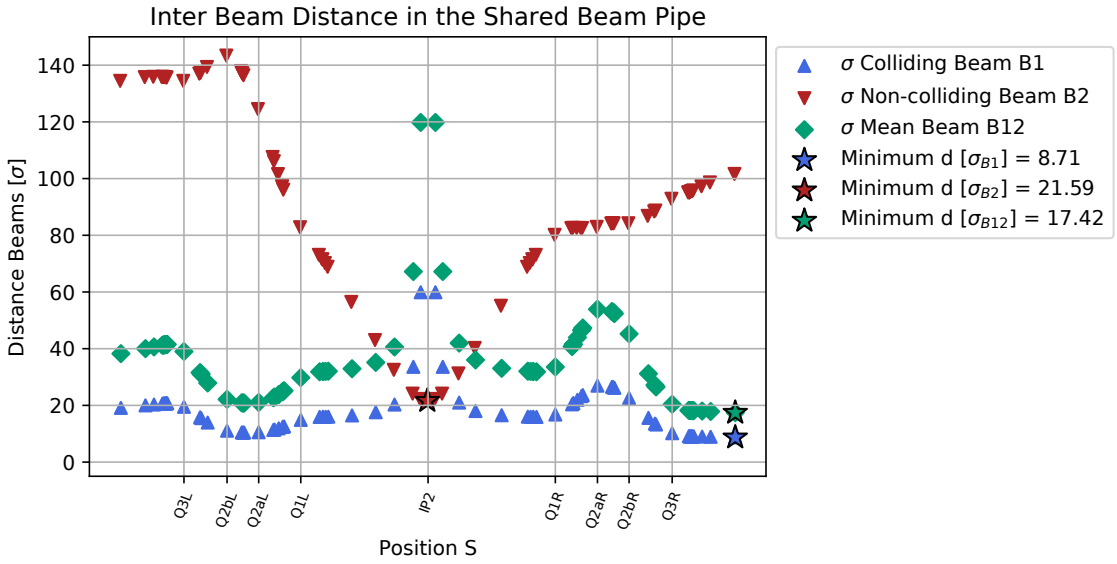


**Figure 49:** Inter beam distance between the two proton beams in their shared beam pipe. In blue in units of $\sigma_{\mathrm{B1}}$ and in red in units of $\sigma_{\mathrm{B2}}$. In green in units of the mean beam size $\sigma_{\mathrm{B12}}$. The stars mark the corresponding minimums for each unit. The position of the IP, as well as the positions of the triplet magnets are marked.

beams are separated only in the horizontal plane. When measuring in units of $\sigma_{\mathrm{B1}}$, the largest inter beam distance is reached at the IP, since the size of B1 reaches the minimum there (not shown in this plot for scaling reasons, as it reaches values higher than $300\,\sigma_{\mathrm{B1}}$). In this case, the smallest inter beam distance is reached downstream of the IP, just before the two proton beams are led back into their corresponding beam pipes. This is partly due to the fact that here the orbit bumps are almost completely closed again reducing their separation (see figure 43 and figure 44), and partly bececause the beam size of B1 is still significant at this point. B1 massively increases in size in the triplet magnets , and thus this region sees a sharp drop of the inter beam distance. When the inter beam distance is measured in the mean beam size $d\ [\sigma_{\mathrm{B12}}]$, the plot keeps a similar shape as for when measuring the inter beam distance in units of B1, but is offset to higher values .

## 6.3 Luminosity Constraints of the Optimization

Among other factors, the luminosity of LHeC is limited by the mechanical aperture of its interaction region, as well as the beam-beam interaction. These limitations had to be taken into account when optimizing the distance between the two proton beams. The detrimental beam-beam effects are stronger the closer the

proton beams are, and it is therefore favorable to maximize the distance between them. On the other hand, the size of the beam pipes limit the phase space expansion as well as the separation of the proton beams. These two constraints limit the push for low $\beta^*$ values and as a result, a higher luminosity.

### 6.3.1 Beam-Beam Effects

As the two proton beams pass next to each other, they exert electromagnetic beam-beam forces on each other. These destructive forces are particularly strong in the four interaction regions, as in these regions the beams share a common beam pipe. It is therefore crucial to keep a certain safety margin between the two proton beams during LHeC operation. In IP1 and IP5 the proton beams are separated before and after the IP with crossing bumps for their p-p operation, precisely to diminish the beam-beam effects. According to the HL-LHC design report [80] and [62] a minimal distance of $12.5\,\sigma$ at the start of collisions and $9.7\,\sigma$ at the end of leveling[2] is necessary between the proton beams to assure the longevity of the beams in the HL-LHC complex for round beams. This value of $12.5\,\sigma$ was taken as an outer constraint for the proton beam separation during the e-p collisions in IR2 in the optimization process of the proton beam separation. It should be noted however, that it would be necessary to perform a beam-beam study, to assure that this inter beam distance suffices.

### 6.3.2 Aperture Limitations

It is not possible to increase the size of the orbit bumps or the size of the beams indefinitely, as the beams are limited in their size by the aperture of the beam pipe. By squeezing the colliding beam, it increases massively in its size before the collision and can therefore not necessarily fit safely into the available aperture. This is a major limitation on the luminosity of this machine design.

The *beam stay clear* is defined as the minimum aperture available between the beam and the beam screen[3] in units of beam size $\sigma$ [57]. In MAD-X, the minimal beam stay clear $n_1$ can be calculated directly with the *aperture* command. It works by first defining the aperture of each element in a certain area of the accelerator

[2] During a fill of protons in LHC, the luminosity would decrease over time, as more and more particles have participated in the collisions or have been lost due to other effects. Levelling in an accelerator attempts to keep the luminosity constant during one fill, by manipulating the beam parameters (such as the size or the position of the beams).

[3] Beam screens shield the superconducting magnets from the beam and therefore represent the minimal effective aperture to the beam.

lattice. This is done by taking the mechanical shape of each element into account and by adding radial tolerances of the beam, such as a spread in energy or orbit distortions, to it. In order to do so, the optics of the beam need to be defined before performing the aperture calculation. The $n_1$ value of a certain segment of the accelerator is then defined as the minimal distance from the center of the beam to the tolerance limit in units of $\sigma$. This is a simplified explanation of how the minimal beam stay clear $n_1$ in MAD-X is computed and more information can be found here [81, 82].

In the original LHC design, a minimum aperture of $8.4\,\sigma_{\mathrm{x,y}}$ [83] is required in both transverse planes during operation. During the HL-LHC upgrade the normalized beam emittance will decrease from $3.75\,\mu\mathrm{m}$ to $2.5\,\mu\mathrm{m}$ and hence the total aperture in units of beam size increases [84]. For the injection process in HL-LHC, it was concluded, that the minimum aperture anywhere in the ring needs to be at least $7.7\,\sigma$ for an ideal scenario without imperfections. When considering imperfections ($\beta$-beat, alignment errors) an aperture of $10.6\,\sigma$ is necessary [85].The interaction regions require a margin of $10\,\mathrm{sigma}$ [74].

In the designs in this PhD, an absolute minimal beam stay clear $n_1$ of $7.7\,\sigma$ was adopted as an outer constraint for the NbTi triplet, as the aim was to push for the highest possible luminosity without performing major hardware changes in the machine layout. The $Nb_3Sn$ triplet offers significantly more aperture, which allowed the beam parameters to be optimized such that a beam stay-clear of $10\,\sigma$ could be reached. The available aperture of LHeC is studied in more detail in the tracking calculations in section 7.

## 6.4 Inter Beam Distance Optimization for the LHeC IR Using a NbTi Triplet

The optimization for the proton beam separation in the e-p interaction region during LHeC operation has been performed for both triplet magnet technologies (NbTi and $Nb_3Sn$). An example of this optimization is presented in this subsection for the NbTi triplet and in subsection 6.5 for the $Nb_3Sn$ triplet.

### 6.4.1 Defined Parameter Space

The $\beta^*_{\mathrm{B1}}$ value for B1 in the LHeC IR using a NbTi triplet was chosen after running a parameter scan over different optics and orbit configurations. They ranged from a $\beta^*_{\mathrm{B1}}$ value of $0.2\,\mathrm{m}$ to $0.7\,\mathrm{m}$. After careful consideration, a $\beta^*_{\mathrm{B1}}$ value of $0.45\,\mathrm{m}$ was chosen . With this value, the beam can just fit into the available aperture, while

leaving enough room to displace it in order to make space for the second proton beam.

The used optimization process will be demonstrated in this chapter for $\boldsymbol{\beta^*_{B1}}$**=0.45 m**. The parameters that were used in this exemplary scan are summarized in table9.

| Beam | $\beta^*$ [m] | sep [mm] | x [$\mu$rad] |
|---|---|---|---|
| B1 | 0.45 | 0.5, 0.55 | 60, 80 |
| B2 | 10 to 40 in steps of 1 | 1, 2 | 300, 350 |

**Table 9:** Parameters that were scanned for the optimal beam configuration for the proton beam separation in IR2 for $\beta^*_{\mathrm{B1}} = 0.45\,\mathrm{m}$.

In total, these parameters yield: $\mathrm{n}_{\beta^*_{\mathrm{B1}}} \cdot \mathrm{n}_{\beta^*_{\mathrm{B2}}} \cdot \mathrm{n}_{\mathrm{sep_{B1}}} \cdot \mathrm{n}_{\mathrm{sep_{B2}}} \cdot \mathrm{n}_{\mathrm{x_{B1}}} \cdot \mathrm{n}_{\mathrm{x_{B2}}} = 1 \cdot 31 \cdot 2 \cdot 2 \cdot 2 \cdot 2 = 496$ different combinations.

### 6.4.2 Optimal Inter Beam Distance

In this optimization $d\,[\sigma_{\mathrm{B12}}]$ has been maximized while taking into account the optics dependence of $d\,[\sigma_{\mathrm{B2}}]$. $d\,[\sigma_{\mathrm{B1}}]$ is analyzed in more detail in appendix A.3. The inter beam distances $d\,[\sigma_{\mathrm{B12}}]$ are first calculated for each of the 496 configurations of table 9, and the the minimum $d$ for each configuration is saved. Figure 49 shows the optimal configuration, with the minimum $d\,[\sigma_{\mathrm{B12}}]$ marked with a green star.

For each orbit configuration of B1 (four in total, as can be seen in table 9), these minimal $d\,[\sigma_{\mathrm{B12}}]$ are plotted against the corresponding $\beta^*_{\mathrm{B2}}$ value of this configuration. As there are also four orbit configurations for B2, four curves are plotted. This is shown in figure 50 for the chosen orbit configuration of B1.

In figure 50 a *very* slight decrease of $d\,[\sigma_{\mathrm{B12}}]$ with a rising $\beta^*_{\mathrm{B2}}$ can be observed. However, considering the scale of these, no meaningful dependence could be identified. The size of B2 varies very little, compared to its distance to the center of B1. As can be seen in equation 70, the effect of the optics of B2 is therefore very small, when calculating $d\,[\sigma_{\mathrm{B12}}]$.

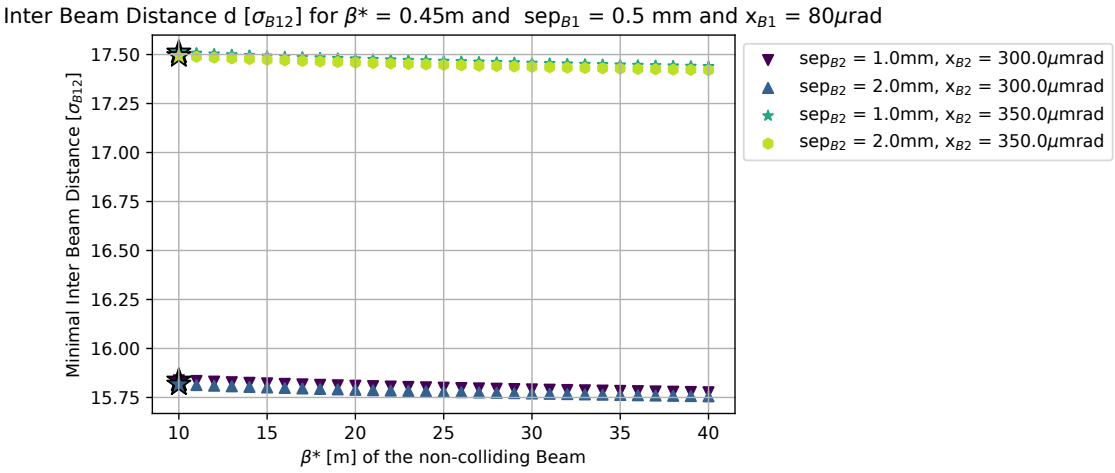


**Figure 50:** Minimal inter beam distances $d\ [\sigma_{\mathrm{B12}}]$ between the two proton beams in their shared beam pipe for $\beta^*_{\mathrm{B1}} = 0.45\,\mathrm{m}$. They are plotted for the chosen orbit configuration of B1 in table 9 as a function of $\beta^*_{\mathrm{B2}}$. Four different curves are shown, for four different orbit configurations of B2. The chosen inter beam distance values are marked with a star. For these points $\beta^*_{\mathrm{B2}}$=10 m.

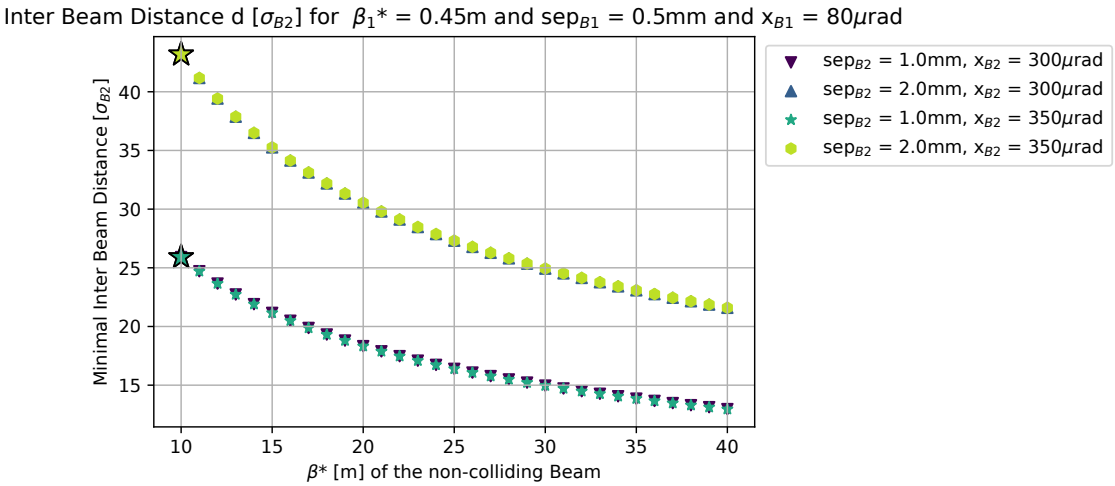


**Figure 51:** Inter beam distance $d[\sigma_{B2}]$ between the two proton beams in their shared beam pipe for $\beta^*_{\mathrm{B1}} = 0.45\,\mathrm{m}$. It is plotted for the chosen orbit configuration of B1 in table 9 as a function of $\beta^*_{\mathrm{B2}}$. Four different curves are shown, for four different orbit configurations of B2. The chosen inter beam distance values are marked with a star. For these points $\beta^*_{\mathrm{B2}}$=10 m.

In figure 51 $d\ [\sigma_{\mathrm{B2}}]$ is shown, as a function of $\beta^*_{\mathrm{B2}}$ for the optimal orbit configura-

tion of B1 and all orbit configurations of B2. For $d\ [\sigma_{\mathrm{B2}}]$, the shape of the curve looks very different to the one of $d\ [\sigma_{\mathrm{B12}}]$. A clear dependence on the optics of B2 can be seen, as the curve falls steeply with a rising $\beta^*_{\mathrm{B2}}$. The minimal inter beam distance in $\beta^*_{\mathrm{B2}}$ is reached at the IP, as can be seen in the example in figure 49. As $\beta^*_{\mathrm{B2}}$ increases, the minimal inter beam distance in units of $\sigma_{B2}$ at the IP decreases. The lowest inter beam distance in $\beta^*_{\mathrm{B2}}$ is thus reached at $40\,\mathrm{m}$. At this point it just exceeds the mandatory $12.5\,\sigma$ defined in section 6.3.1.

For all configurations, a $\beta^*_{\mathrm{B2}}$ of $10\,\mathrm{m}$ reaches the greatest inter beam distance and thus, this value was chosen for the optics of B2. Since the optics of B1 and B2 have been fixed ($\beta^*_{\mathrm{B1}}$=$0.45\,\mathrm{m}$ and $\beta^*_{\mathrm{B2}}$=$10\,\mathrm{m}$), these parameters can be excluded. All orbit configurations are then summarized in figure 52. In this plot, the smallest inter beam distance for each orbit configuration and the corresponding chosen optics configuration (marked as stars in figure 50) is plotted.

With figure 52, it was decided that configurations which do not reach $17\,\sigma$ could be discarded. These include all configurations with $\mathrm{x_{B1}} = 60\,\mu\mathrm{m}$ (points on the left side of this figure), as well as the combinations with $\mathrm{x_{B2}} = 300\,\mu\mathrm{m}$ (lower points on the right). This breaks down the possible parameter combinations to only four orbit configurations. The final configuration is chosen by also considering the beam stay clear of the two proton beams.

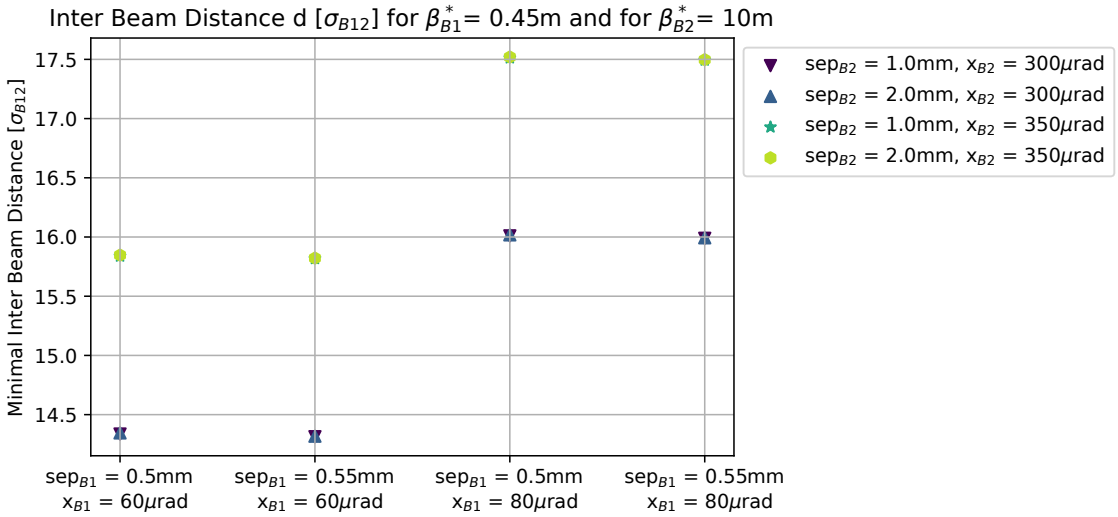


**Figure 52:** Plot of the minimal inter beam distance in the shared beam pipe $d\ [\sigma_{\mathrm{B12}}]$ for $\beta^*_{\mathrm{B1}}$= $0.45\,\mathrm{m}$ and $\beta^*_{\mathrm{B2}}$= $10\,\mathrm{m}$. Each point represents the minimal inter beam distance in the shared beam pipe for this particular orbit configuration. Each color/shape of point represents a different orbit configuration of B2. The x-axis indicates the orbit configurations of B1.

### 6.4.3 Optimal Beam Stay Clear

In order to choose the optimal parameter configuration in figure 52, the beam stay clear for B1 is additionally investigated. The beam stay clear of B2 does not need to be investigated, as this beam never gets particularly close to the beam screen (see appendix A.3). For every configuration of table 9, the beam stay clear in IR2 is therefore calculated. This can be seen for the optimal parameter set in figure 53.

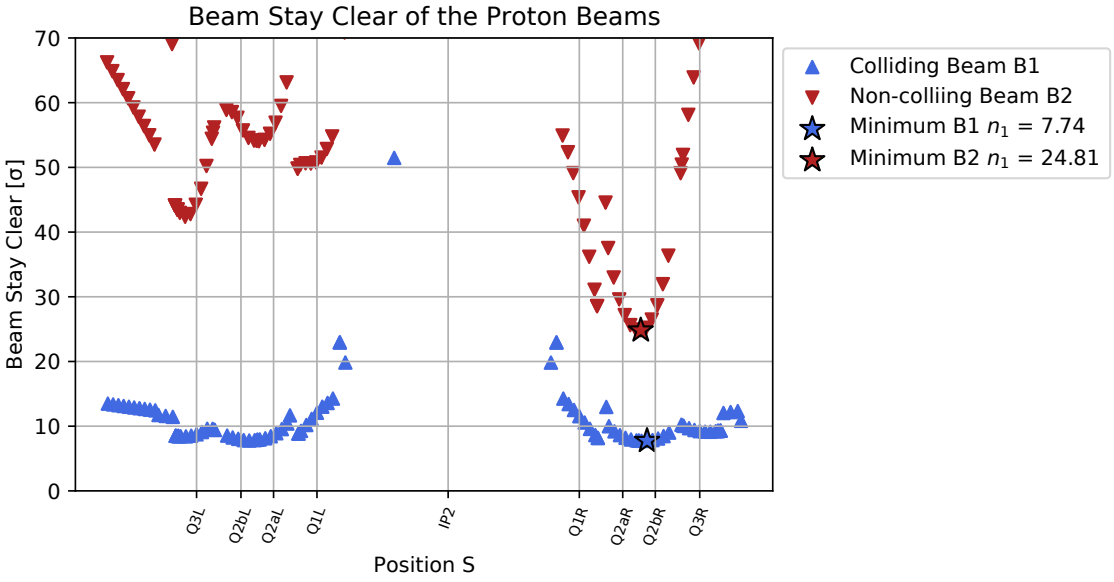


**Figure 53:** Beam stay clear $n_1$ values in units of beam size $\sigma$ for the two proton beams in their shared interaction region. The stars mark the minimal beam stay clear $n_1$ for each beam.

Figure 53 shows that the proton beams reach their lowest $n_1$ value in the triplets. This is, where B1 is significantly increased in size, as well as pushed closer to the beam pipe with the orbit bumps. B2 reaches the peak of its vertical orbit bump at the spot of its lowest $n_1$ value (see figure 44). Each minimal beam stay clear $n_1$ for B1 (the red star in figure 53) is then saved. As it has been done for the inter beam distance, the saved $n_1$ values are plotted along the $\beta^*_{B2}$ of the non colliding proton beam for each orbit configuration of B1. This can be seen for the chosen orbit configuration of B1 in figure 54 for B1.

The $n_1$ values of B1 from the plot in figure 54 show that these values are almost independent of the optics of B2, but do depend on the orbit configuration. A *very slight* dependency on the optics can be seen, but considering their scale, it was

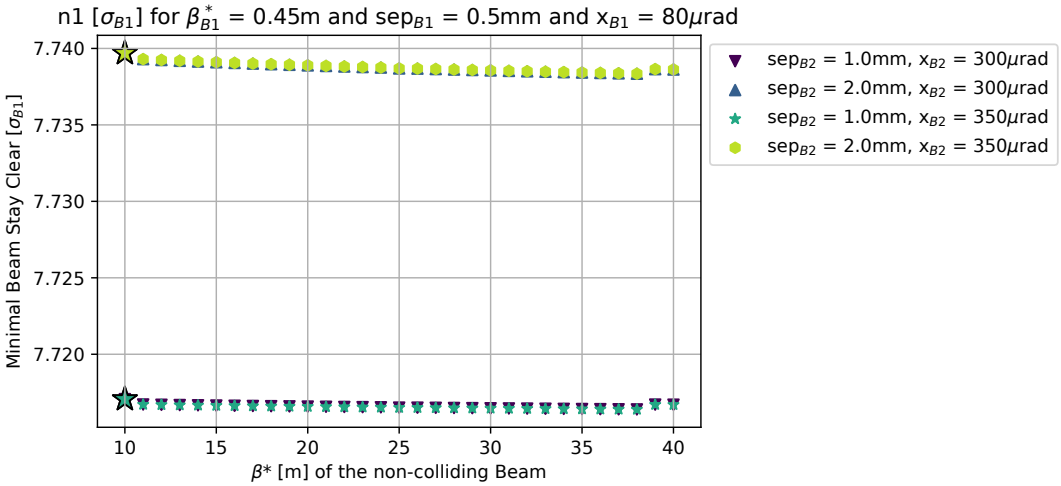


**Figure 54:** Beam stay clear $n_1$ for B1. These points represent the extracted minima along the shared beam pipe of the two proton beams for this particular parameter configuration (see red star in figure 53). The optimal inter beam distance $d$ $[\sigma_{\mathrm{B12}}]$ for each curve is marked here with a star (same values as in figure 50).

decided to not further consider it and to choose the $\beta^*_{\mathrm{B2}}$, where the maximal inter beam distance $d$ $[\sigma_{\mathrm{B12}}]$ value is reached (in section 6.4.2). This value is marked for each curve with a star. These are the positions in which $\beta^*_{\mathrm{B2}} = 10\,\mathrm{m}$. The beam stay clear values can then be summarized for all orbit configurations in figure 55.

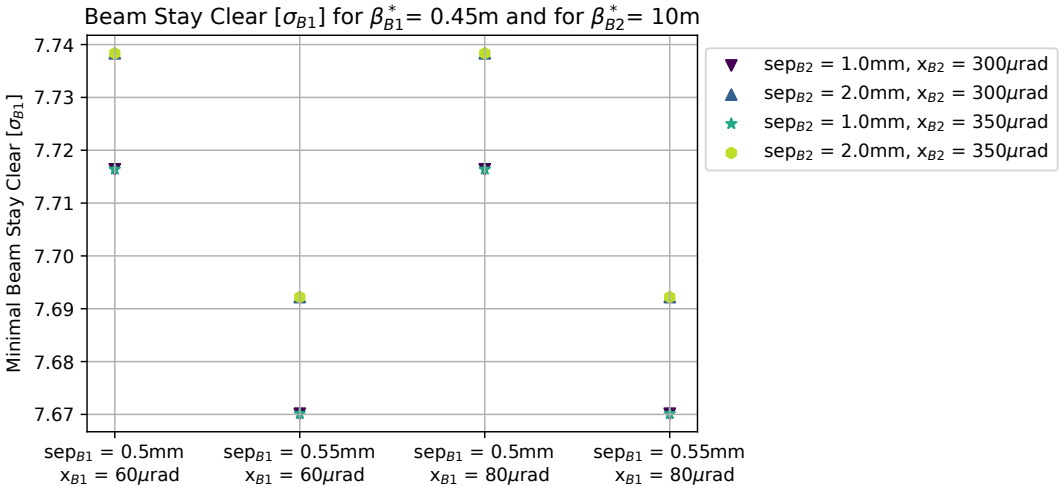


**Figure 55:** Plot of the minimal beam stay clear $n_1$ of B1 for $\beta^*_{\mathrm{B1}} = 0.45\mathrm{m}$ and $\beta^*_{\mathrm{B2}} = 10\mathrm{m}$. It shows the minimal beam stay clear $n_1$ for all the possible orbit configurations of the two proton beams.

In section 6.4.2 it was deduced that only four possible combinations were left to choose from (see figure 52) in order to maximize the inter beam distance. In figure 55 it can be seen that from these four values (right side of the plot), only the ones with an orbit configuration of $\mathrm{x_{B1}}$ = $80\,\mu\mathrm{rad}$ and $\mathrm{sep_{B1}}$ =$0.5\,\mathrm{mm}$ safely reach the necessary $7.7\,\sigma$ beam stay clear. It was decided to take the orbit configuration of B2, which reaches the higher $n_1$ (green octagon in figure 55). The optimal parameters for LHeC operation with the currently used NbTi triplet in IP2 are summarized in table 10. These parameters were chosen as they provide the best compromise between achieving a large inter beam separation and ensuring that the colliding proton beams still fits within the aperture margins.

| Beam | $\beta^*[\mathrm{mm}]$ | $\mathrm{sep}[\mathrm{mm}]$ | $\mathrm{x}[\mu\mathrm{rad}]$ |
|---|---|---|---|
| B1 | 0.45 | 0.5 | 80 |
| B2 | 10 | 2 | 350 |

**Table 10:** Parameters that were chosen as the optimal beam configuration for the proton beam separation in IR2.

These values, which are further summarized in table 13, achieve a beam stay clear of $7.7\,\sigma_{\mathrm{B1}}$ for B1 and $24.8\,\sigma_{\mathrm{B2}}$ for B2. An inter beam distance of $17\,\sigma_{\mathrm{B12}}$ and a luminosity of $1.1 \times 10^{33}\,\mathrm{cm^{-2}\,s^{-1}}$ is reached. This luminosity exceeds the anticipated peak luminosity expectation of LHeC in 2012, which was supposed to reach $1.0 \times 10^{33}\,\mathrm{cm^{-2}\,s^{-1}}$ [11] but is lower than the luminosity expected in an upgraded design for a stand alone experiment in the LHeC design report from 2021 [11]. In this report a luminosity of $0.5 \times 10^{34}\,\mathrm{cm^{-2}\,s^{-1}}$ was reached, for the same ERL configuration used in this thesis. This luminosity however was designed for a stand alone LHeC experiment, featuring different triplet magnets, and no second proton beam B2 passing through the same beam pipe. It was therefore possible to lower the $\beta^*$ value of B1 down to $0.1\,\mathrm{m}$. However, as stated in the report, the development of those triplet magnets would require significant R&D, whereas the triplet magnets used for the calculations in this section are already in use in IP2.

This is the first design for an LHeC interaction region that can run concurrently to the p-p operation of the HL-LHC, while still allowing ion-ion operation when e-p operation is switched off. Furthermore, the only necessary hardware changes for this machine layout include the recabling of the matching quadrupoles, as well as the installation of the electron magnets. The main limitation of this design is the available aperture for the colliding proton beam, limiting the $\beta^*_{\mathrm{B1}}$ that can be reached.

## 6.5 Inter Beam Distance Optimization for the LHeC IR Using a $Nb_3Sn$ Triplet

As was deduced in the previous section, the main limitation for the push in luminosity for the NbTi triplet was the available aperture. Therefore a second interaction region which uses magnets made of $Nb_3Sn$ was designed in the scope of this thesis. The inter beam distance optimization performed for the LHeC design with a NbTi triplet in section 6.4, has been repeated here for the LHeC design featuring a triplet made of $Nb_3Sn$.

The main advantage of these new triplet magnets is the increase in available beam aperture that they offer. Table 6 in section 5.3 summarizes the apertures of the different triplet magnets. The aperture radius in the triplets is increased from $70\,\mathrm{mm}$ to $150\,\mathrm{mm}$. Additionally, the shape of the beam screen changes from an elliptical to an octagonal form [86]. The different shapes of the beam screens can be seen in figure 56. These plots show the two proton beams in the second triplet magnet downstream of the IP (Q2), with a NbTi magnet on the top, and a $Nb_3Sn$ magnet on the bottom. These plots show a major difference in available aperture (see different scaling) and thus in the resulting $\beta^*_{\mathrm{B1}}$ that can be reached, as well as in the magnitude of the orbit bumps. With the new triplet magnets it was possible to push the luminosity from $1.1 \times 10^{33}\,\mathrm{cm^{-2}\,s^{-1}}$ to $2.5 \times 10^{33}\,\mathrm{cm^{-2}\,s^{-1}}$.

### 6.5.1 Defined Parameter Space

After installing the new triplet interaction region described in 5.3, the limits of this machine layout were investigated. It was possible to push $\beta^*_{\mathrm{B1}}$ down to a value of $0.2\,\mathrm{m}$, while still keeping the aperture margins, and assuring enough space between the two proton beams. In this chapter, a summary of the optimization performed for this $\beta^*_{\mathrm{B1}}$ in the new machine layout is presented. The parameter space is summarized in table 11. Compared to the parameters used for NbTi in table 9, the magnitude of the orbit bumps is increased for both proton beams.

In total, these parameters yield: $\mathrm{n}_{\beta^*_{\mathrm{B1}}} \cdot \mathrm{n}_{\beta^*_{\mathrm{B2}}} \cdot \mathrm{n}_{\mathrm{sep_{B1}}} \cdot \mathrm{n}_{\mathrm{sep_{B2}}} \cdot \mathrm{n}_{\mathrm{x_{B1}}} \cdot \mathrm{n}_{\mathrm{x_{B2}}} = 1 \cdot 26 \cdot 2 \cdot 2 \cdot 2 \cdot 2 = 416$ different combinations.

| Beam | $\beta^*\,[\mathrm{m}]$ | $\mathrm{sep}\,[\mathrm{mm}]$ | $\mathrm{x}\,[\mu\mathrm{rad}]$ |
|---|---|---|---|
| B1 | 0.2 | 2.5, 3.0 | 150, 200 |
| B2 | 14 to 40 in steps of 1 | 3.5, 4.0 | 250, 300 |

**Table 11:** Parameters that were scanned for the optimal beam configuration for the proton beam separation in IR2 for a $\beta^*_{\mathrm{B1}}$ of $0.2\,\mathrm{m}$ for a triplet magnet technology using $Nb_3Sn$.

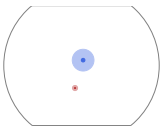

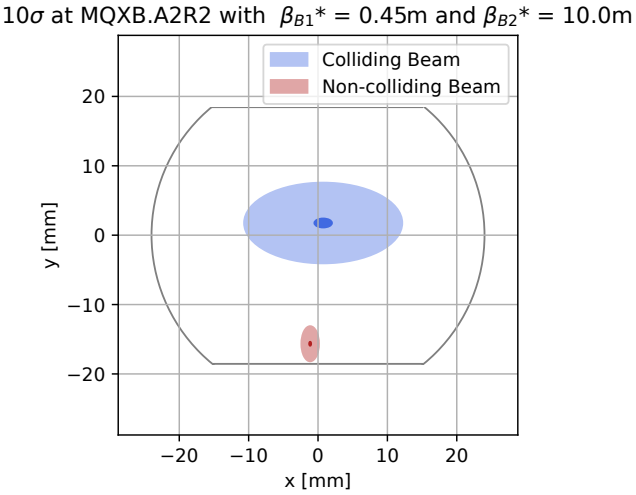


**(a)** Elliptical beam screen used currently in IR2 together with triplet magnets made of NbTi.

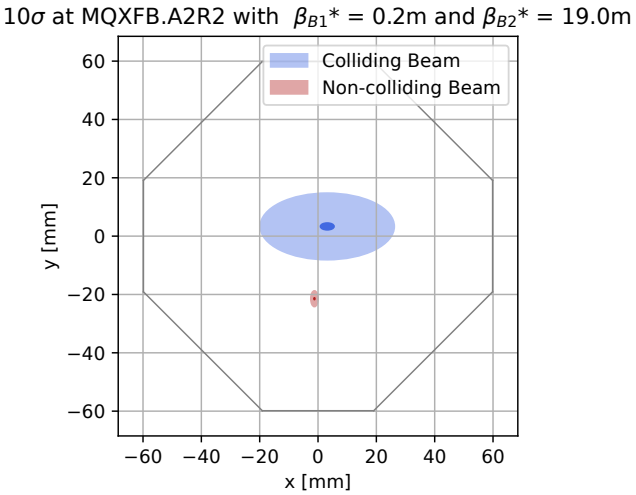


**(b)** Octagonal beam screen designed for the HL-LHC upgrade magnets made of $Nb_3Sn$. Dimensions from [87].

**Figure 56:** Display of different beam screens depending on the magnet technology. On the top for the currently used NbTi triplet magnets and on the bottom for the $Nb_3Sn$ triplets which will be installed in the the HL-LHC upgrade. Dark blue shading represents $1\ \sigma_{\mathrm{B1}}$, and light blue shading represents $10\ \sigma_{\mathrm{B1}}$. In dark red $1\ \sigma_{\mathrm{B2}}$ is represented and in light red $10\ \sigma_{\mathrm{B1}}$ are shown. Note that the axes are scaled differently for the two beam screens.

### 6.5.2 Optimal Inter Beam Distance

A plot of the inter beam distance can be seen in figure 57 for the chosen parameter set. In this plot it can be seen that when measuring $d\,[\sigma_{\mathrm{B1}}]$ and $d\,[\sigma_{\mathrm{B12}}]$, the inter beam distance reaches a minimum downstream of the IP, as the orbit bumps close, and B1 is still increased in size. At the IP $d\,[\sigma_{\mathrm{B1}}]$ reaches a value above $600\,\sigma$ which is not shown in this plot for scaling reasons. $d\,[\sigma_{\mathrm{B2}}]$ reaches a minimum upstream of the IP, which still exceeds the required inter beam distance. In this optimization, as for the one performed with NbTi, $d\,[\sigma_{\mathrm{B12}}]$ is optimized while considering the $d\,[\sigma_{\mathrm{B2}}]$ for the optics of B2. An analysis of $d\,[\sigma_{\mathrm{B1}}]$ can be found in the appendix A.3.3.

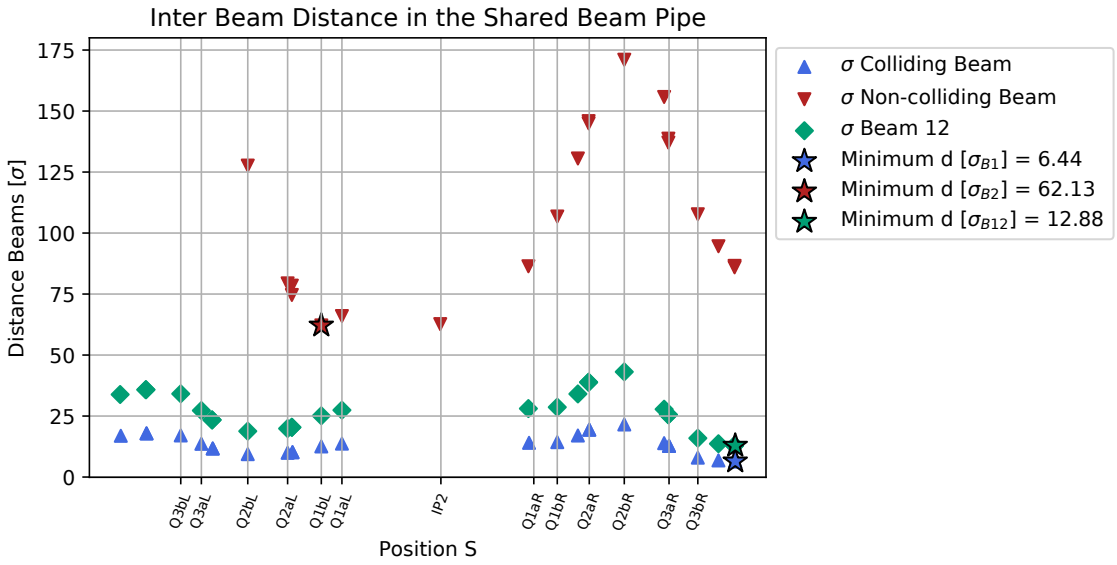


**Figure 57:** Inter beam distance between the two proton beams in their shared beam pipe. In blue in units of $\sigma_{\mathrm{B1}}$ and in red in units of $\sigma_{\mathrm{B2}}$. In green in units of the mean beam size $\sigma_{\mathrm{B12}}$. The stars mark the corresponding minimums for each unit.

As was the case for the triplet design based on NbTi, The inter beam distance in units of the average beam size $d\ [\sigma_{\mathrm{B12}}]$ does not depend on the optics of B2 (see appendix A.3). In figure 58, $d\ [\sigma_{\mathrm{B2}}]$ is plotted as a function of $\beta^*_{\mathrm{B2}}$ for the best chosen configuration of B1, for all orbit configurations of B2.

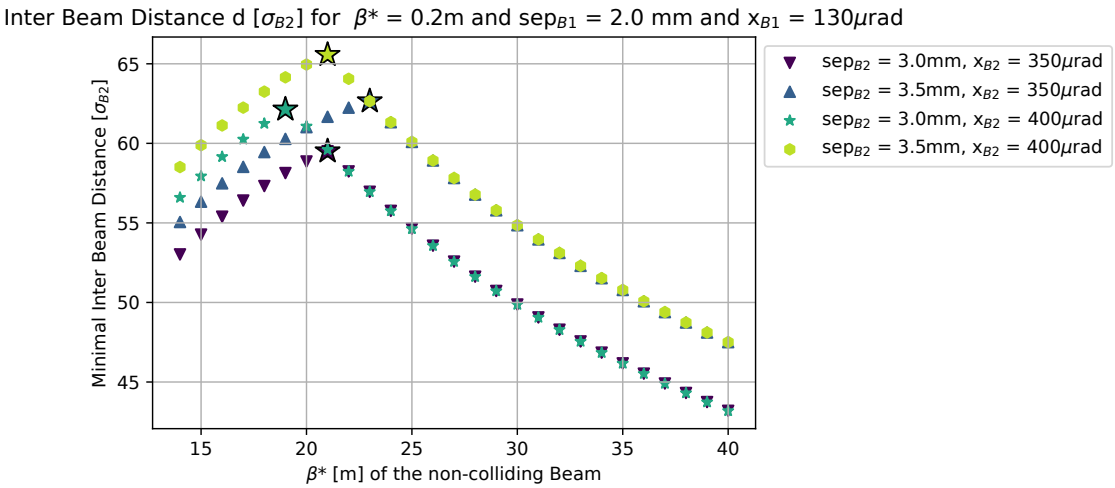


**Figure 58:** Inter beam distance $d$ between the two proton beams in their shared beam pipe for $\beta^*_{\mathrm{B1}} = 0.2\,\mathrm{m}$. It is plotted for the chosen orbit configuration of B1 in table 9 as a function of $\beta^*_{\mathrm{B2}}$ in units of $\sigma_{\mathrm{B2}}$. Four different curves are shown, for four different orbit configurations of B2. The stars mark the position of the chosen $\beta^*_{B2}$.

Figure 58 shows that $d\ [\sigma_{\mathrm{B2}}]$ varies greatly depending on the chosen $\beta^*_{\mathrm{B2}}$ and a clear optimum can be defined for each curve. This is due to the position of the minimal $d\ [\sigma_{\mathrm{B2}}]$ being located in the inner triplet for lower $\beta^*_{\mathrm{B2}}$ values and then shifting to the position of the IP for higher $\beta^*_{\mathrm{B2}}$ (see figures49 and figure 57). It then proceeds to fall of sharply. This plot shows that $d\ [\sigma_{\mathrm{B2}}]$ always exceeds $40\,\sigma$.

In these curves the minimal values of the inter beam distance have been marked with stars. It can be seen that differently to the LHeC design with a NbTi triplet, the maxima are reached here for higher $\beta^*_{\mathrm{B2}}$ values. For each orbit configuration, $\beta^*_{\mathrm{B2}}$ is chosen so that $d\ [\sigma_{\mathrm{B2}}]$ reaches the highest value. The optics of the beams are thus fixed and only the orbit configurations still need to be chosen. A summary of the minimal value of $d\ [\sigma_{\mathrm{B12}}]$ can be seen for each orbit configuration in figure 59.

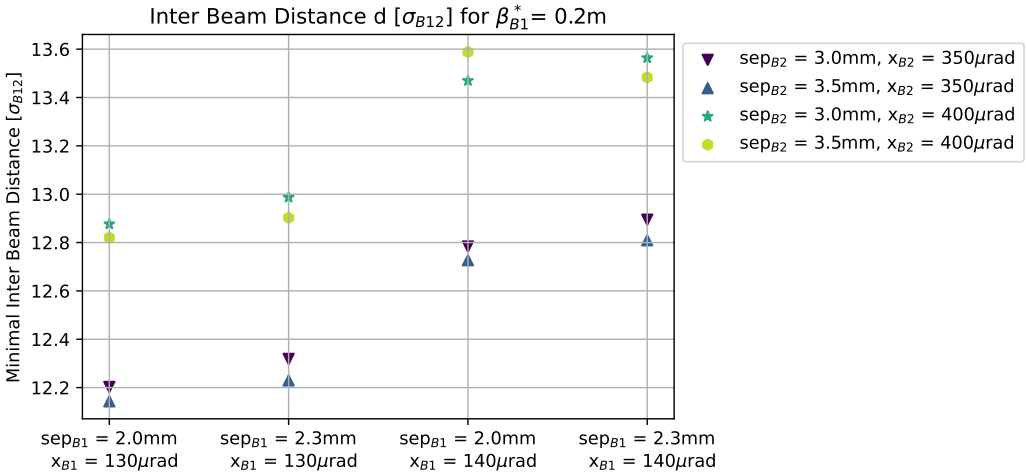


**Figure 59:** Inter beam distance $d$ $[\sigma_{\mathrm{B12}}]$ between the two proton beams in their shared beam pipe for $\beta^*_{\mathrm{B1}} = 0.2\,\mathrm{m}$. Each point represents the minimal inter beam distance for this particular orbit configuration. Each color/shape of point represents a different orbit configuration of B2. The x-axis indicates the orbit configurations of B1. The $\beta^*_{\mathrm{B2}}$ is set to a value, which reaches the highest inter beam distance for this particular orbit configuration (stars in figure 81).

From this plot, it can be seen that only four combinations do not meet the necessary $12.5\,\sigma_{\mathrm{B12}}$. In order to decide on an orbit configuration among the remaining ones, the beam stay clear $n_1$ was additionally evaluated.

### 6.5.3 Beam Stay Clear

The beam stay clear $n_1$ is calculated for each proton beam in their shared beam pipe for every single configuration of table 11. In figure 60 the beam stay clear is shown for the optimal parameter set.

This plot shows that with the new triplet it is possible to reach a beam stay clear $n_1$ of $10\,\sigma$ for B1 for $\beta^*_{\mathrm{B1}} = 0.2\,\mathrm{m}$, even for separation and crossing bumps with high values. For B1, the lowest value is reached in the triplet (Q3bR), where the beam reaches a great size, and the orbit bumps are still pushing it close to the aperture. For B2, the lowest $n_1$ is reached in the first triplet magnet downstream of the IP (Q1aR). It does however exceed $70\,\sigma$ and the beam stay clear of B2 is not investigated further in this section, as B2 never gets dangerously close to the aperture. An analysis of the beam stay clear of B2 can be found in the appendix A.3.3.

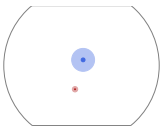

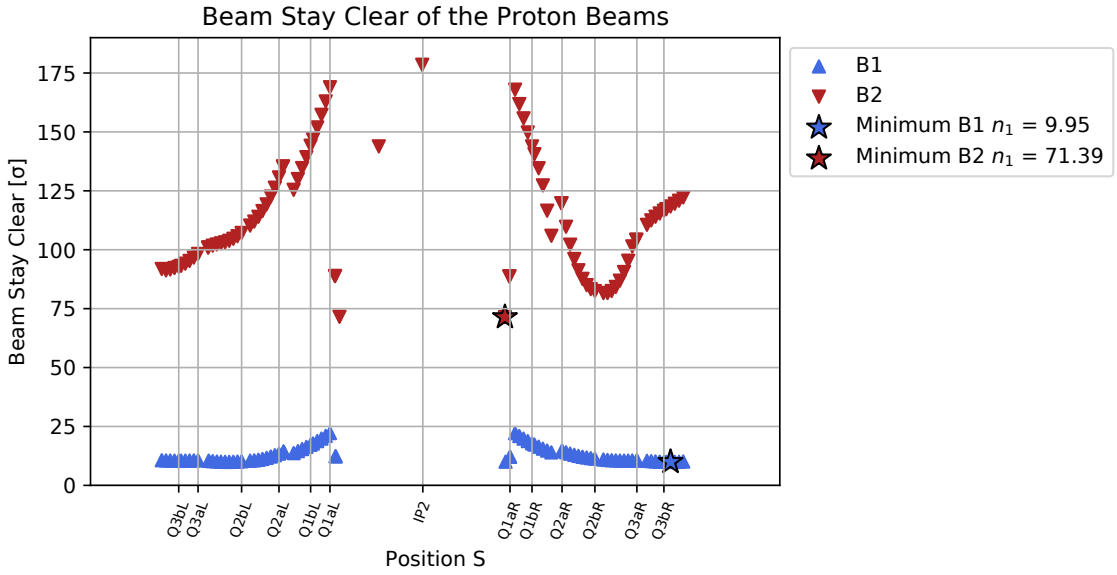


**Figure 60:** Beam stay clear $n_1$ values in units of beam size $\sigma$ for the two proton beams in their shared interaction region. The stars mark the minimal $n_1$ value for each beam. Here an example is shown for the chosen configuration of table 11.

As the optics of B2 were set by choosing the $\beta^*_{\mathrm{B2}}$, which maximized the inter beam distance $d[\sigma_{\mathrm{B2}}]$, the $n_1$ values can be summarized for all orbit configurations in figure 61.

In figure 61 it can be seen that for all orbit configurations a beam stay clear of $9.4\,\sigma$ can be reached. Comparing this plot with figure 59, which represents a summary of the inter beam distances, the parameter configuration in table 12 is chosen which give the highest beam stay clear, together with sufficient inter beam distance (first turquoise star in figure 61).

| Beam | $\beta^*$[mm] | sep[mm] | x[$\mu$rad] |
|---|---|---|---|
| B1 | 0.2 | 2 | 130 |
| B2 | 19 | 3 | 400 |

**Table 12:** Parameters that were chosen as the optimal beam configuration for the proton beam separation in IR2 with triplets using $Nb_3Sn$ magnet technology.

With these values, a beam stay clear of $9.9\,\sigma_{\mathrm{B1}}$ is assured for B1, while for B2 it reaches $71\,\sigma_{\mathrm{B2}}$. An inter beam distance of $12.9\,\sigma_{\mathrm{B12}}$ and a luminosity of $2.5 \times 10^{33}\,\mathrm{cm}^{-2}\,\mathrm{s}^{-1}$ can be reached. This interaction region can satisfy the desired inter beam distance in order to minimize the beam-beam interactions, as well as keep

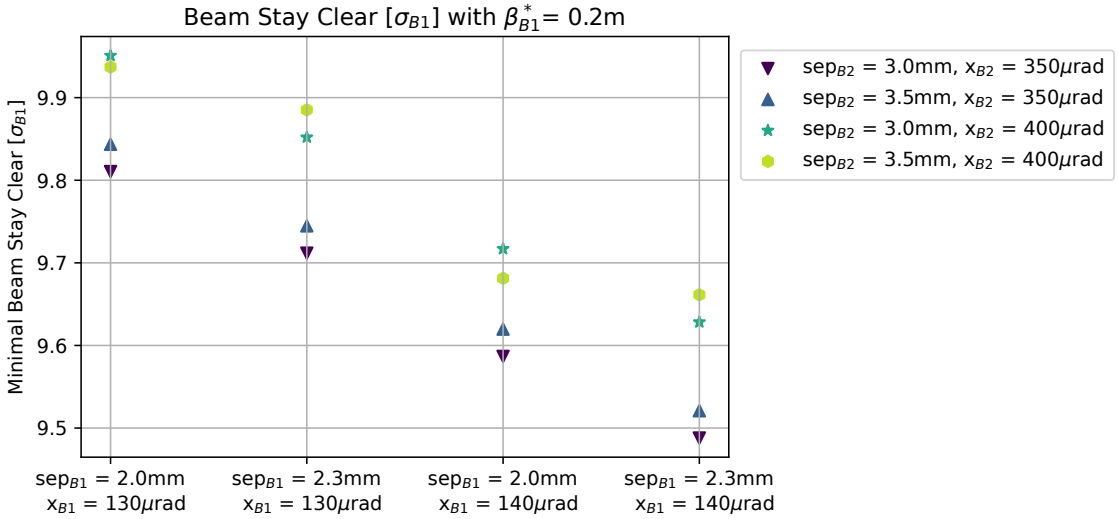


**Figure 61:** Summary of the minimal beam stay clear $n_1$ of B1 for each orbit configuration. The optics in this plot show $\beta^*_{\mathrm{B1}} = 0.2\mathrm{m}$ and the optimal $\beta^*_{\mathrm{B2}}$ for each configuration, maximizing $d[\sigma_{\mathrm{B2}}]$. Each color/shape represents a different orbit configuration of B2. The x-axis represents different orbit configurations for B1.

a safe margin to the available aperture.

## 6.6 Summary

The proposed interaction region designs allow flexible operation: they can run e–p collisions concurrently with p–p collisions in the remaining interaction points, or alternatively, they can operate in ion–ion or p–p mode when LHeC operation is switched off.

In Table 13, the results of the optimization of the distance between the two proton beams are presented.

These results show that for high luminosity high energy e-p collisions it is necessary to invest in $Nb_3Sn$ magnets. This new interaction region achieves twice the luminosity obtained with the NbTi triplet. The resulting luminosity even exceeds the initial peak luminosity target of the LHeC from 2012, which anticipated $1.0 \times 10^{33}\,\mathrm{cm}^{-2}\,\mathrm{s}^{-1}$ [11]. Compared to the stand-alone LHeC configuration, the luminosity obtained here is smaller by a factor of two [11]. It is important to distinguish this from the stand-alone expectation (see section 8).

| LHeC Design | d $[\sigma_{\mathrm{B12}}]$ | $\beta^*_{\mathrm{B1}}[m]$ | $\beta^*_{\mathrm{B2}}[m]$ | Luminosity $[\mathrm{cm}^{-2}\mathrm{s}^{-1}]$ | $\mathrm{n}_1$ B1$[\sigma_{\mathrm{B1}}]$ | $\mathrm{n}_1$ B2$[\sigma_{\mathrm{B2}}]$ |
|---|---|---|---|---|---|---|
| NbTi triplet | 17.5 | 0.45 | 10 | $1.1 \times 10^{33}$ | 7.7 | 25 |
| $Nb_3Sn$ triplet | 12.9 | 0.2 | 19 | $2.5 \times 10^{33}$ | 10 | 71 |

**Table 13:** Comparison of the LHeC interaction design with a triplet using $Nb_3Sn$ or NbTi technology. $d$ $[\sigma_{\mathrm{B12}}]$ defines the minimal distance achieved between the two proton beams in units of their average beam size. The $n_1$ value denotes the minimal distance of the corresponding proton beam to the beam screen in units of the beam size.

The main limitation of these designs is the available aperture when focusing proton B1.

It should be noted that in the scope of performing these calculations, the aperture limits in the injection collimators, as well as the ALICE spectrometer were not considered. For the designs investigated in this thesis, the chosen interaction point would be IR2, which is also the region of LHC where proton beam B1 is injected. This poses extra constraints on this interaction region and makes it less flexible than for example IR1 or IR5. These calculations serve as proof of principle demonstrations for concurrent operation of LHeC and HL-LHC, while still allowing ion-ion collisions in the LHeC interaction region. In order to fully define this interaction region, it would be necessary to research injection collimators, which can house a high luminosity proton beam. Additionally, it would be necessary to verify if this proton beam can fit safely into the ALICE spectrometer.

# 7 Dynamic Aperture Calculations for the LHeC Interaction Region

This chapter describes the procedure, as well as the results of the dynamic aperture studies performed for one of the designed LHeC interaction regions. These calculations have been performed for the colliding proton beam B1 for the LHeC interaction region using a triplet based on niobium titanium (NbTi). Owing to time constraints, the analysis was restricted to this configuration.

## 7.1 Preparation for the Tracking Simulations

The **dynamic aperture** is defined as the largest initial transverse amplitude in phase space for which a particle remains stably confined over a specified number of turns, in the presence of nonlinear fields and machine imperfections [88].

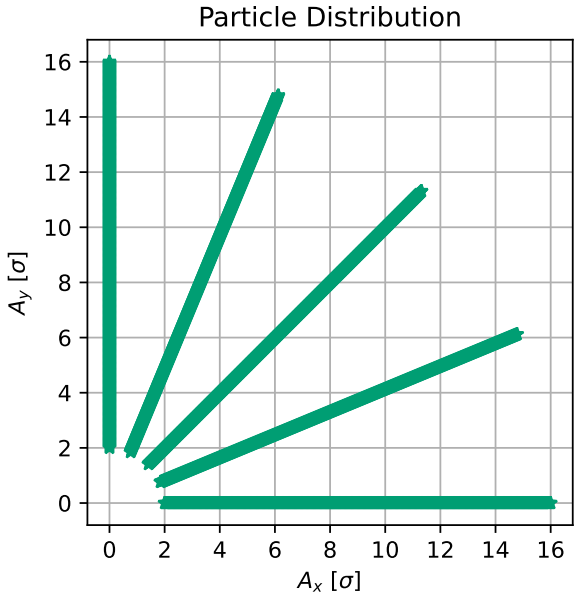


**Figure 62:** Initial particle distribution before performing the tracking simulations. The x- and y- axis indicate the amplitude of the corresponding transversal displacement expressed in beam sizes $\sigma$.

The particles were initialized on a polar grid in the transverse plane before being tracked. The particles were distributed with amplitudes $A_x, y$ ranging from $2\,\sigma$ to

$16\,\sigma$. These amplitudes $A_{x,y}$ were applied to five different polar angles. This can be seen in figure 62.

Since the tracking calculations were only performed for the colliding proton beam B1, this amplitude $A_{x,y}[\sigma]$ was defined as such:

$$A_{x,y}[\sigma] = \frac{A_{x,y}[\mathrm{mm}]}{\sigma_{B_1[\mathrm{mm}]}}. \tag{71}$$

In equation 71, $\sigma_{B1}$ represents the beam size of B1 and $A_{x,y}[\mathrm{mm}]$ represents the transverse displacement in $\mathrm{mm}$ . The particles between $0\,\sigma$ and $2\,\sigma$ were not considered in the tracking simulations, as it was assumed that they survived in either case. In these tracking calculation only the impact of the sextupoles, as well as magnetic field errors were investigated. Higher order magnetic fields (octupoles, dodecapoles) were not considered. An overview of the files used to prepare the lattice for tracking can be found in the appendix B.

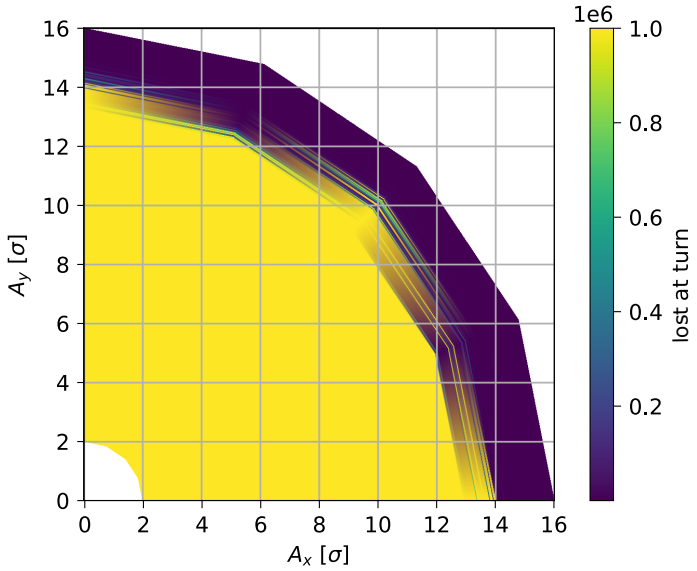


**Figure 63:** Tracking calculation performed for HL-LHC without any modifications over one million turns. Here collision optics were tracked with $\beta^*_{\mathrm{IP1/5}}$= 0.15 m, $\beta^*_{\mathrm{IP2}}$= 10 m and $\beta^*_{\mathrm{IP8}}$= 1.5 m. The x- and y- axis indicate the amplitude of the corresponding transversal displacement expressed in beam sizes $\sigma$. The initialized particles can be seen in figure 62. The color code indicates how many turns the particles performed.

Before studying the dynamic aperture of any of the designed optics of LHeC, the initialized particles are tracked in the collision optics of the HL-LHC lattice ([74])

without applying any modifications and without adding beam-beam effects. In these optics $\beta^*_{\mathrm{IP1/5}}$=0.15 m, $\beta^*_{\mathrm{IP2}}$=10 m and $\beta^*_{\mathrm{IP8}}$=1.5 m. The result can be seen in figure 63.

For HL-LHC, the minimal dynamic aperture for one proton beam, without considering beam-beam effects, over one million turns amounts to $12.96\,\sigma$ for particles who are initialized on the polar grid at an angle of $\theta = 22.5°$. In the following tracking studies, modifications were applied exclusively in IR2.

## 7.2 Dynamic Aperture Studies of the Colliding Proton Beam

The tracking calculations were performed for the LHeC design using a NbTi triplet for the proton beam which collides with the electron beam: B1. The dynamic aperture of the spectator proton beam B2 was not investigated in the scope of this PhD. It is assumed that the losses are less significant for this beam, as the margin to the available aperture is significantly larger than for B1. Additionally, in the chromatic correction, the sextupoles did not need to be increased in their strength, as was the case for the aggressively focused B1.

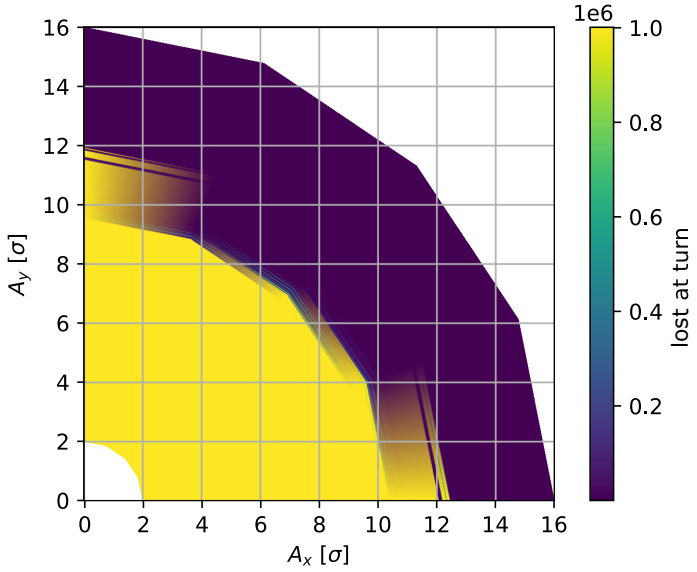


**Figure 64:** Tracking calculation performed for $\beta^*_{\mathrm{IP2}}$= 0.45 m without the additional electron magnets. The particles were tracked over one million turns. The x- and y- axis indicate the amplitude of the corresponding transversal displacement expressed in beam sizes $\sigma$. The initialized particles can be seen in figure 62. The color code indicates how many turns the particles performed.

In section 6 it was shown, that the lowest $\beta^*$ which could be realized for B1 with this design was $0.45\,\mathrm{cm}$. These optics were first investigated by just focusing B1 down to this value, and not adding the electron insertion to the lattice yet. The result for this tracking scenario can be seen in figure 64.

The determined dynamic aperture for these optics were $9.58\,\sigma$ at an initiation angle $\theta$ of $67.5°$. It can be seen, that the dynamic aperture decreases in comparison to the one defined by running the tracking simulations without focusing B1 in this interaction region in figure 63. One of the major reasons for these losses is, that the beam stay clear for these optics amounts to $7.7\,\sigma$ at its lowest point (see section 6.4). As a result, many particles with high amplitudes are lost on the machine aperture.

As a next step, the electron insertion was inserted into the HL-LHC lattice and the tracking calculations were repeated. This can be seen in figure 65.

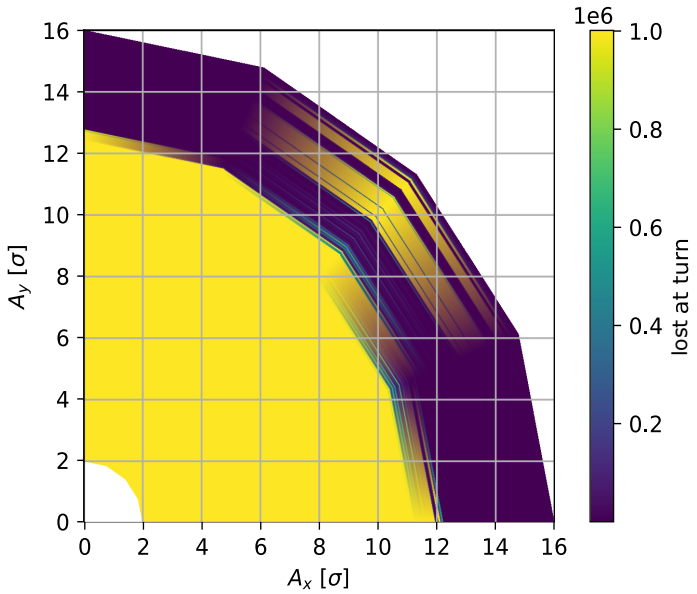


**Figure 65:** Tracking calculation performed for $\beta^*_{\mathrm{IP2}}$= $0.45\,\mathrm{m}$ with the additional electron magnets inserted into the lattice. The x- and y- axis indicate the amplitude of the corresponding transversal displacement expressed in beam sizes $\sigma$. The particles were tracked over one million turns. The initialized particles can be seen in figure 62. The color code indicates how many turns the particles performed.

The minimal dynamic aperture increased to $11.2\,\sigma$ at an initiation angle $\theta$ of $22.5\,\mathrm{rad}$. This could be explained with a small focusing effect of the electron quadrupoles on proton B1 but would need further research to be clarified.

### 7.2.1 Beam-beam Impact of the Electron Beam on the Colliding Proton Beam

In this study, mutual beam–beam effects between the proton beams were not considered, as it is assumed that the optimized separation scheme, providing a beam separation of $17.5\,\sigma$ (see section 6) in IR2, is sufficient. Only the impact of the electron beam on the colliding proton beam B1 was investigated. As the electron beam collides with B1, it exerts a short-range beam-beam force on the proton beam. To investigate this effect, a beam-beam element was installed at the interaction point in the lattice. This element reproduces the nonlinear kick that the proton beam would experience from the electron beam, modeled as a magnetic multipole field. The parameters used to simulate the beam-beam element in the tracking simulation are summarized in table 14.

**Table 14:** Parameters used to simulate the beam-beam effect of the electron beam on the colliding proton beam B1.

| Parameter | Value |
|---|---|
| RMS Bunch Length $\sigma_z$ | $0.06\,\mathrm{cm}$ [32] |
| Bunch Number $n_b$ | 1188 [32] |
| Beam Current | $20\,\mathrm{mA}$ [32] |
| Bunch Charge | $0.5\,\mathrm{nC}$ [32] |
| Normalized Emittance | $30\,\mu\mathrm{m\,rad}$ [32] |
| Amplitude function at the IP $\beta^*$ | $49.17\,\mathrm{cm}$ |
| Beam-beam Parameter $\xi_{x,y}$ | 0.047 |

The effect of the nonlinear kick introduced by the beam-beam element can be seen in figure 66. It shows the $7\,\mathrm{TeV}$ protons initialized at a transversal position $x$ between $-0.01\,\mathrm{mm}$ and $0.01\,\mathrm{mm}$. These particles had no initial transversal momentum $p_x$. They were subsequently tracked for two cases: without the beam-beam effect and with the applied beam-beam effect.

Figure 66 shows how the multipole field introduced by the beam-beam element impacts the transversal momentum $p_x$. The particles experience a linear force in the regime around $x$=0, similar to the one experienced by a quadrupole field. As $|x|$ increases, this force becomes non linear.

The particles in the colliding proton beam B1 are subsequently tracked again over one million turns in the LHeC lattice with $\beta^*$ =0.45 m. The result is plotted in figure 67.

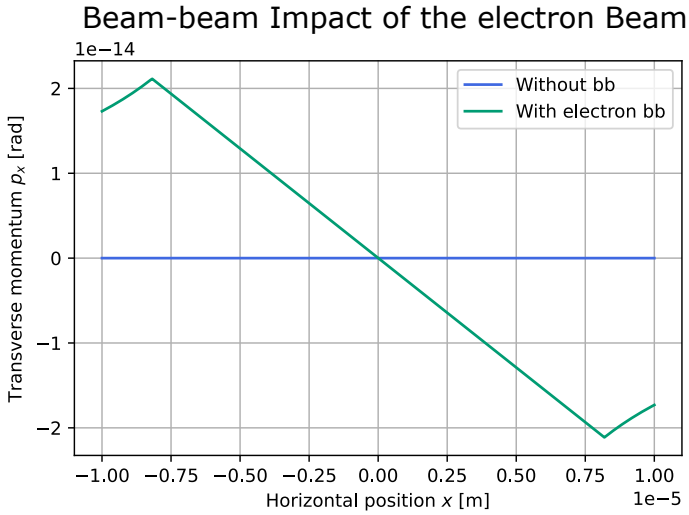


**Figure 66:** Impact of the electron beam on the transverse momentum $p_x$ of the colliding proton beam B1. The proton particles were tracked once without the beam-beam effect of the electron beam (blue) and once after applying the beam-beam effect (green).

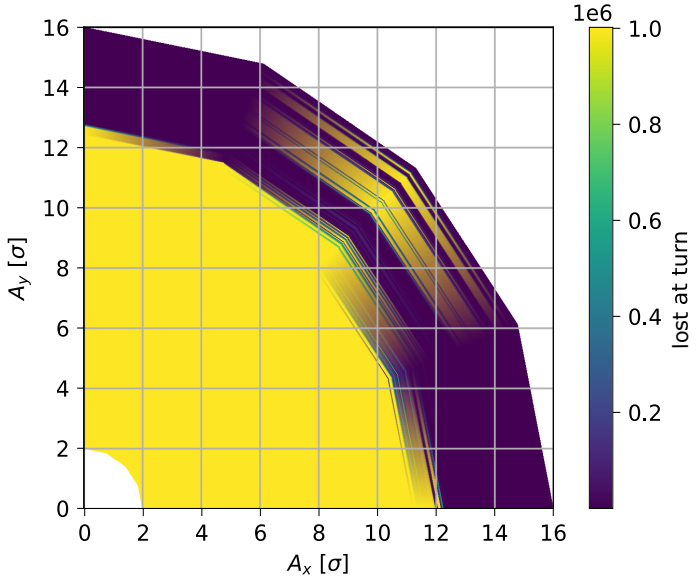


**Figure 67:** Tracking calculation performed over one million turns for the colliding proton beam B1 with $\beta^*$= 0.45 m. The short range beam-beam effect of the electron beam was simulated at the IP. The x- and y- axis indicate the amplitude of the corresponding transversal displacement expressed in beam sizes $\sigma$. The initialized particles can be seen in figure 62. The color code indicates how many turns the particles performed.

The dynamic aperture increases very slightly from $11.2\,\sigma$ to $11.24\,\sigma$ at an angle $\theta$ of $22.5°$. It can also be seen that more particles are recovered at higher amplitudes. This could be due to the electron beam's opposite charge slightly focusing the proton beam. However, the change is so small that no firm conclusion can be drawn regarding its significance. The electron beam-beam effect on the colliding proton beam B1 is negligible compared to the loss in dynamic aperture caused by the small beam stay clear and possibly by the chromatic effect induced by the sextupoles.

In the original collision optics the amplitude function amounts to $\beta^*$ =10 m. By focusing B1 more aggressively in this IP, the strength of the quadrupoles is increased. As a result, the chromaticity increases. This can be seen in equation 36, which is repeated here for convenience:

$$\xi = \frac{\Delta Q}{\Delta p/p} = \frac{1}{4\pi} \oint k(s)\beta(s)\mathrm{ds}. \tag{72}$$

In this equation $\xi$ represents the chromaticity (not to be confused with the beam-beam parameter), $\Delta Q$ the tune shift, $k(s)$ the quadrupole strength at a location $s$ and $\beta(s)$ the corresponding amplitude function.

The chromaticity is particularly increased in IR2, as the amplitude function of B1 is increased here and the quadrupoles are set to higher currents. As the chromaticity was corrected by increasing the strength of the sextupoles, the loss in dynamic aperture could also be caused by particles with high amplitudes being deflected by the sextupoles.

These results show that the dynamic aperture is primarily limited by the mechanical aperture of the NbTi triplet. The beam–beam effect of the electron beam on the proton beam is negligible and may even lead to a slight increase in the dynamic aperture.

## 7.3 Dynamic Aperture Studies of the Colliding Proton Beam without the Spectating Proton Beam

In the previous section the dynamic aperture of HL-HLC was studied for a value of $\beta^*_{\mathrm{IP2}}$ = 0.45 m. This value was chosen in section 6, as it offers the highest luminosity for an e-p interaction region that can host either e-h or h-h interactions and run concurrently to other h-h interactions in the other interaction points.

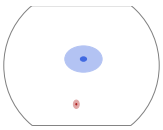

It is possible to further increase the e-p luminosity by switching off the spectator proton beam, as well as the orbit bumps for B1. This gain in aperture makes it possible to push the amplitude function of B1 down to $\beta^*_{\mathrm{IP2}}$=0.35 m. In figure 68 the simulated tracking data for the proton beam B1 for these optics is shown.

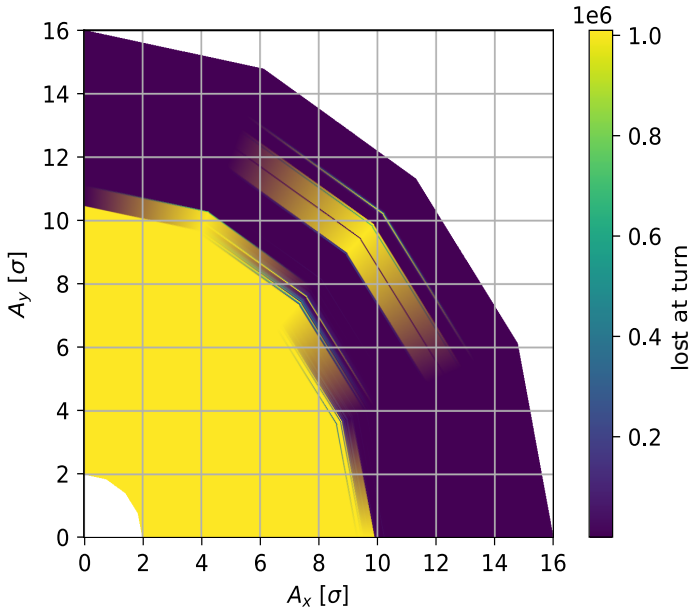


**Figure 68:** Tracking calculation performed for $\beta^*_{\mathrm{IP2}}$= 0.35 m with the additional electron magnets inserted into the lattice. The particles were tracked over one million turns. The x- and y- axis indicate the amplitude of the corresponding transversal displacement expressed in beam sizes $\sigma$. The initialized particles can be seen in figure 62. The color code indicates how many turns the particles performed.

The dynamical aperture that was derived with these calculations amounts to $9.3\,\sigma$ at an initiation angle $\theta$ of $22.5°$. The reduction in dynamic aperture is likely due to the limited beam stay-clear ($n_1$) and the increased sextupole strengths. It would be interesting to repeat these dynamical aperture studies for the interaction region with the $Nb_3Sn$ triplet to determine whether the observed reduction in aperture is primarily caused by mechanical constraints or by the sextupoles.

In the betatron cleaning insertion in IR7, the primary collimators will be positioned at $8.5\,\sigma$ for collision energies of 7 TeV during HL-LHC operation [89]. The dynamic aperture studies performed for the optics of the colliding proton beam B1 reach values well above these collimator settings. It is therefore assumed, that B1 would not be destroyed by the available aperture. It would however be necessary to perform an extensive proton beam-beam study to investigate if the designed proton beam separation is sufficient. For beam–beam simulations performed for proton–proton collision optics in the HL-LHC, the dynamic aperture

reaches values of only about $6.5\,\sigma$ [90], showing how detrimental the effects of these high intensity beams are. Additionally, higher-order magnetic fields would need to be investigated to finalize this design for LHeC.

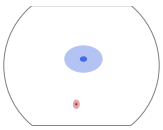

# 8 Luminosity Expectation for LHeC

This chapter discusses how the luminosity of LHeC varies depending on the machine design, as well as on the specific machine operation. The concept of luminosity has been introduced in section 2.2 and is briefly reviewed here.

The *geometric luminosity* $L_{\text{geo}}$ of an e-p collider is given by [11]:

$$L_{\text{geo}} = \gamma_p \frac{n_p \cdot N_e \cdot N_p \cdot f_{rev}}{4 \cdot \pi \cdot \beta_p^* \cdot \varepsilon_{n_p}}. \tag{73}$$

In this equation, $n_p$ describes the proton bunch number, $N_{e,p}$ represent the amount of particles per bunch for the corresponding beam. $f_{rev}$ represents the proton revolution frequency, $\beta_p^*$ the amplitude function of the protons at the interaction point and $\varepsilon_{n_p}$ the normalized emittance of the proton beam. At the interaction point, the electron beam has the same transverse size as the proton beam. The *total luminosity* $L_{\text{tot}}$ takes into account additional effects which modify the luminosity [34].

$$L_{\text{tot}} = L_{\text{geo}} \cdot G \cdot B \cdot F. \tag{74}$$

In this equation $G$ represent the geometric reduction factor. It includes the geometric effects, which reduce the overlap of the bunches: the crossing angle, as well as the hourglass effect. Usually, the crossing angle between the two colliding beams diminishes the luminosity. In the case of LHeC however, the particles collide head on and no crossing angle needs to be considered. As a result $G$ only considers the hourglass effect. $F$ describes the filling factor, since a certain space is left in the bunch train. The factor $B$ represents the beam-beam correction factor [11]. This one is greater than $1$ in the case of LHeC, as the rigid proton beam focuses the flexible electron beam by pinching it and therefore increasing the overlap of the bunches in the collision.

In the case of LHeC, the geometric, filling and beam-beam correction factor are estimated as $G \approx 0.9$, $F \approx 0.8$ and $B \approx 1.3$ [11]. The product of these factors is $0.936$ but in previous LHeC luminosity estimates it has been approximated as unity for simplicity [11, 32]. For consistency, the same approximation was adopted in this thesis.

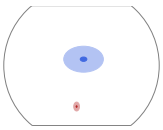

In order to calculate the luminosity for the layout of LHeC designed in this PhD, the following parameters were chosen:

| Parameter | Electron Beam | Proton Beam | Unit |
|---|---|---|---|
| Beam Energy | 50 [32] | 7000 [57] | GeV |
| Lorentz Factor $\gamma$ | 97 847.36 | 7460 | - |
| Normalized Emittance $\varepsilon_n$ | 30 [32] | 2.5 [84] | µm rad |
| $N$ | $3.1 \times 10^9$[11] | $2.2 \times 10^{11}$ | - |
| $n_b$ | 2760 [91] | 1188[32] | - |
| $f_{rev}$ | 112 455 [91] | - | Hz |

The parameters for the energy recovery linac are extracted from the LHeC conceptual design report [11]. At the moment these parameters are still subject to a feasibility study and they might still be changed. The PERLE (Powerful Energy Recovery Linal for Experiments) facility in Orsay, France is designed to test and demonstrate multi-turn ERL technology, which could be used for the LHeC. At present, PERLE aims to achieve multi-turn ERL operation by 2032 [92].

As one can deduce from equation 73, the only parameter that can be influenced with the proton optics is the size of the amplitude function at the IP: $\beta_p^*$.

One of the factors in the design of a collider directly impacts the reachable $\beta^*$. This is the length of the drift space between the last focusing triplet quadrupole and the IP: $L^*$.

As the particles pass through a symmetry point $\beta^*$ after a drift space of length $l$, their amplitude function at this distance $l$ is of the size $\beta(l)$ [30]:

$$\beta(l) = \beta^* + \frac{l^2}{\beta^*}. \tag{75}$$

This equation is a result of *Liouvilles' Theorem*. As the beam size is reduced at the interaction point by decreasing $\beta^*$, the amplitude increases at a distance $l$ from the interaction point. It is possible to minimize this increase in the amplitude function by calculating its derivative and setting it to zero:

$$\frac{\mathrm{d}\beta(l)}{\mathrm{d}\beta^*} = 1 - \frac{l^2}{\beta^{*2}} \stackrel{!}{=} 0. \tag{76}$$

This then results in:

$$\beta^* = l. \tag{77}$$

This means, that the expansion of the beta function is smallest for $\beta^* = l$. From equation 77 one can deduce that the increase in the amplitude function is smaller, for small values of $L^*$. A smaller $L^*$ therefore requires less aperture in the triplet magnets to reach a low $\beta^*$.

For the protons in HL-LHC, this drift distance between the last focusing quadrupole and the IP amounts to $22.965\,\mathrm{m}$ [58], as the detector needs to fit in between. In ATLAS and CMS, the amplitude function at the IP is reduced to $0.15\,\mathrm{m}$. As a result, the amplitude function before the IP reaches values above $21\,000\,\mathrm{m}$ (see figure 21).

In this section, the interaction regions developed in this PhD are compared with the LHeC stand-alone configuration. An overview of these operational modes is given in Table 15.

| **LHeC IR Design** | **ATLAS** | **LHeC/ALICE** | **CMS** | **LHCb** |
|---|---|---|---|---|
| LHeC alternate to p-p | p-p | e-p **or** p-p | p-p | p-p |
| LHeC stand alone | p-p | e-p **only** | p-p | p-p |

**Table 15:** Different operational scenarios for LHeC. *LHeC alternate to p-p* represents the design created in this thesis, which allows for either operation: e-p (LHeC) or p-p (ALICE). LHeC as a *stand alone* experiment represents an LHeC interaction region solely designed for e-p interactions. Note that all interactions labeled as p-p could also run as ion-ion experiments.

## 8.1 LHeC in Alternating Operation with p-p/ion-ion Operation

The interaction region designed in this PhD makes it possible to run either kind of experiment in IP2: e-p/e-ion (LHeC) or p-p/ion-ion (ALICE). This means that a multipurpose detector would need to be installed [49], satisfying the demand of LHeC, as well as ALICE. A drawback of this machine design is, that the second

proton beam, which does not collide with the electron beam, needs to be guided around the e-p collision in the same beam pipe in IR2. In this kind of design, the distance between the last focusing quadrupole and the collision point ($L^*$) amounts to $22.965\,\mathrm{m}$. This has a direct impact on how strongly the proton beam which participates in the e-p collisions can be focused.

The major and unprecedented advantage of this design is the possibility of collecting either e–p or p–p collision data in this interaction region.

In this PhD two different triplet magnets in the LHeC interaction region have been tested. The optics design aimed at maximizing the luminosity of the e-p collisions, while also assuring that the second proton beam stays far enough away from the colliding proton beam in this IR. For this machine design of LHeC, the reachable luminosities, together with their $\beta^*$ values as well as the necessary machine changes are summarized in table 16.

| **Parameter** | **NbTi triplet** | **$Nb_3Sn$ triplet** |
|---|---|---|
| $L^*$ | $22.965\,\mathrm{m}$ | $22.965\,\mathrm{m}$ |
| $\beta_p^*$ | $0.45\,\mathrm{m}$ | $0.2\,\mathrm{m}$ |
| Luminosity | $1.1 \times 10^{33}\,\mathrm{cm}^{-2}\,\mathrm{s}^{-1}$ | $2.5 \times 10^{33}\,\mathrm{cm}^{-2}\,\mathrm{s}^{-1}$ |
| Hardware Changes | • Electron Magnet Insertion 4<br>• Recabling of Quadrupoles 5.2.1 | • Electron Magnet Insertion 4<br>• Recabling of Quadrupoles 5.2.1<br>• $Nb_3Sn$ magnets 5.3 |
| Detector Design | Multipurpose [49] | Multipurpose [49] |

**Table 16:** Performance parameters for an interaction region design of LHeC, which would alternate with p-p/ion-ion operation.

This table shows, that investing into $Nb_3Sn$ magnets would lead to twice the luminosity in this type of multipurpose design. Additionally, the aperture margins would be significantly increased with this magnet technology, as was shown in section 6. The cost of superconducting magnets is largely driven by the price of the conductor and the complexity of the fabrication process. In a recent dipole magnet study at CERN [93], $Nb_3Sn$ conductor procurement costs were found to be several times higher than those of NbTi, with values of approximately $2274\,€/\mathrm{kg}$ compared to about $330\,€/\mathrm{kg}$, respectively. While $Nb_3Sn$ technology offers a clear performance advantage, the higher costs need to be weighed in against the overall design objectives.

## 8.2 LHeC as a Stand Alone Experiment

In previous studies of LHeC, a stand alone experiment was foreseen. This means, that IP2 would be used exclusively for e-p collisions and p-p collisions would no longer be possible in this IP. It would also run concurrently to the other HL-LHC experiments. For this design a luminosity of $5 \times 10^{33}\,\mathrm{cm}^{-2}\,\mathrm{s}^{-1}$ was anticipated, see table 17.

| **Parameter** | $\beta^*$=0.1 m [11] | $\beta^*$=0.07 m [11] |
|---|---|---|
| $L^*$ | 15 m [94, 95] | 15 m [94, 95] |
| Luminosity | $5 \times 10^{33}\,\mathrm{cm}^{-2}\,\mathrm{s}^{-1}$ | $7.2 \times 10^{33}\,\mathrm{cm}^{-2}\,\mathrm{s}^{-1}$ |
| Hardware Changes | • $Nb_3Sn$ magnets [95]<br>• Estimated Costs: 1371 MCHF [96] | • $Nb_3Sn$ magnets [95]<br>• Estimated Costs: 1371 MCHF [96] |
| Detector Design | Approx. length of 13 m [11] | Approx. length of 13 m [11] |

**Table 17:** Performance parameters for designs of LHeC as a stand alone experiment. The luminosities have been calculated using the parameters in table 8.

For this design, it would be necessary to lower $L^*$ down to a value of 15 m. This places additional constraints on the electron machine design, as the electron beam must be bent more strongly up- and downstream of the collision, resulting in increased synchrotron radiation emission [32]. Furthermore, the installed detector would need to be shorter to make it possible to reach this $L^*$. A possible design for this kind of detector is presented in [11, 97]. For values down to $\beta^*$ =0.07 m, the margins to the triplet walls are getting very thin, but the machine would still be able to operate. The magnet technology which would be necessary to go below 0.07 m, is summarized in [95]. Some of the designs of these magnets still need to be verified. Additionally, it would be necessary to test weather it would be possible to correct the chromaticity for this intense focusing of the proton beam.

## 8.3 Summary

The reachable luminosities for the different designs of LHeC are summarized in table 18.

From this table, it can be seen that the optics and the interaction regions developed in this PhD can reach one fifth up to one half of the luminosity that is anticipated to be reached with LHeC as a stand alone experiment. While not reaching the ultimate luminosity targets of a dedicated LHeC design, this perfor-

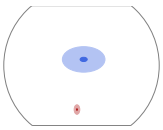

| LHeC Design | Magnet Technology | Luminosity [$cm^{-2}s^{-1}$] |
|---|---|---|
| LHeC alternate to p-p | NbTi | $1.1 \times 10^{33}$ |
| LHeC alternate to p-p | $Nb_3Sn$ (design completed) | $2.5 \times 10^{33}$ |
| LHeC stand alone | $Nb_3Sn$ (significant R&D necessary) | $5.0 \times 10^{33}$ |

**Table 18:** Comparison of luminosity reaches for different proposed designs of LHeC. *LHeC alternate to p-p* represents the design created in this PhD, which allows for either operation: e-p (LHeC) or a-a (ALICE). LHeC as a *stand alone* experiment represent a previously designed LHeC interaction region solely designed for e-p interactions. All designs run concurrently to the other experiments in HL-LHC.

mance demonstrates that a substantial fraction of the anticipated luminosity can be achieved within the proposed constraints.

The design created in this PhD is based on superconducting magnet technology, which is either already in use (NbTi), or in the process of being commissioned for HL-LHC ($Nb_3Sn$ magnets). One of these triplet magnets, has recently been tested and passed five thermal cycles [98]. As a result, this approach benefits from a high level of technological maturity. In contrast to a fully stand-alone LHeC interaction region, no additional dedicated R&D on proton triplet magnets would be required.

An additional advantage of the proposed design is its compatibility with the ALICE 3 program. The ALICE collaboration is studying an upgrade for its detector for RUN 5 ( to be commissioned around 2036) [99, 100], although no decision on the construction has been taken yet. Running LHeC as a stand alone experiment would increase its luminosity by a factor of 2, with the draw back of not enabling ALICE 3, as well as needing new magnet technology for this IR (with significant R&D).

In this context, the design presented here can be viewed as a flexible intermediate solution. It enables significant e–p physics potential while preserving compatibility with the broader HL-LHC physics program through the end of Run 5 (around 2041 [22]). Beyond this period, the interaction region could be upgraded to a dedicated stand-alone e–p configuration, potentially serving as a transitional project prior to the anticipated commissioning of FCC-ee in the late 2040s.

# 9 Design of the Interaction Region for the FCC-eh Collider

In this chapter, a possible layout for an electron hadron interaction region for the Future Circular Collider (FCC-eh) is presented.

The FCC is a proposed circular collider at CERN. It is currently in the design study phase (see the feasibility report [101]). FCC is supposed to be commissioned in the late 2040s for $e^-$- $e^+$ operation and then supposed to run for 25 years [102]. It could then be upgraded for h-h operation and be commissioned in the late 2070s [102] for h-h operation. The e-h interaction region could be added during the h-h upgrade or after the first h-h runs. A possible timeline is shown schematically in figure 16. Similar to the LHC, the FCC design investigated in this PhD study foresees four interaction points. One of these interaction points could be used for e-h operation. The circumference of the FCC would amount to $90.66\,\mathrm{km}$[103] with proton-proton collisions reaching a center-of-mass energy of $85\,\mathrm{TeV}$ [101] up to $100\,\mathrm{TeV}$ [16, 103], depending on the available dipole technology. The FCC-hh is expected to reach an instantaneous luminosity of up to $3 \times 10^{35}\,\mathrm{cm}^{-2}\,\mathrm{s}^{-1}$ [104].

The main **physics case** of the FCC-hh, as well as the FCC-eh includes high precision measurements of the Higgs Boson and its couplings and self-couplings, as well as an exploration of physics beyond the Standard Model [105–107]. As the FCC-eh would be performing deep inelastic scattering, it would study high precision parton distributions, as well as quantum chromo dynamics at unprecedented kinematic reach (see figure 3). A summary of the physics case is presented in section 1.1. The two colliders are complementary, with FCC-hh focusing on rare processes and direct searches for new particles at the energy frontier while FCC-eh provides high-precision measurements in a cleaner experimental environment.

The e-h interaction region which was integrated in this PhD has been designed for the layout of the Future Circular Collider hadron hadron (FCC-hh) published in the 2025 feasibility study report [101, 108]. More information on the h-h lattice can be found here [16, 103]. The calculations have been performed with a proton beam energy of $50\,\mathrm{TeV}$. Different to LHeC, this hadron collider machine is still being developed at this moment, and therefore there are more options on how to design the e-h interaction region. It would be possible to build FCC-eh either as a stand alone experiment and use one interaction region of FCC for e-h collisions only.

In this chapter, an IR design is explored that would allow either e-h or h-h collisions in point D of the FCC-hh, similar to what was explored in previous chapters

for LHeC. In figure 69, a schematic layout illustrates how this design could fit into the overall FCC configuration.

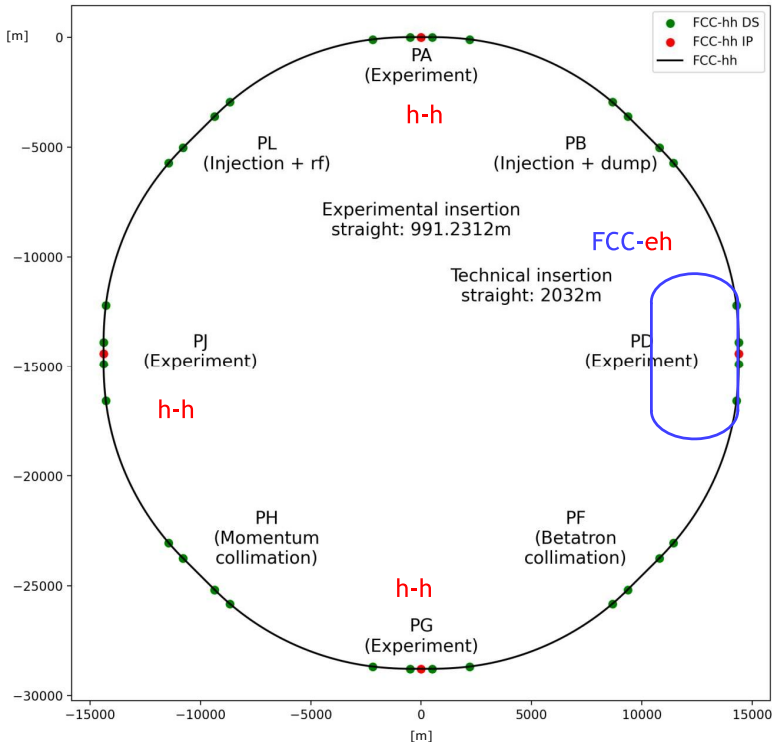


**Figure 69:** Schematic layout of a possible design of FCC-eh. The three h-h collisions are marked, together with the dispersion suppressors (DS). An ERL is placed in interaction point D (PD), which could enable e-h collisions in this IR. Figure adapted from [13, 14] with modifications.

The ERL designed for this interaction region would be of a length of $9\,\mathrm{km}$ and, as in the design for LHeC, would accelerate the electrons over three turns to a final energy of $60\,\mathrm{GeV}$. For an ERL of this size, the energy recovered amounts to $97.92\,\%$ [32], as less energy is lost in synchrotron radiation. The protons would be accelerated in the FCC-hh to a final energy of $50\,\mathrm{TeV}$. Due to their different beam emittances, the proton beam will be focused to a $\beta^*$ of $30\,\mathrm{cm}$, while the electron beam is focused to a a $\beta^*$ of $7.3\,\mathrm{cm}$. This results in a beam size of $3.5\,\mu\mathrm{m}$ at the IP for both beams [32]. The parameters for the e-h collisions in FCC-eh are summarized in table 19. These values yield a geometric luminosity of $1.36 \times 10^{35}\,\mathrm{cm}^{-2}\,\mathrm{s}^{-1}$ for FCC-eh which is about a factor of $100$ higher than that of the LHeC.

| Parameter | Protons | Electrons | Unit |
|---|---|---|---|
| Maximum Energy $E_{p/e}$ | 50 000 | 60 | GeV |
| Transverse Normalized Emittance $\varepsilon$ | 2.2 | 20 | µm |
| Amplitude function at the IP $\beta^*$ | 30 | 7.3 | cm |
| Number of Particles $N_{p/e}$ | $10 \times 10^{10}$ | $3.1 \times 10^{10}$ | - |
| RMS bunch length $\sigma_z$ | 0.06 | 8 | cm |
| Bunch Spacing | 25 | 25 | ns |
| Relativistic $\gamma$ | 53 289.45 | 117 416.83 | - |
| Total Length | 90.66 | 9 | km |

**Table 19:** Key beam parameters for the luminosity for the FCC-eh design used in this thesis [32, 109].

## 9.1 Implementation of the Electron Hadron Interaction Region

In order to collide the electrons with the hadrons in the FCC-eh collider, additional magnets need to be installed into the hh-lattice, as it has been done for LHeC in chapter 4. These magnets are designed for the guidance and the focusing of the electrons. As they are inserted into the hh-lattice, they affect the proton beams as well. The protons reach a much higher collision energy $E_p$ than the electrons do and therefore the impact of the electron magnets on the protons is reduces by a scaling factor of:

$$\frac{E_e}{E_p} = \frac{60 \text{ GeV}}{50000 \text{ GeV}} = 0.0012. \tag{78}$$

This factor is approximately six times smaller than the corresponding scaling factor for the LHeC. Consequently, the expected impact on the proton orbit and optics is small.

In figure 70 a schematic representation of the inserted electron magnets (with their corresponding names) is displayed, together with the two proton beams, as well as the electron beam.

Figure 70 shows the proton final focusing quadrupole magnets of the triplet (Q1, Q2, Q3). In this case, the first and the third triplet quadrupoles each consist of two magnets, and the second quadrupole consists of four magnets. As it has been done for the electron insertion in the LHC lattice for LHeC, a doublet consisting of

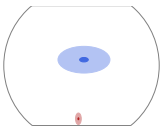

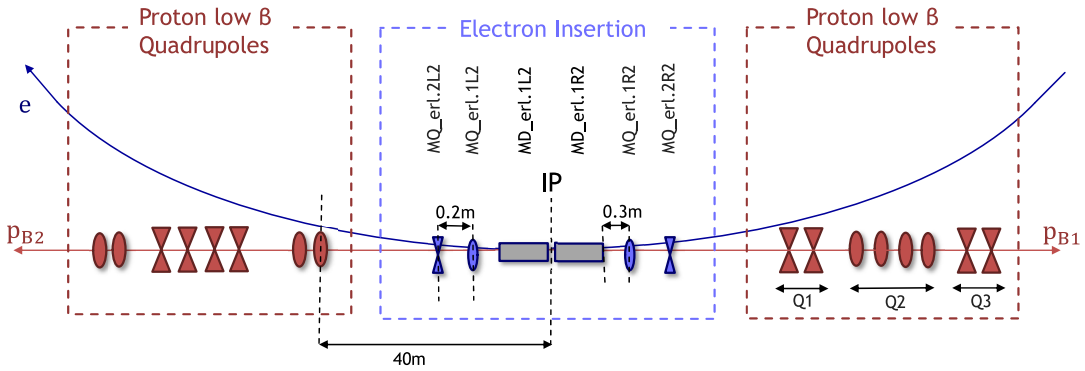


**Figure 70:** Schematic display of the final focusing system of the protons (red), as well as the final focusing system of the electrons (blue) and their dipole magnets (grey). The electron beam is schematically represented in blue, while the proton beams are represented in red. The names of the newly inserted magnets for the electrons are marked on the top.

one focusing and one defocusing quadrupole, is installed for the electron beam. These are used to focus the electron beam. Two dipole magnets are installed right next to the IP, in order to guide the electron beam into the collision and then back into the ERL. In this case, the distance between the last triplet magnet of the protons and the IP amounts to $L^*$ =40 m. Compared to the $L^*$ =23 m of LHeC, it is easier to bend the electron beam.

## 9.2 Impact of the Electron Insertion on the Proton Beams

After the installation of the electron insertion into the FCC-hh lattice, the impact of this insertion on the protons has been investigated. As the design of this interaction region is fairly recent, these studies have been performed on one of the proton beams and only locally in the interaction region D of the FCC-hh lattice, as a complete layout was not yet available.

### 9.2.1 Impact of the Electron Insertion on the Orbit of the Proton Beams

As the protons pass through the electron insertion, their orbit is impacted. They are deflected in the x-plane by the dipoles of the electron insertion, as well as by the quadrupoles, since they are slightly misaligned to the design orbit. This creates a feed-down effect, which is exploited here, in order to further bend the electron beam. This misalignment has been recalculated in reference to the proton

orbit, analogously as it has been done for LHeC in chapter 4.

The distorted orbit $x(s)$ has been defined in equation 56. It is repeated here for convenience. The distorted orbit at a position $s$ for a dipole placed at position $s_0$ can be calculated using:

$$x(s) = \frac{\vartheta}{2\sin(\pi Q)}\sqrt{\beta(s)\beta(s_0)}\cos(|\psi(s) - \psi(s_0)| - \pi Q). \tag{79}$$

Here $\vartheta$ describes the deflection angle applied at $s_0$, and $\psi(s)$ describes the phase advance at the position $s$, while $\psi(s_0)$ describes the phase advance at the location of the dipole. $\beta(s)$ represents the amplitude function at the measured position and $\beta(s_0)$ the amplitude function at the position of the dipole. This equation can be found in [68].

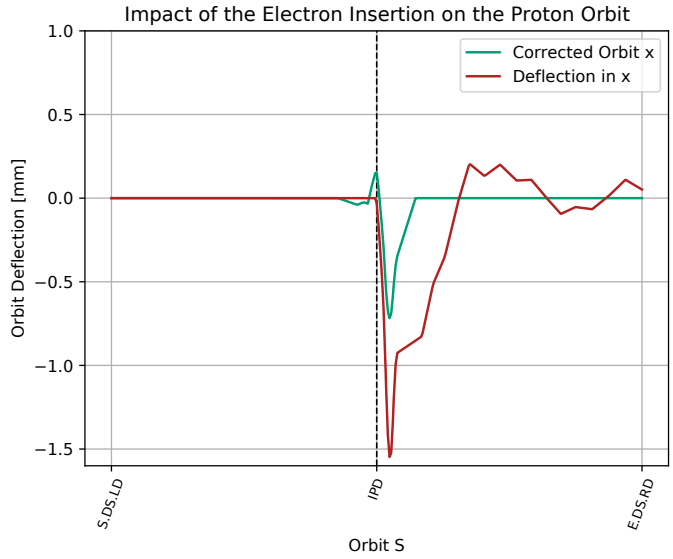


**Figure 71:** Orbit distortion in the x-plane for the proton beam after installation of the electron insertion (see figure 70). The dipoles and misaligned quadrupoles deflect the beam in the horizontal plane. The dashed line marks the position of the IP. The applied correction on the horizontal orbit is displayed in green. The orbit was corrected at the IP, as well as before reentering the periodic arcs in the lattice (at the dispersion suppressors S.DS.LD and E.DS.RD). The position of the used orbit correctors are marked.

With this equation, the orbit deflection caused by the electron insertion at the position of the dipole downstream of the IP (MD_erl.1R2 in figure 70) was calculated. The calculated value amounts to a distortion of $0.2\,\mathrm{mm}$. This value is really

small, as expected from the scaling factor given in equation 78. The orbit distortion at this dipole is subsequently modeled with MAD-X. The thus calculated value amounts to $0.13\,\mathrm{mm}$. The in MAD-X calculated orbit distortion considers also the quadrupoles and this might be why the two values differ slightly. The caused deflection can be seen in figure 71. Note that the calculated value is positioned very close to the IP and the total orbit distortion is bigger than this value. The distortion was subsequently corrected using the first two orbit correctors adjacent to the triplet, as shown by the green curve in Fig. 71.

### 9.2.2 Impact of the Electron Insertion on the Optics of the Proton Beams

The collision optics of the proton beam at IPD of the FCC-eh can be seen in figure 72.

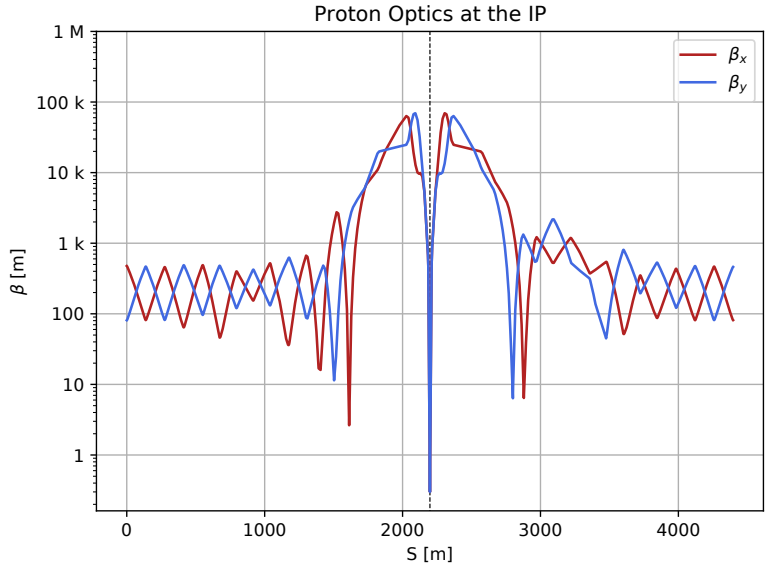


**Figure 72:** Optics of the proton beam at the interaction point D of the FCC-eh. The amplitude function in the x-plane $\beta_x$ is displayed in red while the amplitude function in the y-plane $\beta_y$ is displayed in blue. For improved visibility, the optics are displayed on a semi-logarithmic scale. The amplitude function at the IP amounts to $\beta^*$=30 cm.

Since the protons also pass through the quadrupoles which focus the electrons, their optics are slightly affected, analogously to LHeC in chapter 4.

In figure 73 the resulting beta-beat is plotted against the position $s$ on the orbit

of the protons. This beta-beat is defined as the relative deviation between the original amplitude function $\beta_0(s)$ and the perturbed amplitude function value $\beta(s)$ at position $s$ normalized to the original amplitude function:

$$\frac{\Delta\beta(s)}{\beta(s)}[\%] = \frac{\beta_0(s) - \beta(s)}{\beta_0(s)} \cdot 100. \tag{80}$$

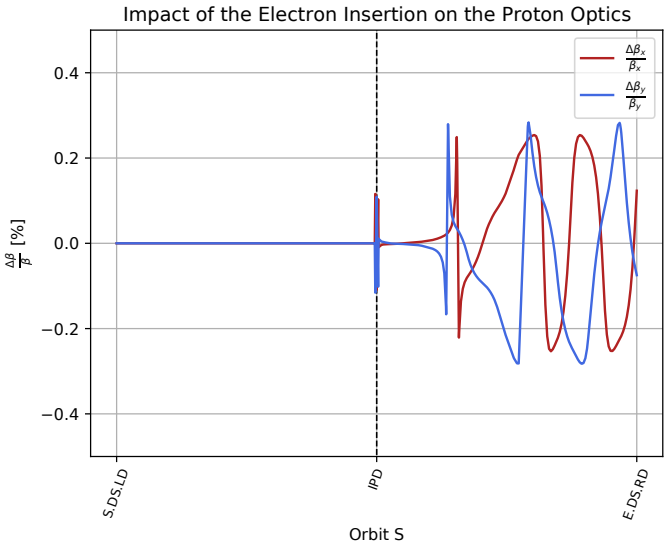


**Figure 73:** Relative change in the amplitude function in the horizontal (red) and the vertical (blue) plane after insertion of the electron elements into the FCC-hh proton lattice.

The observed beta-beat is of the order of $0.3\,\%$. This effect is very small, which is expected, as the proton and electron beam vary greatly in their energies. This impact on the optics has been corrected with the use of the matching quadrupoles of this interaction region. The optics are matched at the IP and at the end of the dispersion suppressor downstream of IPD (E.DS.RD). This way, the optics is corrected, before the beam reenters into the periodic arc. This correction is shown in figure 74.

It can be seen that by correcting the optics locally, the total magnitude of the beta-beat increases to up to almost $7\,\%$ downstream of the IP, before disappearing.

A detailed overview of the MAD-X files used in order to create these optics, as well as the files which correct the orbit, can be found in the appendix C.

These results show, that it would be possible to install the electron magnets and consequently perform high luminosity e-h collisions in point D of the FCC-hh.

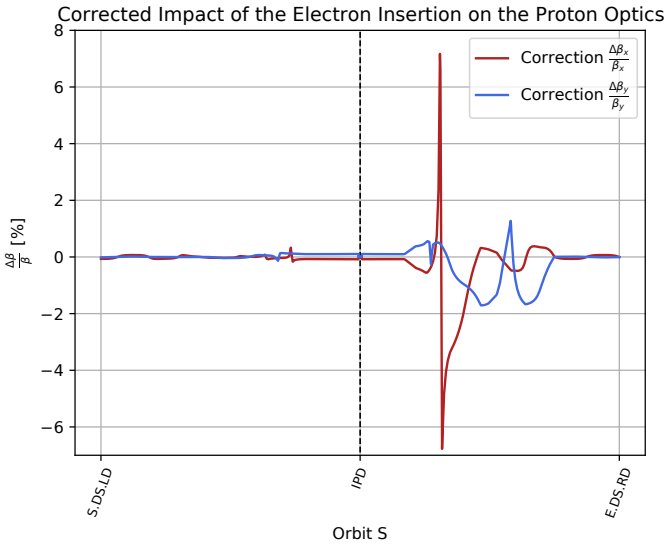


**Figure 74:** Display of the applied correction to the proton optics of the FCC-eh collider, after the electron magnets have been inserted. The position of the IP is indicated with a dashed black line. The positions of the dispersion suppressors (E.DS.DR and S.DS.LD) are marked. These points mark the transition between the periodic arcs and the straight interaction regions and the points at which the optics was rematched.

The impact on the orbit, as well as on the optics can be corrected locally, without further hardware modifications. It would still need to be decided if this experimental area will be used as a stand alone experiment for e-h, or if it will be used alternatively for h-h as well. In the case of a stand alone experiment the second proton beam would be guided through its own beam pipe. For an experiment which can house either, e-h or h-h experiments, a separation scheme for the protons, as it has been done for LHeC, would need to be developed. This chapter also demonstrates that, compared to the LHeC, designing the interaction region for FCC-eh is more flexible, as more freedom remains in the choice of design parameters.

# 10 Summary

During LHeC operation, the two proton beams of HL-LHC would collide with each other in three interaction points (ATLAS, CMS, LHCb), while one of the two proton beams would also collide with an electron beam from an **energy recovery linac**, built tangentially to HL-LHC.

In this PhD two distinct interaction regions for the LHeC collider were designed. The difference between the two designed interaction regions is the superconducting technology out of which the final focusing system for the protons is built. The currently installed one in this interaction point of LHC consists of Niobium titanium (NbTi), whereas the alternative design uses magnets built out of Niobium Tin ($Nb_3Sn$) which would allow for stronger beam focusing.
These new interaction regions differ from previous LHeC interaction regions by also allowing p-p or ion-ion collisions alternatively to the e-p operation. The main challenge of this type of interaction region is that **three particle beams must pass through the LHeC interaction region**:

1. the clockwise rotating proton beam of HL-LHC, which collides with the electrons (B1)
2. the counterclockwise rotating proton beam of HL-LHC, which collides with the other proton beam in the three remaining interaction regions (B2) and
3. the electron beam from the ERL.

As a first step, the electron magnets, which were designed to guide and focus the electron beam [32], were introduced into the proton HL-LHC lattice in MAD-X. The **impact of the electron magnets** on the proton optics and closed orbits was quantified and subsequently corrected.
To allow all three beams to circulate through the same beam pipe while ensuring that only B1 collides with the electrons, a dedicated **separation scheme** was developed. Its purpose is to position B2 as far away as possible from the e-p collisions while maximizing the e-p luminosity with B1. In this way the detrimental beam-beam effects of the proton beams on each other can be minimized. This separation scheme relies on asymmetric proton beam optics and orbits. While B1 is aggressively focused to maximize the e-p luminosity, B2 maintains a nearly constant size throughout the interaction region. With a combination of separation and crossing orbit bumps, the two proton beam orbits are effectively separated. This separation scheme is displayed in the reference system of the protons in the LHeC interaction region in figure 75.

With the current superconducting technology of LHC, it was possible to separate the proton beams by more than $17.5\,\sigma$, while reaching a luminosity of

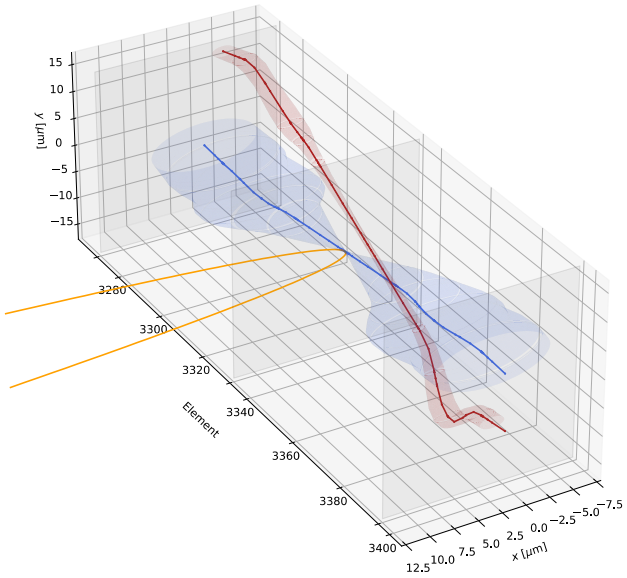


**Figure 75:** Display of the designed three beam interaction region. The clockwise rotating proton beam (blue) collides with the electron beam (orange), while the counterclockwise rotating proton beam is guided around the e-p collision (red). The proton beams are plotted with $5\,\sigma$ envelopes in the reference system of the proton beams [66].

$1.1 \times 10^{33}\,\mathrm{cm}^{-2}\,\mathrm{s}^{-1}$ with only minor changes to the machine layout.
To further increase the achievable luminosity a final focusing system using **Niobium Tin technology** ($Nb_3Sn$) was implemented into the LHeC interaction region, replacing the currently used NbTi system. These are the same magnets used for the High-Luminosity LHC (HL-LHC) upgrade in interaction region 1 and 5, scheduled to be commissioned in 2029. These magnets are therefore already designed, developed and tested, needing no further R&D. With this upgraded system a beam distance of $12.9\,\sigma$ was reached between the two proton beams, while enabling an e-p luminosity of $2.5 \times 10^{33}\,\mathrm{cm}^{-2}\,\mathrm{s}^{-1}$.

**This is the first design for an LHeC interaction region capable of supporting two operational modes: e-p or p-p.**

Furthermore, all components required for both designs already exist and have been validated. The choice between the two final-focusing systems for LHeC is therefore primarily a matter of available budget. Current cost estimates indicate that the procurement costs for $Nb_3Sn$ magnets are approximately an order of magnitude higher than those for NbTi magnets [93].

As a next step, the **beam-beam impact** of the electron beam on the colliding proton beam B1 was studied using numerical tracking simulations. These simulations were performed using the Xsuite framework and showed that the electron beam has essentially no detrimental effect on the protons. If anything, it produces a slightly focusing, or pinch effect, which can further increase the e–p luminosity. Finally, the **dynamic aperture** of the colliding proton beam was evaluated for the current machine layout of HL-LHC, using a final focusing system consisting of NbTi. This study revealed that the main limitation to the luminosity at this moment is the available aperture, followed possibly by high amplitude particle losses due to the chromatic correction of the sextupoles. Neither effect poses a limitation to the previously mentioned luminosity.

For the **Future Circular Collider for electron hadron Collisions** (FCC-eh), the electron magnets, which steer and focus the electron beam, were inserted into the 2023 FCC-hh proton lattice [16]. As it was done for LHeC, the impact of these magnets on the proton optics and orbit was quantified and locally corrected. The calculations performed in this PhD provide a quantitative basis for assessing the competitiveness of different e-p collider concepts and for evaluating their potential physics reach.

# 11 Outlook

It would be interesting to study the **dynamic aperture** for the LHeC design using the $Nb_3Sn$ final focusing system for LHeC. Additionally, this machine design could be expanded to include higher-order magnetic fields, such as sextupoles, octupoles, and dodecapoles. These elements were omitted in the present design, as their inclusion would exceed the scope of this thesis. Since this final focusing design uses very small beam sizes (and consequently high quadrupole gradients) at the interaction point, the dynamic aperture studies are necessary to verify the designed chromatic correction.

Furthermore, the potentially detrimental **beam-beam** effects of the two proton beams on each other should be investigated, in order to verify if the designed distance optimization is sufficient for both machine designs of LHeC presented in this thesis. During these dynamic aperture studies, the impact of higher order multipoles could additionally be investigated.

For the **FCC-hh** layout, only a single proton beam has been considered so far, as additional beams were not yet available in the simulation framework. In the

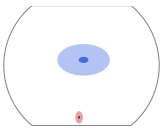

future, a complete design will need to include both proton beams and determine how the electron–proton (e–p) interaction is utilized. This could be implemented either as a dedicated e–p interaction region or, similar to the LHeC design presented in this thesis, as an interaction region capable of alternating between e–p and p–p operation.

## Acknowledgements

I want to thank everyone who contributed to this thesis. Some of these contributions were not strictly scientific and might seem invisible at first. I want to thank everyone who helped me in their own way. By listening to me, making me food, by calling me, by sending me a song or by making me laugh or cry. By telling me to go on. Thank you, you know who you are.
Your work and care are not invisible. They are on every page of this book, on every line and in every word. It is just as invisible as the actual collisions in a particle detector or the energy poured into it. Consider this thesis as scattered debris, as successful experimental results, predicted by a few particular people, not all of them physicists.

I ow my greatest thanks to **Jörg Pretz**. Thank you for predicting potential in me (that is non-zero!). Thank you for making my dream of working at CERN come true. Thank you for your time, your energy, your support and your expertise. It is an honor to learn from you.
Thank you to **Bernhard Holzer** for introducing me to the beautiful field of accelerator physics. Thank you for the many hours and coffees, where you shared your greatly appreciated expertise with me.
I want to thank my office mate **Peter Kicsiny** for always being there for me. Maybe it was because we shared an office and you could not really be somewhere else (too big to exist in a superposition, I assume) but I think it is because you are kind and caring. Thank you for the many moments that in retrospect seem so mundane, like our daily cafeteria raid or using the fax machine.
In terms of optics, I would like to thank **Leon van Riesen-Haupt**, **Michael Hofer**, **Joschua Dilly** and **Riccardo de Maria** for teaching me how to use MAD-X without going completely insane, despite what the name of this program suggests. Thank you for your excellent advice. Your mentorship made me want to go on and rediscover my PhD, when I thought about giving up.
I want to thank **Pascal Hermes** for teaching me how to use Xsuite, as well as how to play *live forever* on guitar.
Thank you to **Tévin Daniel Joël André** for providing the electron insertion and his advice on the LHeC.
Thank you to my former student **Matthew Smith** for your hard work and creativity and for placing your trust in me. I wish you all the best for your own PhD.
My gratitude goes to **Lars-Thorben Moos** for sharing your knowledge on particle physics and for proof reading.
Thank you to **Roxana Pohlmann** for supporting me and guiding me in the process of writing up.
Thank you to **Micho Serans** for proof reading my thesis a hundred times. Thank you for teaching me about (programming) language, about truth and about bugs.

I want to express my gratitude to my **family**. First of all, to my brother Moritz. Thank you for *always* being there for me. Even now, as you are sending me corrections way past midnight. Thank you to my father for nurturing my curiosity and for buying me a microscope in 2006. At the time I did not know that I would need a way bigger microscope to understand what matter is made of. Thank you for teaching me how to believe in myself and for proof reading my introduction, as I am typing this. Thank you to my mother for her support throughout my life, for always having a place for me to come home to and for teaching me to bring humor into my life. Thank you to Beate for her support in diplomatic questions and matters (and antimatters) of the heart, as well as showing me how to use oxford commas. Thank you all for having my back at all times and supporting my dreams.

Power

Living in the earth-deposits of our history

Today a backhoe divulged out of a crumbling flank of earth
one bottle amber perfect a hundred-year-old
cure for fever or melancholy a tonic
for living on this earth in the winters of this climate.

Today I was reading about Marie Curie:
she must have known she suffered from radiation sickness
her body bombarded for years by the element
she had purified
It seems she denied to the end
the source of the cataracts on her eyes
the cracked and suppurating skin of her finger-ends
till she could no longer hold a test-tube or a pencil

She died a famous woman denying
her wounds
denying
her wounds came from the same source as her power.

–Adrienne Rich, *The Dream of a Common Language [110]*

# A Appendix I: Electron Magnet Insertion and Proton Beam Optics

## A.1 Installation of the Electron Insertion

The MADX-X files used to install the electron insertion into the HL-LHC proton lattice can be found in the LHeC git repository: `https://github.com/agiantmanatee/LHeC/electron_insertion`. The electron insertion sequence file `LHeC/electron_insertion/sequences/install_erl.seq` installs the electron magnets into the existing proton lattice, without turning on the magnets yet. In order to turn on the electron magnets, the additional strength file: `LHeC/electron_insertion/strengths/electrons_syn.str` needs to be loaded. This file assigns strengths to the magnets different from zero and in return "turns on" the electron insertion. These two files need to be loaded additionally to the LHC sequence `LHeC/vendor/HLLHCV1.5/lhc/lhc_sequence.madx` and the HL-LHC upgrade `LHeC/vendor/HLLHCV1.5/hllhc_sequence.madx`, as well as a file which defines the strengths for the proton magnets.

The magnetic strengths, as well as the magnet lengths and their positioning to the IP of the electron insertion are summarized in table 20 for the dipoles and in table 21 for the quadrupoles. The dipoles are placed directly adjacent to the IP.

| Magnet | Bending angle [rad] | $k_0$ [$\mathrm{m}^{-1}$] | Length [m] |
|---|---|---|---|
| MD_erl.1L2 | 0.005 378 | $4.499\,977 \times 10^{-4}$ | 11.951 17 |
| MD_erl.1R2 | 0.005 378 | $4.499\,977 \times 10^{-4}$ | 11.951 17 |

**Table 20:** Summary of the values assigned to the two dipole magnets, which guide the electron beam out of the ERL into the collision with the proton beam and back into the ERL. Here, $k_0$ represents the bending strength of the dipole. These values have been calculated for the collision energy of the electrons and were rescaled for the protons.

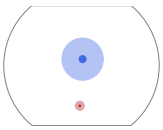

| Magnet | $G$ [T/m] | Length [m] | $\Delta x_{\mathrm{quad_e}}$ [m] | Distance to IP [m] |
|---|---|---|---|---|
| MQ_erl.2L2 | −21.8747 | 1.854 84 | 0.003 43 | −14.3060 |
| MQ_erl.1L2 | 29.0116 | 1.854 84 | −0.002 58 | −12.2511 |
| MQ_erl.1R2 | 29.0116 | 1.854 84 | −0.002 58 | 12.2511 |
| MQ_erl.2R2 | −21.8747 | 1.854 84 | 0.003 43 | 14.3060 |

**Table 21:** Summary of the values assigned to the four quadrupole magnets, that focus the electron beam for its collision with the proton beam in figure 23. Here $G$ represents the quadrupole gradient. The misalignment $\Delta x_{\mathrm{quad_e}}$ describes how far the center of the quadrupole is offset in relation to the electron orbit [111].

### A.1.1 Correction of the Proton Optics after Insertion of the Electron Interaction Region

The proton optics are corrected by using the matching quadrupoles of this interaction region (IR2), as well as the trim quadrupoles, which are usually used to correct the tune. With the file `LHeC/NbTi_triplet/NbTi_rematch_lhec.madx`, the optics, as well as the orbit are rematched for both proton beams. The orbits are corrected with the use of the local orbit correctors in this interaction region, as well as the nested triplet correctors.

## A.2 Creation of the Proton Optics for LHeC

### A.2.1 Proton Optics for the NbTi Triplet

The file with which the different proton optics for LHeC using the Niobium Titanium triplet can be created, is the same as the one that is used to correct the impact of the electron insertions: `LHeC/NbTi_triplet/NbTi_rematch_lhec.madx`. In this file, the $\beta^*$ values of both proton beams can be set independently. The optics are afterwards saved here: `LHeC/NbTi_triplet/NbTi_strengths`.

To generate the optics used in the parameter scan for proton B1 and proton B2, automated scripts for producing multiple optics configurations are available at `LHeC/NbTi_triplet/lhec_strength_B1.py` and `LHeC/NbTi_triplet/lhec_strength_B2.py`.

### A.2.2 Proton Optics for the $Nb_3Sn$ Triplet

The installation file for the Niobium Titanium triplet in IP2 can be found here: `LHeC/Nb3Sn_triplet/sequences/install_triplet_elements.madx`. It installs the $Nb_3Sn$ triplet into point 2 of the HL-LHC lattice. After the installation, an additional strength file needs to be loaded as to apply the strengths to the newly inserted elements. These strength files are generated here: `LHeC/Nb3Sn_triplet/Nb3Sn_rematch_lhec.madx` depending on the desired operational scenario. To generate multiple optics with variable $\beta^*_{B2}$ values for proton B2, an automated script is available at `LHeC/Nb3Sn_triplet/lhec_strength.py`. The thus generated strength files are saved to the folder: `LHeC/Nb3Sn_triplet/strengths`.

## A.3 Optimization of the Proton Beam Separation

### A.3.1 Settings of the Orbit Separation

The two proton beams are separated with the use of separation orbit bumps in the horizontal plane and with crossing bumps in the vertical plane (see figure 43 and figure 44). These orbit bumps are set with the use of orbit corrector magnets. These are small dipole magnets, which steer the beams. In figure 37 the first four correctors of this interaction region are displayed in green. For the NbTi triplet, as well as the $Nb_3Sn$ triplet, it can be seen that the first three correctors are nested within the triplet magnets. These correctors act on both proton beams, as well as on both transversal planes. Once the proton beams are entering their individual beam pipes, they have their own set of corrector magnets. The three nested correctors (labeled 1-3), additionally to the first two individual corrector magnets of each beam (labeled 4 and 5) were used, in order to well define the orbit bumps.

The closed orbit distortion $x(s)$ from a transverse deflection at a position $s_0$ can be calculated using [112]:

$$x(s) = \sqrt{\beta(s)\beta(s_0)} \cdot \frac{\vartheta}{2\sin(\pi Q)} \cdot \cos\left(|\phi(s) - \phi(s_0)| - \pi Q\right) \tag{81}$$

In this equation $\vartheta$ represents the angular deflection applied to the orbit by the dipole corrector magnet, $\beta(s)$ and $\beta(s_0)$ describe the beta function at the measured position and the position of the dipole, respectively. $\phi(s)$ and $\phi(s_0)$ rep-

resent the phase advances at the corresponding positions and $Q$ the tune. This formula shows, that the orbit distortion is related linearly to the magnitude of the applied angular deflection. The transverse deflection angle $\vartheta$ of a dipole can be expressed as [112]:

$$\vartheta = \frac{q}{p} \int B \, \mathrm{dl} \tag{82}$$

In this equation $q$ represent the charge of the particle and $p$ the momentum and as a result, $\frac{p}{q}$ the beam rigidity. $\int B \, \mathrm{dl}$ represents the integrated magnetic field along the dipole of length $l$. This field is usually proportional to the applied current of the dipole $I$:

$$B = k \cdot I \tag{83}$$

Here $k$ represents a magnet calibration constant [112]. From these equations it can be deduced that the orbit distortion at a position $x(s)$ is proportional to the applied current of the magnet $I$:

$$x(s) \sim \vartheta \sim I \tag{84}$$

In order to match different sized orbit bumps in the transversal planes, the strength of the used dipole correctors was measured at several positions. Afterwards a linear fit was applied to these measurements. For the horizontal separation bump an exemplary fit is shown in figure 76 and for the vertical crossing bump an exemplary fit is shown in figure 77.

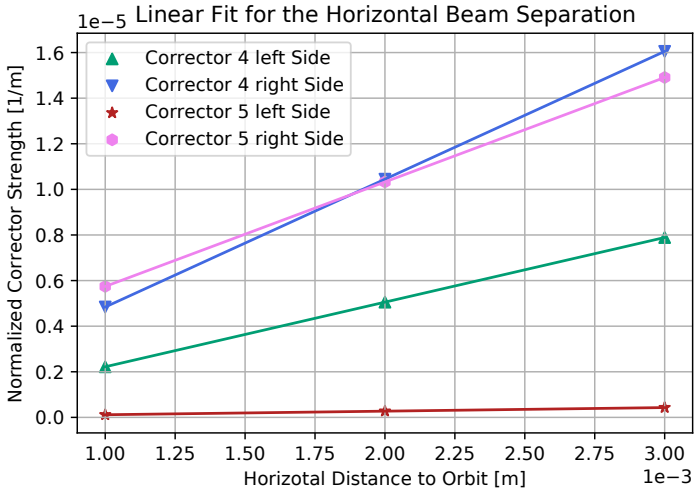


**Figure 76:** Display of the measured corrector strengths for different magnitudes of the horizontal separation bump. In this case the correctors 4 and 5 are shown for B1. The lines represent the linear fit.

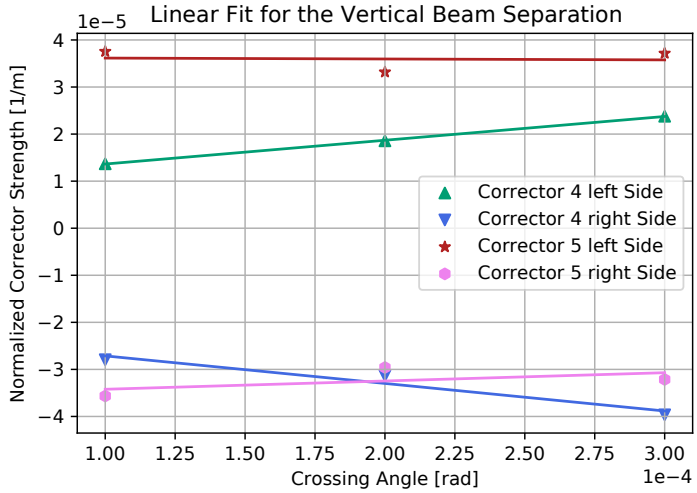


**Figure 77:** Display of the measured corrector strengths for different magnitudes of the vertical crossing bump. In this case the correctors 4 and 5 are shown for B1. The lines represent the linear fit.

In order to find a match more quickly, these fits were used to feed in approximate dipole strength values as starting parameters.

### A.3.2 Optimization of the Proton Beam Separation for the NbTi Triplet

For the NbTi triplet design the orbits bumps were matched to the required amplitudes using the file `LHeC/NbTi_triplet/orbit_bumps.madx`. The files used to generate the corresponding orbit knobs (providing the initial parameters needed to accelerate the matching process) are available at: `LHeC/NbTi_triplet/tools`.

The twiss, survey and aperture files, which are needed for a comparison scan in the separation optimization can be generated for a defined parameter grid with: `LHeC/NbTi_triplet/create_twiss_distance_optimization.py`. The corresponding plots can be generated using: `LHeC/NbTi_triplet/distance_optimization_plot.ipynb`.

**Optimal Inter Beam Distance** In section 6.4.2 the inter beam distance $d$ between the proton beams in sigma of the mean beam size $d\ [\sigma_{\mathrm{B12}}]$ is optimized, while considering $d\ [\sigma_{\mathrm{B2}}]$. In this appendix the inter beam distance results for $d\ [\sigma_{\mathrm{B1}}]$ are presented.

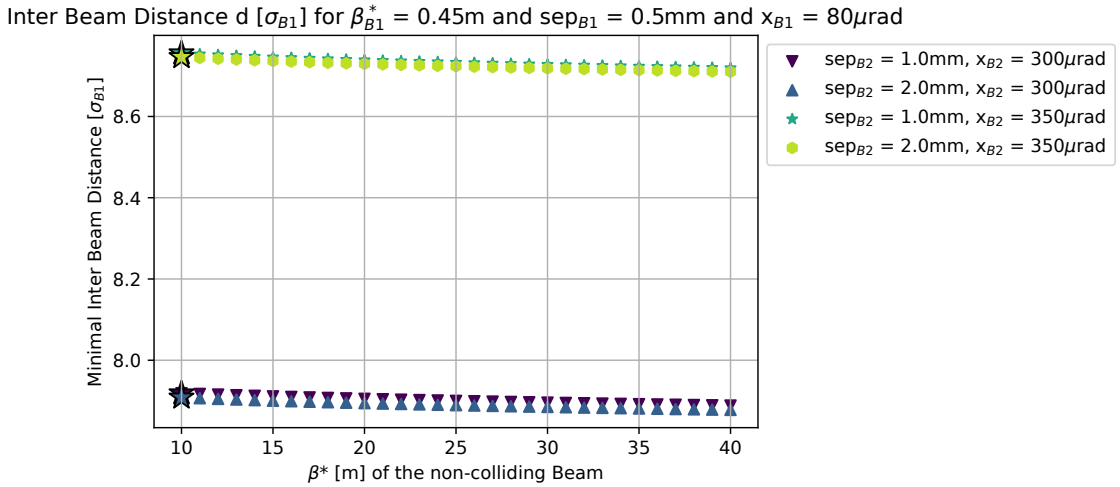


**Figure 78:** Inter beam distance $d[\sigma_{B1}]$ between the two proton beams in their shared beam pipe for $\beta^*_{\mathrm{B1}} = 0.45\,\mathrm{m}$. It is plotted for the optimal orbit configuration of B1 in table 9 as a function of $\beta^*_{\mathrm{B2}}$. Four different curves are shown, for four different orbit configurations of B2.

In figure 78 $d\ [\sigma_{\mathrm{B1}}]$ is presented as a function of $\beta^*_{\mathrm{B2}}$ for the optimal orbit configuration of B1, and all orbit configurations of B2. It can be seen, that the optics of B2 barely affect the inter beam distance $d\ [\sigma_{\mathrm{B1}}]$. The inter beam distance increases with the the magnitude of the orbit bumps of B2.

**Beam stay Clear of B2** In Sec. 6.4.3, the beam stay-clear of B1 was examined, as it is more tightly constrained within the available aperture. In this part of the appendix, the corresponding beam stay-clear for beam B2 is briefly presented.

For each parameter configuration, the beam stay clear has been calculated for both beams. This can be seen for the chosen optimum in figure 53. The minimal beam stay clear $n_1$ for each of these configurations is saved (marked as stars in figure 53) and subsequently plotted as a function of $\beta^*_{\mathrm{B2}}$ for the optimal orbit configuration of B1. This can be seen in figure 79.

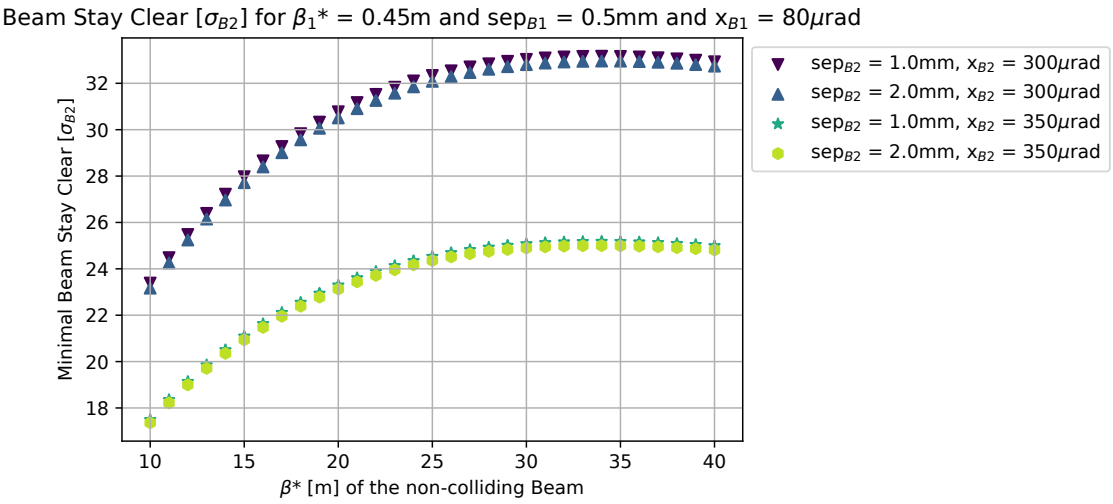


**Figure 79:** Beam stay clear $n_1$ for B2 as a function of $\beta^*_{\mathrm{B2}}$ for the optimal orbit configuration of B1. Four different curves are plotted for four different orbit configurations of B2.

For B2, $n_1$ reaches a plateau around $\beta^*_{\mathrm{B2}}$=32 m. This is because at roughly 32 m downstream of the IP, the vertical crossing bump of B2 reaches its peak (see figure 44). This is the point at which B2 reaches its minimal $n_1$. Setting $\beta^*_{\mathrm{B2}}$=32 m minimizes the size of B2 at this position and in turn increases $n_1$ (see the calculation in section 8). For all values, the mandatory $n_1$ =7.7 $\sigma$ can easily be reached.

### A.3.3 Optimization of the Proton Beam Separation for the $Nb_3Sn$ Triplet

For the $Nb_3Sn$ design the amplitudes of the orbit bumps were matched using the file `LHeC/Nb3Sn_triplet/orbit_bumps.madx`. The files which create the orbit knobs, in order to find a faster match, can be found here: `LHeC/Nb3Sn_triplet/tools`. The twiss, survey and aperture files, which are needed for a comparison scan can be generated using: `LHeC/Nb3Sn_triplet/create_twiss_distance_optimization.py`.

The corresponding plots can be generated with: `LHeC/Nb3Sn_triplet/distance_optimization_plot.ipynp`.

**Optimal Inter Beam Distance** In this appendix, the behavior of $d$ in units of $\sigma_{\mathrm{B1}}$, as well as $\sigma_{\mathrm{B12}}$ is presented. In figure 80, $d\,[\sigma_{\mathrm{B1}}]$ is plotted as a function of $\beta^*_{\mathrm{B2}}$ for the optimal orbit configuration of B1, for all orbit configurations of B2. In figure 81, $d\,[\sigma_{\mathrm{B12}}]$ is shown.

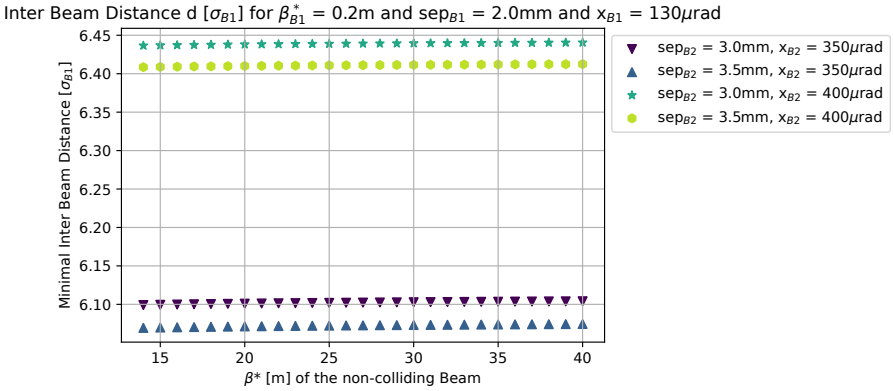


**Figure 80:** Inter beam distance $d[\sigma_{\mathrm{B1}}]$ between the two proton beams in their shared beam pipe for $\beta^*_{\mathrm{B1}} = 0.2\,\mathrm{m}$. It is plotted for the chosen orbit configuration of B1 in table 9 as a function of $\beta^*_{\mathrm{B2}}$. Four different curves are shown for four different orbit configurations of B2.

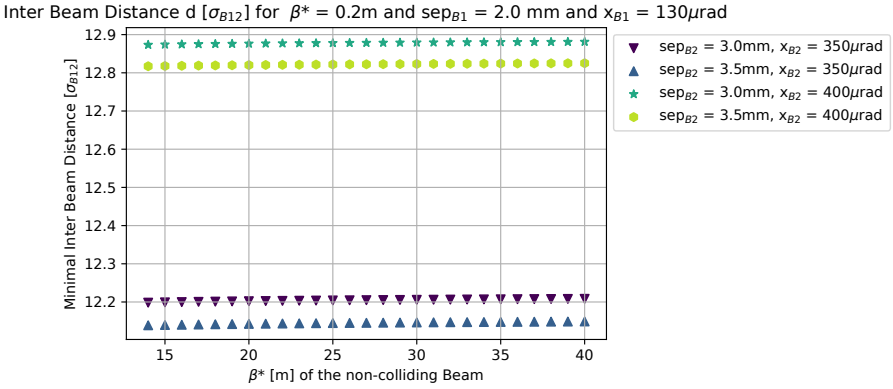


**Figure 81:** Inter beam distance $d\,[\sigma_{\mathrm{B12}}]$ between the two proton beams in their shared beam pipe for $\beta^*_{\mathrm{B1}} = 0.2\,\mathrm{m}$. It is plotted for the best orbit configuration of B1 in table 11 as a function of $\beta^*_{\mathrm{B2}}$. Four different curves are shown, for four different orbit configurations of B2.

In figure 80 and figure 81, it can be seen, that $d\,[\sigma_{\mathrm{B1}}]$ and $d\,[\sigma_{\mathrm{B12}}]$ are independent of the optics of B2, and solely depends on the orbit.

**Beam Stay Clear** In section 6.5 the summary for the $n_1$ values for all orbit configurations was presented for B1 and B2. In this appendix $n_1$ is shown as a function of $\beta^*_{\mathrm{B2}}$ for the chosen orbit configuration of B1.

For each of the 416 combinations of table 11 the minimal beam stay clear value is saved for each beam. As $\beta^*_{\mathrm{B1}}$ is fixed, these minimal values are then plotted for each orbit configuration of B1, versus $\beta^*_{\mathrm{B2}}$. This can be seen in figure 82 for the chosen orbit configuration of B1.

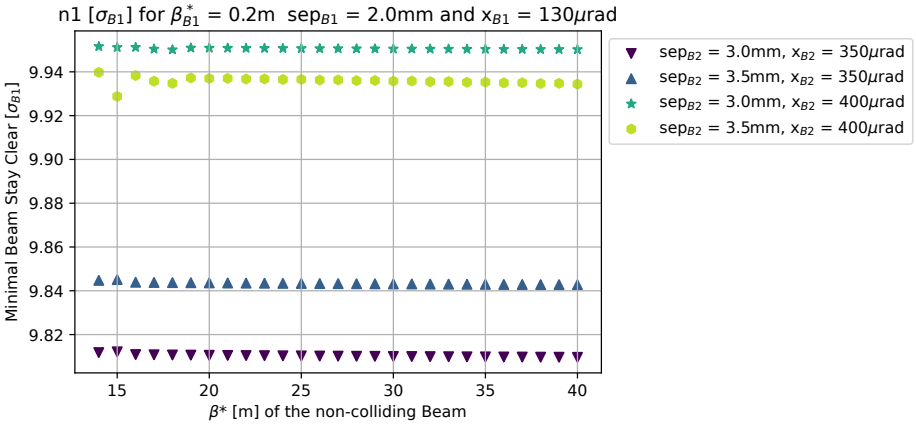


**Figure 82:** Beam stay clear $n_1$ values of B1 as a function of $\beta^*_{\mathrm{B2}}$. The orbit configuration and the optics are set for B1. The four different orbit configurations of B2 are plotted.

In figure 82 it can be seen that the beam stay clear $n_1$ of B1 does indeed not depend on the optics of B2. $n_1$ for B1 does however depend on the orbit configuration of B2. As for the IR design using NbTi technology, the inner correctors are applied on both proton beams, and affect each other. It is therefore not possible to endlessly increase the orbit bumps of B2, even though B2 is still far away from reaching the aperture limit, as B1 could reach the aperture limit.

The beam stay clear $n_1$ of B2 can be seen in figure 83. It reaches a peak around $\beta^*_{\mathrm{B2}}$ = 20m and then $n_1$ falls with a rising $\beta^*_{\mathrm{B2}}$. At a distance of approximately $20\,\mathrm{m}$ downstream of the IP, the vertical crossing bump reaches a maximum. The $n_1$ value is therefore highest for $\beta^*_{\mathrm{B2}}$ =$20\,\mathrm{m}$ as for these optics, the beam reaches the smallest size at this position (see the calculation in section 8).

For all considered parameter settings, B2 remains safely within the aperture limits.

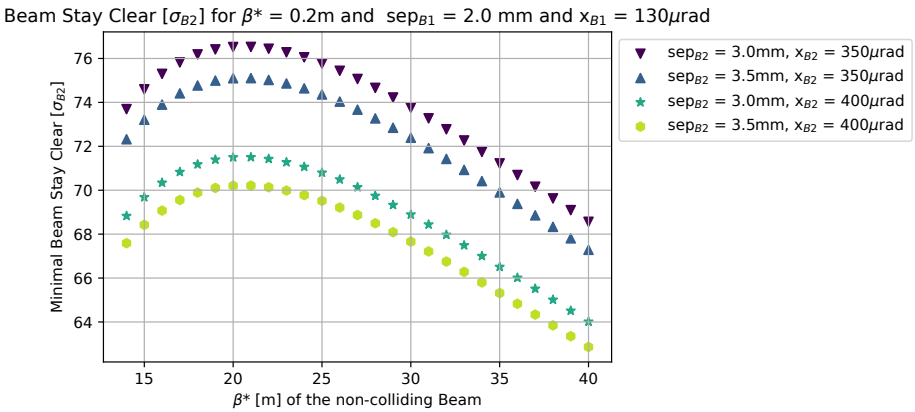


**Figure 83:** Beam stay clear $n_1$ for B2 as a function of $\beta^*_{\mathrm{B2}}$ for the optimal orbit configuration of B1. Four different curves are plotted for four different orbit configurations of B2.

### A.3.4 Plot Generation

The 3D plot can be created using: `3D Schematic Plot.ipynb`. The beam screen plots can be generated here: `cross_section_IR_NbTi.ipynb` for the NbTi triplet and here: `cross_section_IR_Nb3Sn.ipynb` for the $Nb_3Sn$ triplet.

# B Appendix II: Dynamic Aperture Calculations for the LHeC Interaction Region

## B.1 Preparation of the Lattices before Tracking

The HL-LHC, as well as the LHeC optics lattices tracked in section 7 were sliced before being tracked with the use of: `https://github.com/lhcopt/lhcmask/blob/master/python_examples/hl_lhc_collisions_python/000_pymask.py`. By adding the LHeC modifications in `optics_specific_tools.py`, as well as `config.yaml`, the calculations could be performed for the different LHeC optics. During the tracking calculations, field errors were applied to the magnets. These field errors can be found here: `lhcerrors`. The created LHeC lines are saved here: `DA_nbti/lattices`.

## B.2 Chromatic Correction for low $\beta$ values for LHeC using a NbTi Triplet

In section 7 the dynamic aperture was defined for $\beta^*_{\mathrm{B1}}$ =0.45 cm and $\beta^*_{\mathrm{B1}}$ =0.35 cm. In order to push the luminosity even further, an LHeC optics with $\beta^*_{\mathrm{B1}}$ =0.2 cm was designed. As these optics are squeezing the beam aggressively for the collision, the used quadrupole gradients have been set to very high values. As a consequence, the chromaticity increases and the sextupole gradients need to be set to higher values, in order to correct it. It was possible to lower the sextupole gradients by introducing an achromatic telescopic squeeze (ATS)-like chromatic control between IP2 and IP3 of HL-LHC. These optics can be seen in figure 84. In this figure a semi-logarithmic scale was used to see the ATS beta wave. These arcs can be created for a chosen $\beta^*$ with the routine designed in `rematch_arc23.madx`.

The dynamical aperture for these optics was subsequently investigated. The results of the tracking calculations performed for the particles defined in figure 62, can be seen in figure 85.

The thus defined minimal DA amounts to only $4.975\,\sigma$ for particles initialized at an angle $\theta$ of 22.5 rad. This relatively low result could be a consequence of the available aperture shrinking for such a low $\beta^*$.

Another reason for the high loss of particles might be the sextupole gradients still reaching high values in order to control the chromaticity induced by the quadrupole gradients in the LHeC interaction region. In the dynamic aperture study performed on these optics, the conventional correctors were used for the

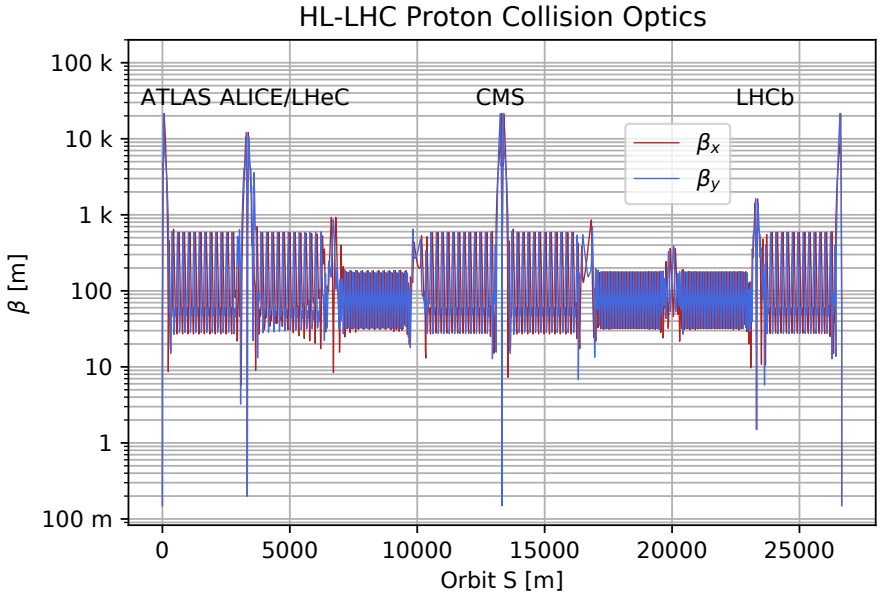


**Figure 84:** Beam size for an optics for LHeC with $\beta^*= 0.2\,\mathrm{m}$. An ATS wave is introduced between IP2 and IP3.

tune and the chromaticity corrections.

The tune is corrected with trim quadrupoles in the arcs, while the chromaticity is corrected with the use of the sextupoles. These groups of correctors do not work independently of each other, but are usually powered over common circuits. A detailed explanation on the powering of the arc sextupoles can be found in [69]. An overview of the powering of the magnets in the LHC arcs can be found in [113]. The so-called *knobs* defined in MAD-X are linear combinations of magnet strengths. A tune knob controls several quadrupoles together in order to adjust the machine tune, while a sextupole knob controls several sextupoles to adjust the chromaticity. These knobs were first introduced in section A.3.1 for the orbit correctors for different amplitudes of the orbit bumps. A detailed explanation of the sextupoles correcting the chromaticity, as well as how the tune knobs are defined, can be found in [114, 114].

**Definition of Tune Knobs** The off-momentum particles in a beam travel through the accelerator on a distorted orbit. As they pass through the quadrupoles, they see a modified quadrupole strength. The induced tune shift $\Delta Q$ by quadrupoles of a strength $k(s)$ across the whole orbit can be seen in equation85 [115].

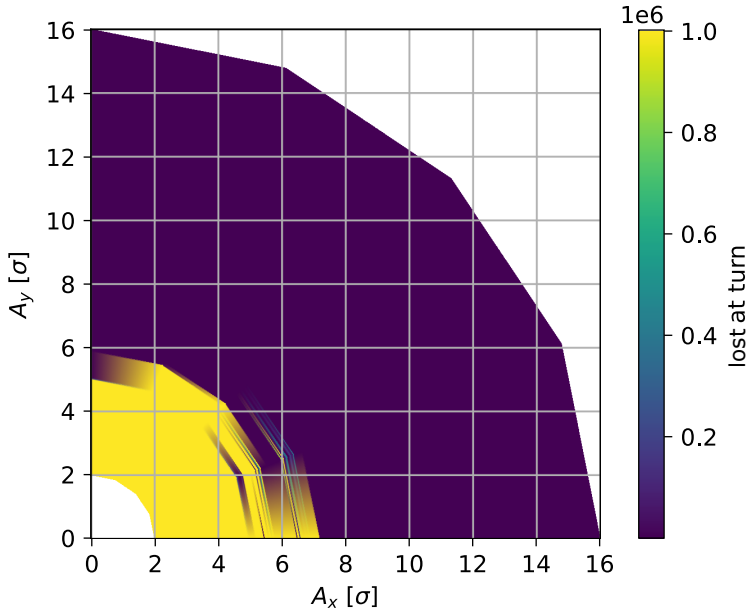


**Figure 85:** Dynamic aperture study for the particle distribution shown in 62 over one million turns. The tracked optics can be seen in figure 85. These optics focus the beam to $\beta^* = 0.2\,\mathrm{m}$ and have an ATS wave between IP2 (ALICE/LHeC) and IP3 in HL-LHC. In this tracking calculation no beam-beam effects were considered.

$$\Delta Q = \frac{1}{4\pi} \int \beta_{x,y}(s) \Delta k(s)\,\mathrm{ds} \tag{85}$$

With $\beta_{x,y}(s)$ being the amplitude function at a position $s$.

This relationship can be used to define the weighted tune knobs with:

$$\Delta Q = \sum_i \frac{1}{4\pi} \beta_i \,\Delta k_i \,\Delta s_i \tag{86}$$

This formula expresses how the tune can be influenced with the different quadrupole strengths $\Delta k_i$ at the positions $\Delta s_i$.

**ATS Tune and Chromaticity Knobs** It is necessary to redefine the tune-, as well as the chromaticity-knobs for LHeC, when using this ATS correction in the arc between IP2 and IP3. These knobs usually use groups of tune (trim

quadrupoles) and chromaticity correctors (sextupoles) in the non ATS arcs: arc 23, arc 34, arc 67 and arc 78, to rematch the tune and the chromaticity globally across the whole accelerator. When introducing another ATS arc between IP2 and IP3, only three arcs (34, 67 and 78) are left for this correction. To define the tune knobs for these three arcs, a routine has been developed in `NbTi_triplet/tools/save_tune_knobs.ipynb`.

It works by first matching different values for the tune and saving the the strength of the quadrupole gradient of the tune correctors. Next, a linear fit is performed on these data points, and the tune knobs are defined. For a certain tune, the value of the corrector can be easily defined with this linear fit. It also facilitates the match, as not every trim quadrupole needs to be matched, but only one knob for a certain set of correctors.

In figure 86 an example of a linear fit performed on the trim quadrupoles for the tune correctors can be seen.

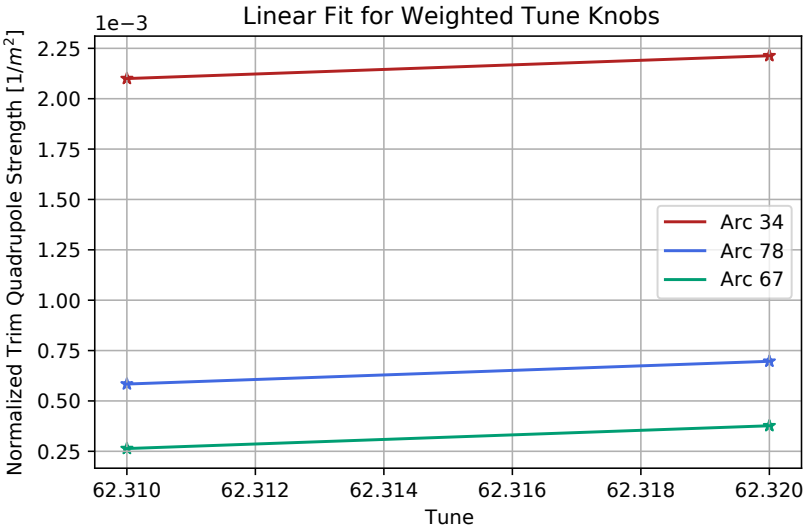


**Figure 86:** Linear fits performed in order to define the knobs used to match the tune. The stars mark two data points, while the lines mark the linear fit of the trim correctors of the non ATS arcs: 34, 67 and 78.

After correcting the tune, the chromaticity needs to be controlled. It can be corrected locally in the LHeC IR with the use of `NbTi_triplet/correct_chroma.madx`. In this correction the local sextupoles of arc 12 and arc 23 are used to control the chromaticity. Afterwards the chromaticity knobs can be defined with the use of `NbTi_triplet/tools/save_chroma_knobs.ipynb`. For these newly defined knobs, only the sextupoles in the non-ATS arcs are used (arc 34, arc 67, arc 78). Simi-

lar to the correction of the tune with quadrupoles, the linear chromaticity can be corrected with linear weighted combinations of sextupoles.

When the lattice is sliced before the tracking calculation and subsequently rematched, the ordinary tune and and chromaticity knobs were used in this PhD and not the newly defined ones. It would be interesting to repeat the dynamic aperture study for the LHeC proton optics with low amplitude functions $\beta^*$ and the newly defined knobs, to see if the lowering of the sextupole gradients through this ATS correction in the adjacent arc (together with newly defined tune and chromaticity knobs) can prolong the lifetime of higher amplitude particles.

## B.3 Luminosity Expectation for LHeC without the Spectating Proton Beam

In section 8 the different luminosities depending on the LHeC design were compared. In these comparisons, LHeC runs concurrently to the other HL-LHC experiments. It would also be possible to operate the designed interaction regions of LHeC, without running the other HL-LHC experiments at the same time. As a result, the available aperture for B1 would be increased, as there would be no second proton beam B2 which would share the same IR. It was possible to lower $\beta^*_{\mathrm{B1}}$ down to $0.35\,\mathrm{m}$ in IP2, with the use of the current triplet, consisting of NbTi. For lower values, the increase in the amplitude function was too big to assure enough beam stay clear to the beam pipe and it would become necessary to invest in $Nb_3Sn$ magnets.

| **Parameter** | **NbTi triplet** | **$Nb_3Sn$ triplet** |
|---|---|---|
| $L^*$ | $22.965\,\mathrm{m}$ | $22.965\,\mathrm{m}$ |
| $\beta^*_p$ | $0.35\,\mathrm{m}$ | $0.13\,\mathrm{m}$ |
| Luminosity | $1.4 \times 10^{33}\,\mathrm{cm}^{-2}\,\mathrm{s}^{-1}$ | $3.9 \times 10^{33}\,\mathrm{cm}^{-2}\,\mathrm{s}^{-1}$ |
| Hardware Changes | • Electron Magnet Insertion 4<br>• Recabling of Quadrupoles 5.2.1 | • Electron Magnet Insertion 4<br>• Recabling of Quadrupoles 5.2.1<br>• $Nb_3Sn$ magnets 5.3 |
| Detector Design | Multipurpose [49] | Multipurpose [49] |

**Table 22:** Performance parameters for designs of LHeC as a run alone experiment.

For this type of design, the beam-beam effects are limited to the ones between the proton beam, and the electron beam. The main limitation to the luminosity would be the available aperture of the proton beam, as well as possibly the chromaticity. A major obvious drawback of this design is that it could not run concurrently to the other HL-LHC experiments.

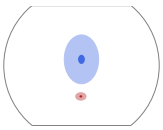

In this PhD an optics of $0.13\,\mathrm{m}$ was created for the $Nb_3Sn$ triplet. With this value a beam stay clear of $9.14\,\sigma$ could be assured. It might be possible to lower this $\beta^*$ value even further with the corresponding chromatic control down to $10\,\mathrm{cm}$, since that is a value HL-LHC aims to reach in IP1 and IP5 [116]. With a value of $\beta^*$ =$0.1\,\mathrm{m}$, an e-p luminosity of $0.5 \times 10^{34}\,\mathrm{cm}^{-2}\,\mathrm{s}^{-1}$ can be reached.

With this choice, the luminosity is increased by about $20\,\%$ (NbTi) or $54\,\%$ ($Nb_3Sn$). However, the run alone design would not be compatible with the other HL-LHC experiments and is therefore not a viable option for LHeC.

## B.4 Tune Footprint of the Colliding Proton Beam of LHeC

In section 6 the optimal optics of the colliding proton beam have been determined to be $\beta^*$ =$0.45\,\mathrm{m}$. In figure 87 the footprint of these optics can be seen. In this design the electron insertion has been added.

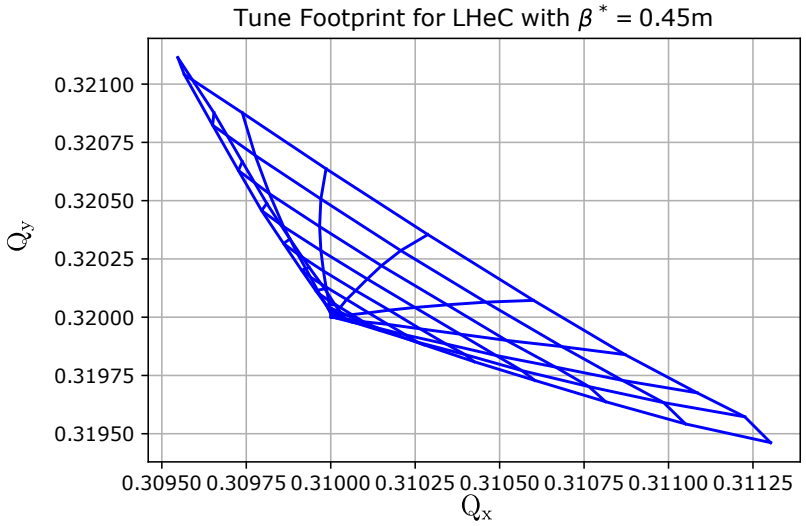


**Figure 87:** Tune footprint for LHeC proton optics with $\beta^* = 0.45\,\mathrm{m}$.

# C Appendix III: Design of the Interaction Region for the FCC-eh Collider

The FCC-eh repository can be found at: `FCC_eh`. The electron insertion can be installed with an installation and a strength file, which can be found here: `FCC_eh/electron_insertion`. These files need to be loaded additionally to the FCC-hh lattice. The optics and orbit correction can be performed using: `FCC_eh/FCC_PD.ipynb`.

## References

[1] David Griffiths. *Introduction to Elementary Particles*. John Wiley & Sons, 2020.

[2] Andrew A Armstrong. *Beyond scientific research: tracing the contributions Ernest Rutherford made to the next generation of scientists*. PhD thesis, Texas A&M University, 2006.

[3] CERN. CERN Rapport annuel 2024. Technical report, CERN, Geneva, 2025. URL https://cds.cern.ch/record/2931993.

[4] Sheldon Lee Glashow. Toward a unified theory: Threads in a tapestry. *Science*, 210(4476):1319–1323, 1980.

[5] Carlo Rubbia. Experimental observation of the intermediate vector bosons W+, W-, and Z 0. *Reviews of Modern Physics*, 57(3):699, 1985.

[6] Simon Van Der Meer. Stochastic cooling and the accumulation of antiprotons. *Reviews of Modern Physics*, 57(3):689, 1985.

[7] ATLAS Collaboration et al. Observation of a new particle in the search for the standard model higgs boson with the ATLAS detector at the LHC. *Physics Letters B*, 2012.

[8] J B Dainton, M Klein, P Newman, E Perez, and F Willeke. Deep inelastic electron-nucleon scattering at the LHC. *Journal of Instrumentation*, 1(10): P10001–P10001, October 2006. ISSN 1748-0221. doi: 10.1088/1748-0221/1/10/p10001. URL http://dx.doi.org/10.1088/1748-0221/1/10/P10001.

[9] Frederick Bordry, Michael Benedikt, Oliver Bruning, John Jowett, Lucio Rossi, Daniel Schulte, Steinar Stapnes, and Frank Zimmermann. Machine Parameters and Projected Luminosity Performance of Proposed Future Colliders at CERN, 2018. URL https://arxiv.org/abs/1810.13022.

[10] CERN. Future Circular Collider (FCC). https://home.cern/science/accelerators/future-circular-collider, 2025. Accessed: April 26, 2025.

[11] P Agostini, H Aksakal, S Alekhin, PP Allport, N Andari, KDJ Andre, D Angal-Kalinin, S Antusch, L Aperio Bella, L Apolinario, et al. The Large Hadron–electron Collider at the HL-LHC. *J. Phys. G: Nucl. Part. Phys.*, 48 (11):110501, dec 2021. doi: 10.1088/1361-6471/abf3ba.

[12] Oliver Brüning et al. An Energy Recovery Linac for the LHeC. *Eur. Phys. J. ST*, 2022. URL https://arxiv.org/abs/2206.07678.

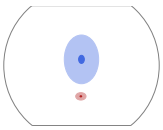

[13] Gustavo Perez Segurana, Andrey Abramov, Wolfgang Bartmann, Michael Benedikt, Roderik Bruce, Massimo Giovannozzi, Thys Risselada, Ezio Todesco, and Frank Zimmermann. New baseline layout of the CERN Future Circular hadron-hadron Collider. *PoS*, ICHEP2024:833, 2025. doi: 10.22323/1.476.0833.

[14] Tiziana Von Witzleben, Bernhard Holzer, Gustavo Perez Segurana, Kevin Daniel Joel Andre, Massimo Giovannozzi, Jorg Pretz, and Max Klein. Design and optimisation of the ep (and possibility joint ep/pp) Interaction Region. In *FCC Week 2023*, 2023. URL https://indico.cern.ch/event/1202105/contributions/5435641/.

[15] KDJ André, L Aperio Bella, N Armesto, SA Bogacz, D Britzger, OS Brüning, M D'Onofrio, EG Ferreiro, O Fischer, C Gwenlan, et al. An experiment for electron-hadron scattering at the LHC. *The European Physical Journal C*, 82 (1):40, 2022.

[16] Gustavo Perez Segurana and Massimo Giovannozzi. New FCC-hh ring layout: arc and insertion optics. In *Proceedings of FCC Week 2023*, London, UK, June 8 2023. URL https://indico.cern.ch/event/1202105/contributions/5383625/. Oral presentation, 20 min, Orchard Suite, Millennium Gloucester Hotel Kensington, FCC Week 2023 (June 5–9, 2023).

[17] Giovanni Anelli, Manuela Cirilli, and Anais Rassat. HOW PARTICLE PHYSICS RESEARCH AT CERN CONTRIBUTES TO MEDICAL INNOVATION. *Global Innovation Index*, 2019:141, 2019.

[18] CERN. The Birth of the World Wide Web. https://home.cern/science/computing/birth-web, 2019. Accessed: 2025-02-14.

[19] Katie Elyce Jones. The coevolution of particle physics and computing. *Symmetry Magazine*, June 2016. URL https://www.symmetrymagazine.org/article/the-coevolution-of-particle-physics-and-computing. Accessed: 2025-02-10.

[20] Marie Curie. Radium and the new concepts in chemistry. *Nobel lecture*, 1911.

[21] Marie Curie. The Discovery of Radium, 1921.

[22] F. Ahmadova, K. André, N. Armesto, G. Azuelos, O. Behnke, M. Boonekamp, M. Bonvini, D. Britzger, O. Brüning, T. A. Bud, A. M. Cooper-Sarkar, J. D'Hondt, M. D'Onofrio, O. Fischer, L. Forthomme, F. Giuli, C. Gwenlan, E. Hammou, B. Holzer, H. Khanpour, U. Klein, P. Kostka, T. Lappi, H. Mäntysaari, B. Mellado, P. R. Newman, F. I. Olness, J. A. Osborne, Y. Papaphilippou, H. Paukkunen, K. Piotrzkowski,

A. Polini, J. Rojo, M. Schott, S. Schumann, C. Schwanenberger, A. M. Staśto, A. Stocchi, S. Tentori, M. Tevio, C. Wang, and Y. Yamazaki. The Large Hadron electron Collider as a bridge project for CERN, 2025. URL https://arxiv.org/abs/2503.17727.

[23] A. Abada, S. Arias, T. Sjöstrand, J. Zurita, and FCC Collaboration. FCC Physics Opportunities: Future Circular Collider Conceptual Design Report Volume 1. *European Physical Journal C*, 79(6):474, 2019. doi: 10.1140/epjc/s10052-019-6904-3.

[24] ep/eA@CERN study group. The LHeC project. CERN Indico page, 2024. URL https://indico.cern.ch/event/1423870/page/34315-the-lhec-project. ep/eA@CERN Study Group, accessed: YYYY-MM-DD.

[25] R Yoshida and M Klein. Collider physics at HERA. *Prog. Part. Nucl. Phys.*, 61(ANL-HEP-PR-08-23), 2008.

[26] Rüdiger Voss. Highlights from muon scattering at CERN. Technical report, P00001674, 1992.

[27] Daniel Britzger, Max Klein, and Hubert Spiesberger. Electroweak physics in inclusive deep inelastic scattering at the LHeC. *The European Physical Journal C*, 80(9):831, 2020.

[28] Baradhwaj Coleppa, Mukesh Kumar, Satendra Kumar, and Bruce Mellado. Measuring CP nature of top-Higgs couplings at the future Large Hadron electron collider. *Physics Letters B*, 770:335–341, 2017.

[29] Daniel Britzger, Max Klein, and Hubert Spiesberger. Precision electroweak physics at the LHeC and FCC-eh. *arXiv preprint arXiv:2203.06237*, 2022.

[30] Klaus Wille. *The Physics of Particle Accelerators: An Introduction*. Oxford University Press, 2000. ISBN 978-0198505495.

[31] CERN. CERN Accelerator School Documentation, 2025. https://cas.web.cern.ch/previous-schools// [Accessed: 11.11.2025].

[32] Kévin Daniel Joel André. *Lattice Design and Beam Optics for the Energy Recovery Linac of the Large Hadron-Electron Collider*. PhD thesis, The University of Liverpool, 2022.

[33] Bernhard Holzer. Transversal Beam Dynamics. University Lecture, 2022.

[34] Werner Herr and Bruno Muratori. Concept of Luminosity. Technical Report CERN-AB-2006-017, CERN, 2006. URL http://cds.cern.ch/record/941318.

[35] Hannes Bartosik, Fanouria Antoniou, and Davide Gamba. Linear imperfections and Correction. University Lecture, 2022.

[36] Werner Herr. Beam-beam interactions, 2006. URL https://cds.cern.ch/record/941319.

[37] E D Courant and H S Snyder. Theory of the Alternating-Gradient Synchrotron. *Ann. Phys.*, 3:1–48, 1958. URL https://cds.cern.ch/record/593259.

[38] Linbo Liang, Guoxing Xia, Alexander Pukhov, and John Patrick Farmer. Acceleration of an Electron Bunch with a Non–Gaussian Transverse Profile in Proton-Driven Plasma Wakefield. *Applied Sciences*, 12(21), 2022. ISSN 2076-3417. doi: 10.3390/app122110919. URL https://www.mdpi.com/2076-3417/12/21/10919.

[39] H Mainaud Durand, S Bartolome-Jimenez, T Dijoud, et al. HL-LHC alignment requirements and associated solutions. In *Proc. 8th Int. Particle Accelerator Conf.(IPAC'17)*, pages 1893–1896, 2017.

[40] Robert Williamson. Accelerator Physics Lecture 7: Momentum Effects, 2019. URL https://indico.cern.ch/event/847209/timetable/?print=1&view=nicecompact.

[41] Jerald Pinson. The power of attraction: Magnets in particle accelerators. Fermilab News, March 2020. URL https://news.fnal.gov/2020/03/the-power-of-attraction-the-use-of-magnets-in-particle-accelerators/.

[42] CERN BE/ABP Accelerator Beam Physics Group. MAD: Methodical Accelerator Design, 2024. https://madx.web.cern.ch/ [Accessed: 01.09.2024].

[43] Giovanni Iadarola et al. Xsuite: An Integrated Beam Physics Simulation Framework. *JACoW*, HB2023:TUA2I1, 2024. doi: 10.18429/JACoW-HB2023-TUA2I1.

[44] M. Klein and R. Yoshida. Collider physics at HERA. *Progress in Particle and Nuclear Physics*, 61(2):343–393, October 2008. ISSN 0146-6410. doi: 10.1016/j.ppnp.2008.05.002. URL http://dx.doi.org/10.1016/j.ppnp.2008.05.002.

[45] W. Bialowons. Status of HERA. In *Proc. EPAC'96*, number 5 in European Particle Accelerator Conference, pages 3–7. JACoW Publishing, Geneva, Switzerland, 9 1996.

[46] J. Wenninger. Machine Protection and Operation for LHC. *CERN Yellow Reports*, page Vol 2 (2016): Proceedings of the 2014 Joint International Accelerator School: Beam Loss and Accelerator Protection, 2016. doi: 10.5170/CERN-2016-002.377. URL https://e-publishing.cern.ch/index.php/CYR/article/view/242.

[47] F. Caspers. Energy Recovery Linacs. In *CERN Accelerator School: General Accelerator Physics*, pages 227–245. CERN, 2003. https://cds.cern.ch/record/1058089/files/p227.pdf.

[48] Emilia Cruz Alaniz. *Modelling the effects of high-luminosity optics in the upgrades of the Large Hadron Collider*. PhD thesis, U. Liverpool (main), 2016.

[49] Peter Kostka. Introduction to the LHeC detector design/simulation. Presented at the LHeC/FCC-eh Beam Dynamics and Machine-Detector Interface Workshop, September 2024. URL https://indico.cern.ch/event/1423983/contributions/6031338/. CERN, Geneva, Switzerland.

[50] K. D. J. André, L. Aperio Bella, N. Armesto, S. A. Bogacz, D. Britzger, O. S. Brüning, M. D'Onofrio, E. G. Ferreiro, O. Fischer, C. Gwenlan, B. J. Holzer, M. Klein, U. Klein, F. Kocak, P. Kostka, M. Kumar, B. Mellado, J. G. Milhano, P. R. Newman, K. Piotrzkowski, A. Polini, X. Ruan, S. Russenschuk, C. Schwanenberger, E. Vilella-Figueras, and Y. Yamazaki. An experiment for electron-hadron scattering at the LHC. *The European Physical Journal C*, 82(1), January 2022. ISSN 1434-6052. doi: 10.1140/epjc/s10052-021-09967-z. URL http://dx.doi.org/10.1140/epjc/s10052-021-09967-z.

[51] CERN. The High-Luminosity LHC (HL-LHC). https://voisins.web.cern.ch/en/high-luminosity-lhc-hl-lhc, 2025. Accessed: April 26, 2025.

[52] O. Brüning, A. Seryi, and S. Verdú-Andrés. Electron-Hadron Colliders: EIC, LHeC and FCC-eh. *Frontiers in Physics*, 10:886473, 2022. doi: 10.3389/fphy.2022.886473. URL https://www.frontiersin.org/articles/10.3389/fphy.2022.886473/full.

[53] Michael Benedikt and Frank Zimmermann. FCC-ee Feasibility Study Progress. In *Proceedings of the 65th ICFA Advanced Beam Dynamics Workshop on High Luminosity Circular $e^+e^-$ Colliders (eeFACT2022)*, pages 7–13, Frascati, Italy, September 2023. JACoW. doi: 10.18429/JACoW-eeFACT2022-MOXAT0104. URL https://accelconf.web.cern.ch/eefact2022/papers/moxat0104.pdf.

[54] A Dainese and A Di Mauro. Scoping document for the ALICE 3 detector. Technical report, CERN, Geneva, 2025. URL https://cds.cern.ch/record/2925455.

[55] M. Benedikt and F. Zimmermann et al. Future Circular Collider Feasibility Study Report, Vol. 1: Physics, Experiments, Detectors. Technical Report CERN-FCC-PHYS-2025-0002, CERN, 2025. URL https://cds.cern.ch/record/2928193.

[56] Achille Stocchi. ERLs and the European Stategy Update, October 2025.

[57] G. Apollinari, I. Béjar Alonso, O. Brüning, P. Fessia, M. Lamont, L. Rossi, and L. Tavian. High-Luminosity Large Hadron Collider (HL-LHC): Technical Design Report V. 0.1. Technical Report CERN-2017-007-M, CERN, 2017. URL https://cds.cern.ch/record/2284929. CERN Yellow Reports: Monographs.

[58] Lyndon Evans and Philip Bryant. The Large Hadron Collider: Design Report, Volume I: The LHC Main Ring. Technical Report CERN-2004-003-V-1, CERN, 2008. URL https://cds.cern.ch/record/782076. Design luminosity: $1 \times 10^{34}$ cm$^{-2}$s$^{-1}$.

[59] CERN. Record luminosity: Well done LHC!, 2023. URL https://home.cern/news/news/accelerators/record-luminosity-well-done-lhc. Peak luminosity achieved: $2.06 \times 10^{34}$ cm$^{-2}$s$^{-1}$.

[60] L. Fiscarelli, E. Todesco, F. Mangiarotti, G. Deferne, M. Pentella, P. Rogacki, S. Russenschuck, and S. Izquierdo Bermudez. Measurement of Integrated Gradient and Field Quality on the First Q2 Magnets for HL-LHC. In *Proceedings of IPAC 2024*, 2024. Paper WEPS64; DOI: 10.18429/JACoW-IPAC2024-WEPS64.

[61] F. Bordry and H. Thiesen. LHC Inner Triplet Powering Strategy. In *Proceedings of the 19th IEEE Particle Accelerator Conference (PAC 2001)*, pages e–proc. 633, Chicago, IL, USA, 2001. IEEE. Imprint date: 6 August 2001.

[62] Stephane Fartoukh, Alexander Valishev, and Dmitry Shatilov. An Alternative High Luminosity LHC with Flat Optics and Long-Range Beam-Beam Compensation. In *Proceedings of IPAC2015*, pages 211–214, Richmond, VA, USA, 2015. JACoW. URL https://accelconf.web.cern.ch/IPAC2015/papers/tupty073.pdf. TUPTY029.

[63] Tatsushi Nakamoto, Michinaka Sugano, Qingjin Xu, Hiroshi Kawamata, Shun Enomoto, Norio Higashi, Akira Idesaki, Masami Iio, Yukiko Ikemoto, Ruri Iwasaki, Nobuhiro Kimura, Toru Ogitsu, Naoki Okada, Ken-ichi Sasaki, Makoto Yoshida, and Ezio Todesco. Model Magnet Development of

D1 Beam Separation Dipole for the HL-LHC Upgrade. *IEEE Transactions on Applied Superconductivity*, 25(3):1–5, 2015. doi: 10.1109/TASC.2014.2361404.

[64] N.V. Mokhov, C. James, L.S. Esposito, et al. Energy deposition studies for the high-luminosity Large Hadron Collider insertion regions. *Physical Review Special Topics – Accelerators and Beams*, 18(5):051001, 2015. doi: 10.1103/PhysRevSTAB.18.051001. States that "a superconducting D1 separation dipole will replace the normal-conducting version" due to high heat and radiation deposition in HL-LHC.

[65] CERN. Crab cavities: colliding protons head-on. `https://home.cern/news/news/accelerators/crab-cavities-colliding-protons-head`, 2018. Accessed: 2025-04-28.

[66] Matthew Smith. Design of a 3D Plot for the LHeC IR. Student Internship, August 2022.

[67] B. J. Holzer. Introduction to Transverse Beam Dynamics. In R. Bailey, editor, *Proceedings of the CAS-CERN Accelerator School: Superconductivity for Accelerators*, CERN–2014–005, pages 171–218, Erice, Italy, April 24 – May 4 2014. CERN.

[68] F. Sannibale. Real Accelerators: Errors & Diagnostics, 2006. URL `https://www2.als.lbl.gov/als_physics/Fernando/USPASJan06Lectures/L13_TheRalAccelerator.pdf`.

[69] Stephane Fartoukh. Achromatic telescopic squeezing scheme and application to the LHC and its luminosity upgrade. *Physical Review Special Topics – Accelerators and Beams*, 16(11):111002, 2013. doi: 10.1103/PhysRevSTAB.16.111002. Introduces and details the ATS concept chosen as the baseline optics scheme for HL-LHC.

[70] Stéphane Fartoukh. Achromatic telescopic squeezing scheme and application to the LHC and its luminosity upgrade. *Phys. Rev. ST Accel. Beams*, 16:111002, Nov 2013. doi: 10.1103/PhysRevSTAB.16.111002. URL `https://link.aps.org/doi/10.1103/PhysRevSTAB.16.111002`.

[71] S Fartoukh, R Bruce, F Carlier, J Coello De Portugal, A Garcia-Tabares, E Maclean, L Malina, A Mereghetti, D Mirarchi, T Persson, M Pojer, L Ponce, S Redaelli, B Salvachua, P Skowronski, M Solfaroli, R Tomas, D Valuch, A Wegscheider, and J Wenninger. Experimental validation of the Achromatic Telescopic Squeezing (ATS) scheme at the LHC. *Journal of Physics: Conference Series*, 874(1):012010, jul 2017. doi: 10.1088/1742-6596/874/1/012010. URL `https://dx.doi.org/10.1088/1742-6596/874/1/012010`.

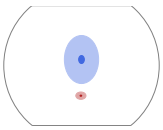

[72] S. Y. Lee. *Accelerator Physics*. World Scientific, 4th edition, 2018. ISBN 9789813274686. doi: 10.1142/11111.

[73] S. Fartoukh, R. Bruce, F. Carlier, J. Coello de Portugal, A. García-Tabares, et al. Experimental validation of the Achromatic Telescopic Squeezing (ATS) scheme at the LHC. In *Journal of Physics: Conference Series*, volume 874 of *JPCS*, page 012010, 2017. doi: 10.1088/1742-6596/874/1/012010. Reports beam tests during Run I and II validating ATS optics.

[74] Riccardo de Maria. acc-models-lhc: `opt_round_150_1500.madx` (branch `hl19`). GitLab repository file, 2025. URL `https://gitlab.cern.ch/acc-models/acc-models-lhc/-/blob/hl19/strengths/round/opt_round_150_1500.madx?ref_type=heads`. Accessed: 2025-12-12.

[75] Valerie MONTABONNET. IPQ CIRCUIT POWERING USING 3 OR 4 CABLES. Technical Report EDMS 1231467, CERN, 2012. URL `https://edms.cern.ch/document/1231467`. Available via CERN EDMS database.

[76] V. Montabonnet, H. Burkhardt, J.-C. Guillaume, A. Ballarino, I. Bejar Alonso, L. Bottura, J. P. Burnet, O. Bruening, J. Coupard, S. Deleval, F. Duval, K. Foraz, M. Giovannozzi, G. Kirby, M. Lamont, P. Le Roux, A. Musso, Y. Muttoni, M. Nonis, T. Otto, J. Pedersen, M. Pojer, S. Prodon, A. Siemko, M. Solfaroli, E. Todesco, A. Verweij, J. Wenninger, M. Zerlauth, P. Collier, and L. Rossi. Engineering Change Request: Electrical Circuit Change for High Beta Optics in IR1 and IR5 of the LHC. Technical Report LHC-LJ-EC-0042, CERN, 2014. URL `https://edms.cern.ch/document/1377232`. EDMS No. 1377232, Rev. 1.0, Released.

[77] E. Todesco, B. Auchmann, P. Fessia, F. Toral, G. Volpini, D. Wollman, C. Volpe, A. Ballarino, A. Musso, S. Deleval, M. Giovannozzi, G. Kirby, M. Lamont, P. Le Roux, A. Verweij, and J. Wenninger. The HL-LHC Interaction Region Magnets. *Superconductor Science and Technology*, 34(5):053001, 2021. doi: 10.1088/1361-6668/abdba4. URL `https://cds.cern.ch/record/2759601/files/10.1088_1361-6668_abdba4.pdf`.

[78] A. Rossi. Estimates of power generated from synchrotron radiation in the High-Luminosity LHC. *CERN Technical Report*, CERN-ACC-2017-011, 2017. URL `https://cds.cern.ch/record/2281095/files/HL-LHC-SyncRad_ARvf.pdf`. Accessed: 2025-08-19.

[79] HandWiki contributors. Ellipse. `https:https://en.wikipedia.org/wiki/Ellipse`, 2025. Accessed: 2025-12-02.

[80] Apollinari G., Béjar Alonso I., Brüning O., Fessia P., Lamont M., Rossi L., and Tavian L. *High-Luminosity Large Hadron Collider (HL-LHC)*, chapter MA-

CHINE LAYOUT AND PERFORMANCE, page 72. CERN, 2017. doi: 10.23731/CYRM-2017-004. URL https://cds.cern.ch/record/2284929.

[81] Thys Risselada. New Ideas for the MAD-X Aperture Calculation. Technical Report CERN-ACC-NOTE-2020-0066, CERN, Accelerators & Technology Sector, Geneva, Switzerland, December 2020. Internal note; published 16 December 2020.

[82] O. S. Brüning, P. Collier, P. Lebrun, S. Myers, R. Ostojic, J. Poole, and P. Proudlock. LHC Design Report Volume I: The LHC Main Ring. Technical Report CERN-2004-003-V1, CERN, Geneva, Switzerland, 2004. URL https://cds.cern.ch/record/782076/files/CERN-2004-003-V1.pdf. Published: 2004.

[83] Marco Morrone, Michele Martino, Riccardo De Maria, M. Fitterer, and Cedric Garion. Magnetic frequency response of High-Luminosity Large Hadron Collider beam screens. *Physical Review Accelerators and Beams*, 22, 01 2019. doi: 10.1103/PhysRevAccelBeams.22.013501.

[84] Roderik Bruce, Chiara Bracco, Riccardo De Maria, Massimo Giovannozzi, Stefano Redaelli, Rogelio Tomás Garcia, Francesco Maria Velotti, and Jörg Wenninger. Updated parameters for HL-LHC aperture calculations for proton beams. Technical Report CERN-ACC-2017-0051, CERN, 2017. URL https://cds.cern.ch/record/2274330. Accessed on May 5, 2025.

[85] Roderik Bruce, Chiara Bracco, Riccardo De Maria, Massimo Giovannozzi, Stefano Redaelli, Rogelio Tomas Garcia, Francesco Maria Velotti, and Jorg Wenninger. Parameters for aperture calculations at injection for HL-LHC*. Technical report, CERN, Geneva, 2016. URL https://cds.cern.ch/record/2237427. *Research supported by EU FP7 HiLumi LHC Grant agreement 284404.

[86] Vincent Baglin, Paolo Chiggiato, Cédric Garion, et al. Material characterization and preliminary mechanical design for the HL-LHC shielded beam screens operating at cryogenic temperatures. *World Scientific – High-Luminosity Large Hadron Collider*, 2024. doi: 10.1088/1757-899X/102/1/012013. URL https://iopscience.iop.org/article/10.1088/1757-899X/102/1/012013/pdf.

[87] Marco Morrone, Michele Martino, Riccardo De Maria, M. Fitterer, and Cedric Garion. Magnetic frequency response of High-Luminosity Large Hadron Collider beam screens. *Physical Review Accelerators and Beams*, 22, 01 2019. doi: 10.1103/PhysRevAccelBeams.22.013501.

[88] D. Di Croce, M. Giovannozzi, E. Krymova, T. Pieloni, S. Redaelli, M. Seidel, R. Tomás, and F. F. Van der Veken. Optimizing Dynamic Aperture Studies

with Active Learning, 2024. URL https://arxiv.org/abs/2402.11077.

[89] R. Tomás, G. Arduini, P. Baudrenghien, O. Brüning, R. Bruce, X. Buffat, R. Calaga, F. Cerutti, R. De Maria, J. Dilly, I. Efthymiopoulos, M. Giovannozzi, P. D. Hermes, G. Iadarola, R. Jones, S. Kostoglou, B. Lindström, E. H. Maclean, E. Métral, N. Mounet, Y. Papaphilippou, T. H. B. Persson, T. Pugnat, S. Redaelli, G. Sterbini, H. Timko, F. Van der Veken, J. Wenninger, and M. Zerlauth. Operational scenario of first high luminosity LHC run. *Journal of Physics: Conference Series*, 2420(1):012003, 2023. doi: 10.1088/1742-6596/2420/1/012003. URL https://iopscience.iop.org/article/10.1088/1742-6596/2420/1/012003.

[90] Colas Droin. DA studies for the new baseline. Talk presented at the 226th HiLumi WP2 Meeting, CERN, 22 March 2024, March 2024. https://indico.cern.ch/event/1395361/.

[91] G. Arduini and et al. HL-LHC Run 4 Proton Operational Scenario. CERN Indico Presentation, 2022. URL https://indico.cern.ch/event/1112119/attachments/2376539/4158466/Run_4_operational_scenario%20%286%29.pdf. Accessed: 2025-09-05.

[92] W. Kaabi, M. Klein, and the PERLE Collaboration. PERLE: Powerful Energy Recovery Linac for Experiments, 2025. URL https://perle-web.ijclab.in2p3.fr/. Accessed: 2025-09-06.

[93] M Elisei, E Beneduce, A Bersani, M Bracco, S Burioli, B Caiffi, M Cannavò, G Crespi, E De Matteis, S Dotti, et al. Design Comparison of Four-Layer Full-Nb 3 Sn and Hybrid Nb 3 Sn/NbTi Cos-Theta Dipoles for the CERN High Field Magnet R&D Programme. *IEEE Transactions on Applied Superconductivity*, 2025.

[94] E. Cruz Alaniz, M. Korostelev, D. Newton, and R. TomÃ¡s. LHeC IR Optics Design Integrated into the HL-LHC Lattice. In *Proc. 5th International Particle Accelerator Conference (IPAC'14), Dresden, Germany, June 15-20, 2014*, number 5 in International Particle Accelerator Conference, pages 1198–1201, Geneva, Switzerland, July 2014. JACoW. ISBN 978-3-95450-132-8. doi: https://doi.org/10.18429/JACoW-IPAC2014-TUPRO070. URL http://jacow.org/ipac2014/papers/tupro070.pdf. https://doi.org/10.18429/JACoW-IPAC2014-TUPRO070.

[95] E. Cruz-Alaniz, R. Martin, and R. Tomás. LHeC optics with $\beta^* = 10\,\text{cm}$ and $L^* = 15\,\text{m}$. Technical Report CERN-ACC-NOTE-2019-0049, CERN, November 2019. URL https://cds.cern.ch/record/2701426/files/CERN-ACC-NOTE-2019-0049.pdf. Accessed: 2025-09-08.

[96] O. Brüning. LHeC Cost Estimate. Technical Report CERN-ACC-2018-0061, CERN, December 2018. URL https://cds.cern.ch/record/2652349/files/CERN-ACC-2018-0061.pdf. Accessed: 2025-09-08.

[97] Max Klein and O. Brüning. LHeC, PERLE and FCC-eh. Presentation at the Snowmass Meeting on TeV Colliders, July 8 2020. URL https://hep.ph.liv.ac.uk/~mklein/LoIAccMK.pdf. Accessed via University of Liverpool website.

[98] Thomas Hortala. HL-LHC magnet endurance test further confirms niobium–tin's resilience. Press release / News article, CERN, July 2022. URL https://home.cern/news/news/accelerators/hl-lhc-magnet-endurance-test-further-confirms-niobium-tins-resilience-0. News article summarizing endurance test on $Nb_3Sn$ quadrupole magnet at BNL.

[99] ALICE Collaboration. Letter of intent for ALICE 3: A next-generation heavy-ion experiment at the LHC, 2022. URL https://arxiv.org/abs/2211.02491.

[100] Nicola Nicassio. ALICE 3: a next-generation heavy-ion detector for LHC Run 5 and beyond, 2023. URL https://arxiv.org/abs/2311.10164.

[101] M. Benedikt, F. Zimmermann, and et al. Future Circular Collider Feasibility Study Report Volume 2. Technical report, CERN, Geneva, 2025. URL https://cds.cern.ch/record/2928793. 627 pages. Please address any comment or request to fcc.secretariat@cern.ch.

[102] CERN. The Future Circular Collider, 2025. URL https://home.cern/science/accelerators/future-circular-collider. Accessed: 2025-10-01.

[103] Andrey Abramov, Frank Zimmermann, Gustavo Perez Segurana, Kieran Geiger, Massimo Giovannozzi, Michael Benedikt, Pierre Alexandre Thonet, Roberto Lopez, Roderik Bruce, Sergio Calatroni, Thys Risselada, and Wolfgang Bartmann. FCC-hh ring: overview of the new layout. In *Proceedings of FCC Week 2023*, London, UK, June 8 2023. URL https://indico.cern.ch/event/1202105/contributions/5383617/. Oral presentation, 25 min, Orchard Suite, Millennium Gloucester Hotel Kensington, FCC Week 2023 (June 5–9, 2023).

[104] Frank Zimmermann. Scenarios for the FCC-hh, 2024.

[105] Michael Benedikt, B. Goddard, Daniel Schulte, F. Zimmermann, and M. J. Syphers. FCC-hh Hadron Collider - Parameter Scenarios and Staging Options. In *6th International Particle Accelerator Conference*, page TUPTY062, 2015. doi: 10.18429/JACoW-IPAC2015-TUPTY062.

[106] CERN. CERN Yellow Reports: Monographs, Vol 3 (2017): Physics at the FCC-hh, a 100 TeV pp collider, 2017. URL https://e-publishing.cern.ch/index.php/CYRM/issue/view/35.

[107] A. Abada, M. Abbrescia, and S.S. et al. AbdusSalam. FCC-hh: The Hadron Collider Future Circular Collider Conceptual Design Report Volume 3. *The European Physical Journal Special Topics*, 2019. doi: https://doi.org/10.1140/epjst/e2019-900087-0.

[108] R. Tomas et al. Progress of the FCC-ee optics tuning working group. In *Proc. IPAC'23*, number 14 in IPAC'23 - 14th International Particle Accelerator Conference, pages 3158–3161. JACoW Publishing, Geneva, Switzerland, 05 2023. ISBN 978-3-95450-231-8. doi: 10.18429/JACoW-IPAC2023-WEPL023. URL https://indico.jacow.org/event/41/contributions/2234.

[109] M. Benedikt, M. Giovannozzi, and F. Zimmermann. Parameter and luminosity scenarios for FCC-hh. In *Proceedings of the 16th International Particle Accelerator Conference*, Geneva, Switzerland, 2025. URL https://indico.jacow.org/event/81/contributions/7337/.

[110] Adrienne Rich. *The dream of a common language: Poems 1974-1977*. WW Norton & Company, 2015.

[111] K.D.J. André. Private communication, 2023. Email received on July 13, 2023.

[112] Helmut Wiedemann. *Particle Accelerator Physics*. Springer, Cham, Switzerland, 4 edition, 2015. ISBN 978-3-319-18316-9. doi: 10.1007/978-3-319-18317-6.

[113] Paul Proudlock. Electrical powering strategy of LHC: First design study. Technical Report 11, CERN, Geneva, Switzerland, 1996. Presented at the 5th European Particle Accelerator Conference, Sitges, Barcelona, Spain, 10–14 June 1996; revised version submitted on 16 February 2004.

[114] S. Guiducci. Chromaticity. In *CERN Accelerator School: 5th Advanced Accelerator Physics Course*, pages 191–208, Geneva, Switzerland, 1994. CERN. URL https://cds.cern.ch/record/398300/files/p191.pdf. Accessed: 2025-09-05.

[115] William Barletta, Mei Bai, and Elvin Harms. Fundamentals of Accelerator Physics and Technology with Simulations and Measurements Lab, 2013. URL https://uspas.fnal.gov/materials/13CSU/CSU-Fundamentals.shtml. Accessed: 2025-09-02.

[116] Oliver Brüning and Markus Zerlauth. LHC operation and the High-Luminosity LHC upgrade project, 2025. URL https://arxiv.org/abs/2505.03535.

Typeset August 18, 2026